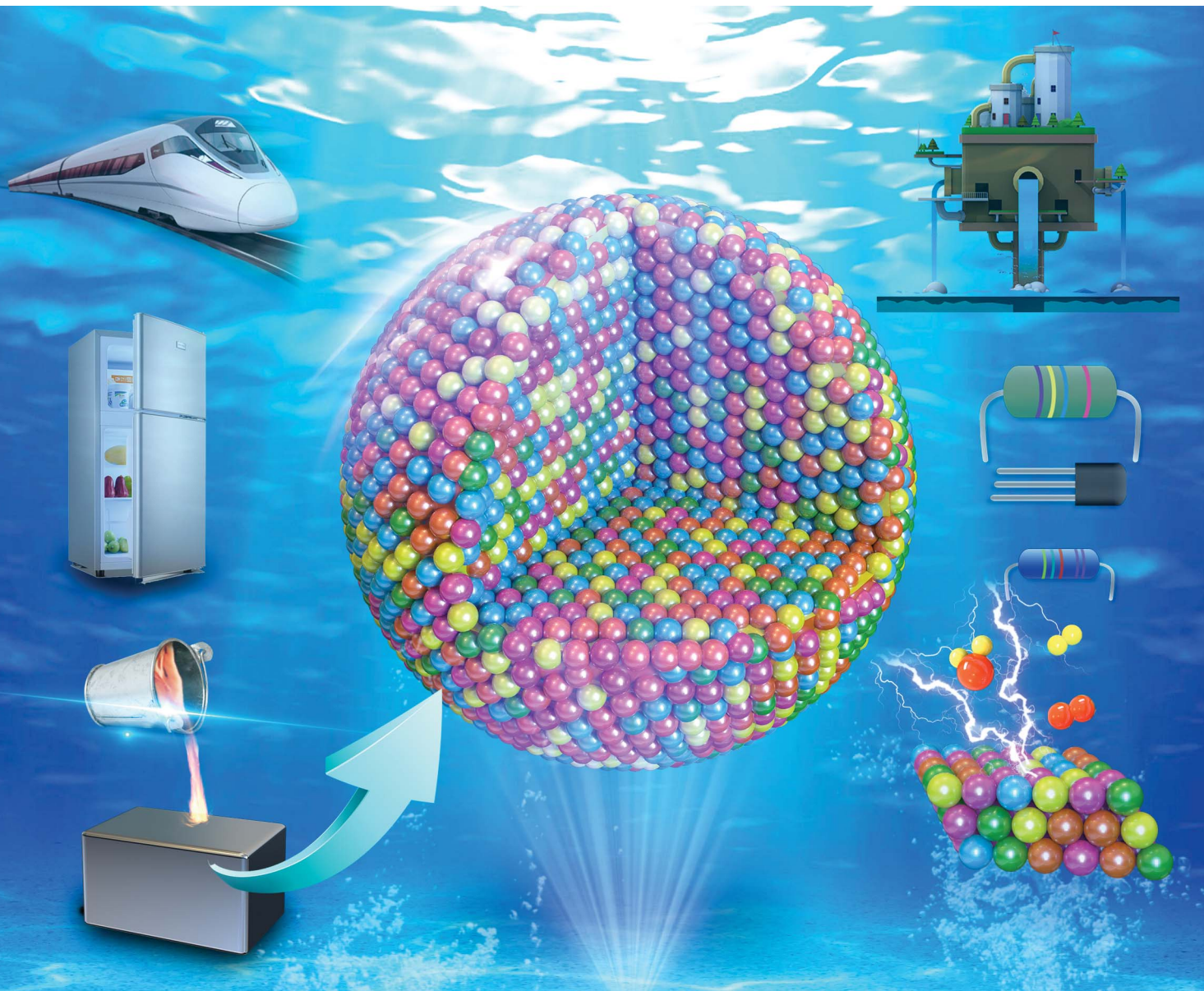


# Journal of Materials Chemistry A

Materials for energy and sustainability

rsc.li/materials-a



ISSN 2050-7488



Cite this: *J. Mater. Chem. A*, 2021, **9**, 663

Received 30th September 2020  
 Accepted 3rd November 2020

DOI: 10.1039/d0ta09601f  
[rsc.li/materials-a](http://rsc.li/materials-a)

## High-entropy alloys: emerging materials for advanced functional applications

Xin Wang, Wei Guo and Yongzhu Fu  \*

Accompanied by enhancements in the ability to fabricate materials for humans, alloy-based materials have advanced from binary alloy systems to complicated compositions along with affording newer applications, which can accelerate the evolution of civilization. Recently, high-entropy alloys (HEAs) have drawn enormous attention in diverse fields because of their distinctive concept and unique properties. The impressive mechanical properties, such as excellent strength, unforgettable corrosion resistance, and superior thermostability, are inherited and overwhelming compared with traditional alloys. Therefore, HEAs have become an emerging class of advanced materials leading to a new field. Based on the exceptional synthesis methods, HEAs surprisingly afford numerous energy and environmental properties, which have endowed HEAs with promising applications. In this paper, we review the salient features of HEAs and summarize their core effects, phase structures, unconventional synthesis methods, and novel energy and environmental applications. In addition, we also discuss the broad space waiting to be explored and overview fruitful pathways of future trends and prospects.

## 1. Introduction

Alloys have a long history with an irreplaceable contribution to the development of civilization. The Bronze Age thrived as early as 3000 BC, and the Iron Age has continued for about 3000 years since the Spring and Autumn and Warring States period.<sup>1</sup> Other alloys, such as Al alloys<sup>2</sup> and Mg and Ti alloys,<sup>3</sup> have been developed in the past century (Fig. 1a). Conventionally, most alloys are based on one major element, and this obviously limits their composition as well as the development of novel

properties. Therefore, unconventional alloys must be explored to satisfy the growing demand.

Because of the multielement composition, high-entropy alloys (HEAs) can possess unique properties. Many traditional properties (superior hardness, high strength, and enhanced wear resistance) endow HEAs to be attractive in many fields (thermoelectric (TE), magnetocaloric, superconducting, and catalysis materials). Moreover, the fabrication for HEAs does not need special equipment, indicating the immense potential of their mass production. This paper summarizes several important aspects, including core effects, phase formation, unique properties, and applications. It also indicates challenge and forecasts their directions for the future. From 2004 till now,

College of Chemistry, Zhengzhou University, Zhengzhou 450001, P. R. China. E-mail:  
[yfu@zzu.edu.cn](mailto:yfu@zzu.edu.cn)



Xin Wang received his BS from Huazhong University of Science and Technology in 2013. He then received his PhD from the College of Chemistry and Molecular Engineering at Peking University in 2018 under the supervision of Prof. Fuqiang Huang. In 2018, he joined the College of Chemistry at Zhengzhou University in China as a Lecturer. His current research is focused on the rational design and synthesis of alloy-based materials with the exploration of electrocatalytic properties.



materials.

Yongzhu Fu is a Professor in the College of Chemistry at Zhengzhou University in China. He received his PhD in Materials Science and Engineering from the University of Texas at Austin (USA) in 2007. He was an Assistant Professor at Indiana University-Purdue University, Indianapolis, in the USA before he joined Zhengzhou University in 2017. His research is focused on electrochemical energy

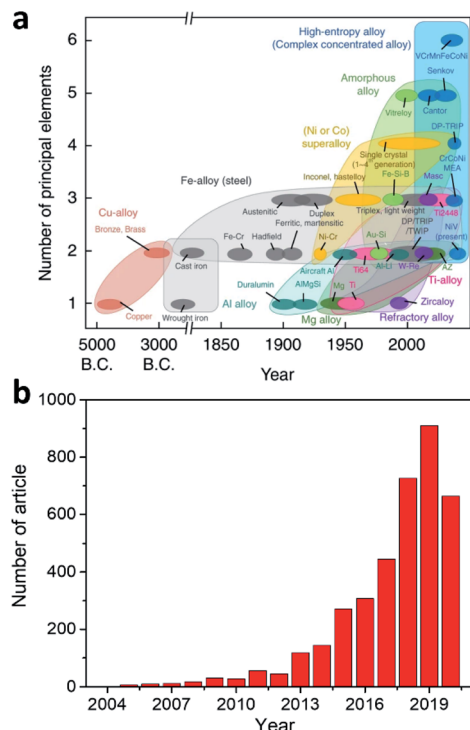


**Fig. 1** (a) A historical evolution diagram of the increasing number of principal elements comprising a common alloy system over the past few centuries. It includes copper, iron, aluminum, magnesium, titanium, refractory alloys, superalloys, and HEAs. Reproduced with the permission from ref. 5. Copyright © 2019, Springer Nature. (b) Publication statistics of the number of publications on HEAs per year until September 2020.

almost 3700 papers on HEAs have been published, covering almost every aspect of HEAs (Fig. 1b). The physical (magnetic, electrical, phases evolution, and thermal) properties have been reviewed elsewhere,<sup>4</sup> and they are not included in this review.

## 2. Definition and core effect of HEAs

### 2.1 Definition of HEAs

In general, there are two definitions of HEAs with respect to composition and entropy. However, whether multicomponent alloys can be regarded as HEAs is still unknown. The following are two brief introductions of the definitions.

**2.1.1 Composition-based definition.** The earliest composition-based definition was published in 2004.<sup>6</sup> In a broader sense, HEAs are defined as alloys containing at least five dominant elements, which are all in an atomic percentage between 5% and 35%. In addition, the atomic percentage of each minor element is less than 5%. It is defined as follows:

$$n_{\text{major}} \geq 5, 5 \text{ at\%} \leq c_i \leq 35 \text{ at\%} \quad (1)$$

$$n_{\text{minor}} \geq 0, c_j \leq 5 \text{ at\%} \quad (2)$$

where  $n_{\text{major}}$  and  $n_{\text{minor}}$  are the numbers of major and minor elements, respectively. Further,  $c_i$  and  $c_j$  are the corresponding atomic percentages.

**2.1.2 Entropy-based definition.** The total mixing entropy includes the following parts: configurational entropy ( $\Delta S_{\text{mix}}^{\text{conf}}$ ), vibrational entropy ( $\Delta S_{\text{mix}}^{\text{vib}}$ ), magnetic dipole entropy ( $\Delta S_{\text{mix}}^{\text{mag}}$ ), and electronic randomness entropy ( $\Delta S_{\text{mix}}^{\text{elec}}$ ); the relationship among them is given by

$$\Delta S_{\text{mix}} = \Delta S_{\text{mix}}^{\text{conf}} + \Delta S_{\text{mix}}^{\text{vib}} + \Delta S_{\text{mix}}^{\text{mag}} + \Delta S_{\text{mix}}^{\text{elec}} \quad (3)$$

The mixing entropy is dominated by configurational entropy. Fig. 2a shows the configurational entropy of equimolar alloys, which increases as the number of elements increases. For the liquid or solid solution of equimolar alloys, the configuration entropy per mole can be calculated based on the relationship between the entropy and complexion:

$$\begin{aligned} \Delta S_{\text{conf}} &= -k \ln \omega = -R \left( \frac{1}{n} \ln \frac{1}{n} + \frac{1}{n} \ln \frac{1}{n} + \dots + \frac{1}{n} \ln \frac{1}{n} \right) \\ &= -R \ln \frac{1}{n} = R \ln n \end{aligned} \quad (4)$$

From Fig. 2a, it is evident that the configurational entropy of a ternary alloy is slightly higher than  $R$  and that of a quinary alloy is higher than  $R$  by 61%. Therefore, the configurational entropy of  $1.5R$  is sufficiently large to be used as the boundary between HEAs and medium-entropy alloys. From the equation of configurational entropy, an element (5 at%) contributes a mixing entropy of  $0.15R$ , which is 10% of the minimum requirement for HEAs. Consequently, the element with an amount  $>5$  at% is regarded as the principal element, and the element with an amount  $<5$  at% is considered as the minor element. Furthermore, the increase in the configurational entropy for more than 13 elements is relatively small ( $0.07/2.57 = 2.7\%$ ); therefore, HEAs usually comprise 5 to 13 principal elements.<sup>7</sup>

The composition of HEAs is complicated because of the equimolar concentration of each component, which is different from traditional alloys. There are many factors affecting the microstructure and properties of HEAs. In thermodynamics, the high-entropy effect interferes with the formation of a complex phase. In terms of kinetics, the slow diffusion effect slows down the phase transition. For the structure, serious lattice distortion effects change the properties of the material to a certain extent. In nature, due to the interaction between different atoms and serious lattice distortion, the cocktail effect increases the number of mixing rule predictions. The next section explains these four core effects.

### 2.2 High-entropy effect

This effect was first proposed by Yeh,<sup>6</sup> which tends to stabilize the high-entropy phases and decreases the number of phases. It is generally believed that the composition of equiautomic or near-isoatomic alloys may form intermetallic phases; however, this is not the actual case. According to the Gibbs phase rule, the number of phases ( $P$ ) in a given alloy in equilibrium is

$$P = C + 1 - F \quad (5)$$

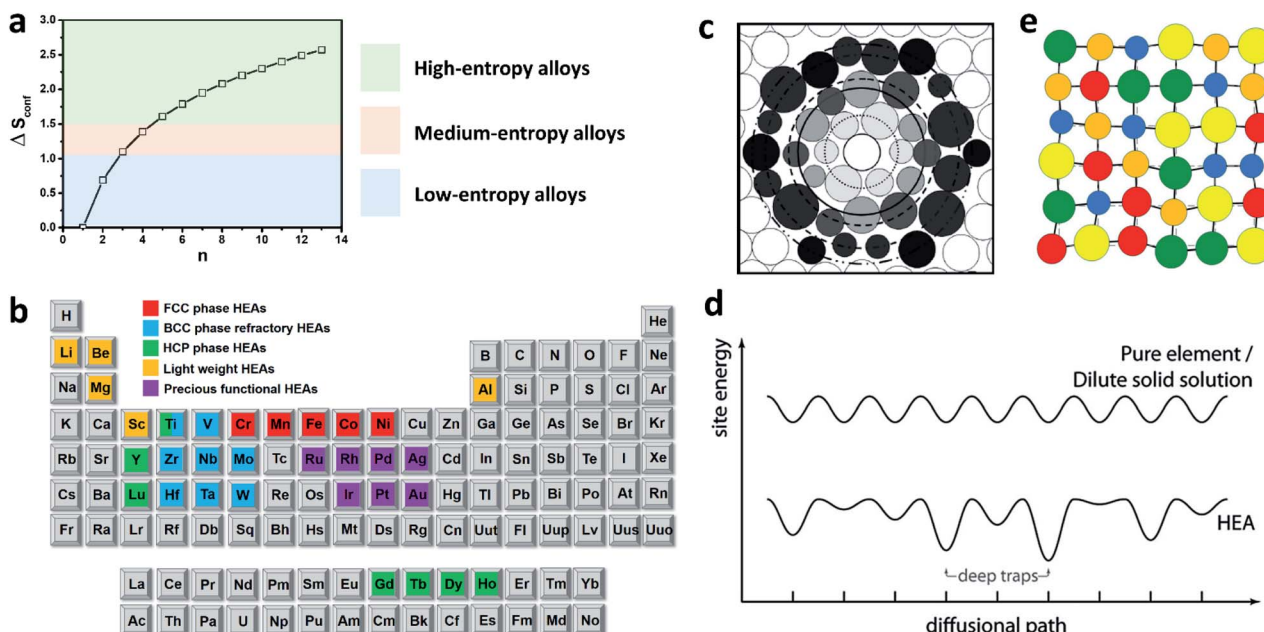


**Fig. 2** (a) Effect of equimolar number on the mixing entropy of the system. (b) Common elements included in the HEAs and classification of various HEAs. (c) Hard ball model shows the difference in the neighboring atom in the HEA. Reproduced with the permission from ref. 17. (d) Schematic diagram of the difference in the lattice potential energy distribution. Reproduced with the permission from ref. 18. Copyright © 2016, Taylor & Francis Group. (e) Severe distorted lattice in the HEA structure.<sup>17</sup> Copyright © 2013, Springer Nature.

where  $C$  is the number of components and  $F$  is the maximum thermodynamic degrees of freedom.

The diverse phase structures of HEAs are shown in Fig. 2b. The high configuration entropy reduces the free energy of the solid-solution phase and promotes the formation of solid solution at higher temperatures. The number of phases of HEAs obviously decreases because of the enhancement in the mutual solubility between the elements. According to the definition of the Gibbs free energy, when the temperature is sufficiently high, the entropy can stabilize the phase. For instance, the configurational entropy of an equimolar quinary solid solution is  $1.61R$ , which means that the difference in entropy between the equimolar quinary solution and an ordered phase is about 60% larger than the difference in the melting alloy mentioned above. Therefore, it is practicable for the solid-solution phase to become a stable phase at higher temperatures. Briefly, a higher number of elements can make the mixing enthalpy of the random state closer to the ordered state, and there will be more rivalry with the ordered state facilitated by the high entropy.

### 2.3 Sluggish diffusion effect

The diffusion and phase transition kinetics of HEAs are slower than those observed in traditional alloys.<sup>8</sup> There may be two reasons for this. The first one is that the neighboring atoms at each lattice position are different. Therefore, the neighborhood of an atom jumping into a vacancy is different from its original environment (Fig. 2c). Different configurations of local atoms result in different bonding and local energies. For example, when an atom jumps to a low-energy point, it will be “trapped” and it would be difficult to jump out of that position. On the

contrary, the atom stands a good chance to jump back to its original position if the site is a high-energy site (Fig. 2d). Both these conditions decrease the diffusion rate. It is suggested that the diffusion rate of HEAs is slow and the activation energy is high due to the large fluctuation in the lattice potential energy (LPE) between the crystal lattice sites.<sup>9</sup> A large number of low LPE sites could be used as traps to hinder the diffusion of atoms, resulting in the diffusion retardation effect.

The second reason is that each element in the HEA diffuses differently. Some elements are not as active as others; therefore, it is difficult for them to hop into vacancies compared with other elements. However, phase transition usually needs the co-diffusion of multiple elements. For instance, the formation of a new phase needs redistribution of all the elements to achieve the desired composition. The grain growth also needs the cooperation of all the elements to make the grain boundary migrate resoundingly. In these conditions, slow-moving elements become a rate-limiting factor, hindering the conversion process. Meanwhile, the sluggish diffusion effect might offer many advantages,<sup>10–12</sup> such as supersaturated state and fine precipitates, increase in recrystallization temperature, sluggish grain growth, and reduced grain coarsening. These benefits contribute to control the microstructure and its properties, further improving the performances.

### 2.4 Severe lattice distortion effect

The size differences that originate from different atom sizes ineluctably result in lattice distortion (Fig. 2e). In addition to the size differences in the atoms, the asymmetric binding and electronic structure between the atoms and their first

neighborhood also exist, and this influence varies with the position in the lattice. Therefore, the bond energy and crystal structure between the components also lead to severe lattice distortion.<sup>13</sup> It increases the scattering among the electrons and phonons, thereby reducing the conductivity and thermal conductivity.<sup>4</sup> To date, some studies using high-resolution transmission electron microscopy (TEM), X-ray diffraction, and neutron scattering images<sup>14,15</sup> have provided the evidence of severe lattice distortion in HEAs.

## 2.5 Cocktail effect

Ranganathan,<sup>16</sup> for the first time, put forward the term “multimetallic cocktails” and emphasize the important role of alloys in alloy development. The overall properties are determined by the phase shape, distribution, boundary, and total contribution of the properties of each phase to the constituent phases. However, each phase is a multicomponent solid solution, which is taken for an atomic-scale composite. Its comprehensive performance is not only derived from the basic properties of the elements under the mixing rule, but also from the interaction between the elements and severe lattice distortion. The interaction and lattice distortion increase the prediction of mixing rules. Generally speaking, the cocktail effect ranges from multicomponent composite effect at the atomic scale to the microscale. Therefore, understanding the relevant factors before choosing an appropriate composition and process is significant for alloy design. Regardless of its novelty, this method is useful in exploring more potential components for HEAs.

## 2.6 Criteria and models for HEAs

As the phase structure of HEAs has an important influence on the performance and application,<sup>19</sup> understanding the phase structure of HEAs is helpful to design HEAs with specific requirements. Therefore, the category of phase structure is first introduced. There are many phases in HEAs, such as solid solution, intermetallic compound, amorphous alloy, or a combination of these phases. Among the phase structures, solid-solution HEAs can be divided into BCC, FCC, and HCP phases. In the second part, there are more than 2000 types of intermetallic compounds, such as  $\mu$ ,  $\chi$ , and Laves phases. Besides, amorphous HEAs usually occur in the formation of bulk metallic glasses (BMGs). Then, we introduce the common thermodynamic parameters for evaluating HEAs and the relationship among these criteria with the crystal structures.

According to the Hume-Rothery rules, all the thermodynamic parameters are based on the definition of  $\Delta S_{\text{mix}}$  and  $\Delta H_{\text{mix}}$ , which are expressed using the following equations:<sup>20</sup>

$$\Delta S_{\text{min}} = -R \sum_{i=1}^n c_i \ln c_i \quad (6)$$

$$\Delta H_{\text{min}} = \sum_{i=1, j>i}^n 4\Delta H_{\text{AB}}^{\text{mix}} c_i c_j \quad (7)$$

where  $\Delta H_{\text{AB}}^{\text{mix}}$  is the enthalpy of mixing for the binary equiatomic AB alloys.

The atomic size mismatch ( $\delta$ ) is given by<sup>21</sup>

$$\delta = \sqrt{\sum_{i=1}^n c_i \left(1 - \frac{r_i}{\sum_{j=1}^n c_j r_j}\right)^2} \quad (8)$$

where  $r_i$  or  $r_j$  is the atomic radius for the  $i^{\text{th}}$  or  $j^{\text{th}}$  component, respectively. The atomic radii are taken from Senkov and Miracle,<sup>22</sup> where they were critically assessed and are now widely used in the field of HEAs.

Singh *et al.* suggested an empirical parameter ( $\Lambda$ )<sup>23</sup> to predict the formation of single-phase disordered solid solutions (DSS).  $\Lambda$  is defined as follows:

$$\Lambda = \frac{\Delta S_{\text{mix}}}{\delta^2} \quad (9)$$

The electronegativity difference ( $\Delta\chi$ ) is given by<sup>24</sup>

$$\Delta\chi = \sqrt{\sum_{i=1}^n c_i \left(\chi_i - \sum_{j=1}^n c_j \chi_j\right)^2} \quad (10)$$

where  $\chi_i$  or  $\chi_j$  is the Pauling electronegativity for the  $i^{\text{th}}$  or  $j^{\text{th}}$  element, respectively.

The valence electron concentration (VEC) is given by<sup>25</sup>

$$\text{VEC} = \sum_{i=1}^n c_i (\text{VEC})_i \quad (11)$$

where  $(\text{VEC})_i$  is the valence electron concentration for the  $i^{\text{th}}$  element.

Yang and Zhang proposed a new parameter from the thermodynamics origin ( $\mathcal{Q}$ ) to replace  $\Delta H_{\text{mix}}$  in the previous  $\Delta H_{\text{mix}}-\delta$  scheme. The parameter  $\mathcal{Q}$  is defined by<sup>26</sup>

$$\mathcal{Q} = \frac{T_m \Delta S_{\text{mix}}}{|\Delta H_{\text{mix}}|} \quad (12)$$

where  $T_m$  is given by

$$T_m = \sum_{i=1}^n c_i (T_m)_i \quad (13)$$

and  $(T_m)_i$  is the melting point for the  $i^{\text{th}}$  component of the alloy.

Ye *et al.*<sup>27</sup> proposed a parameter that suggests that the total configurational entropy ( $\Delta S_T$ ) can be expressed as  $\Delta S_T = \Delta S_C + \Delta S_E$ , where  $\Delta S_C$  is the configurational entropy and  $\Delta S_E$  is the excessive entropy as a function of atomic packing and their sizes. Furthermore, a single, dimensionless thermodynamic parameter ( $\phi$ ) is proposed and expressed using the following equations:

$$\Delta S_H = \frac{|\Delta H_{\text{mix}}|}{T_m} \quad (14)$$

$$\phi = \frac{\Delta S_C - \Delta S_H}{|\Delta S_E|} \quad (15)$$

where  $\Delta S_H$  is defined as the complementary entropy derived from the enthalpy  $|H_{\text{mix}}|$ .

All the relationships between the structural information and thermodynamic criteria are summarized in Fig. 3 and Table 1.

We investigate the atomic size mismatch ( $\delta$ ) with regard to its effect on the phase structure. For example, Guo *et al.*<sup>28</sup> analyzed the  $\Delta H_{\text{mix}}$  and  $\delta$  values of many HEAs and discovered that simple-solution-type HEAs fall in opposite corners of the  $\delta$ - $H_{\text{mix}}$  plot (Fig. 3a). Researchers further found that the amorphous alloy can be solidified into metallic glass by adjusting the composition. In the part of the solid-phase solution, there are three common phases (BCC, FCC, and HCP phase). In particular, different single-phase solid solutions are distributed in different regions of the  $\delta$ - $\Delta H_{\text{mix}}$  plot (Fig. 3b). Therefore, the phase of HEA can be predicted by the difference in the  $\delta$  value. In addition, Takeuchi *et al.* used a  $\delta^2$ - $\Delta H_{\text{mix}}$  plot to describe the phase selection in HEAs, as shown in Fig. 3c.<sup>29</sup> The reason for using  $\delta^2$  is intended to use another parameter that can also

represent the atomic size mismatch ( $S_\sigma$ ) to replace  $\delta$ . Compared with the  $\delta$ - $H_{\text{mix}}$  plot, it can be seen that they basically provide very similar information in terms of phase selection among different phases.

From the effective phase selection rules, it is obvious that the  $\delta$  is a very important parameter, just as it appears in all the empirical rules mentioned above. The form of  $\Omega$  can be used as another parameter to replace  $\Delta H_{\text{mix}}$  to evaluate the phase structure of HEA. As shown in Fig. 3d,<sup>26</sup> the new phase selection rule for solid solutions becomes  $\Omega > 1.1$  and  $\delta < 0.06$ . Recently, a new geometric parameter ( $\gamma$ ) was proposed to distinguish between solid solutions from intermetallic compounds (Fig. 3e).<sup>30</sup> In essence,  $\gamma$  indicates that the solid solubility in multicomponent alloys depends more on the largest and smallest atoms. The atomic size change results in intrinsic residual strains, which can be inferred by minimizing the atomic packing mismatch. These residual strains result from phase formation and theoretically should be a zero average.

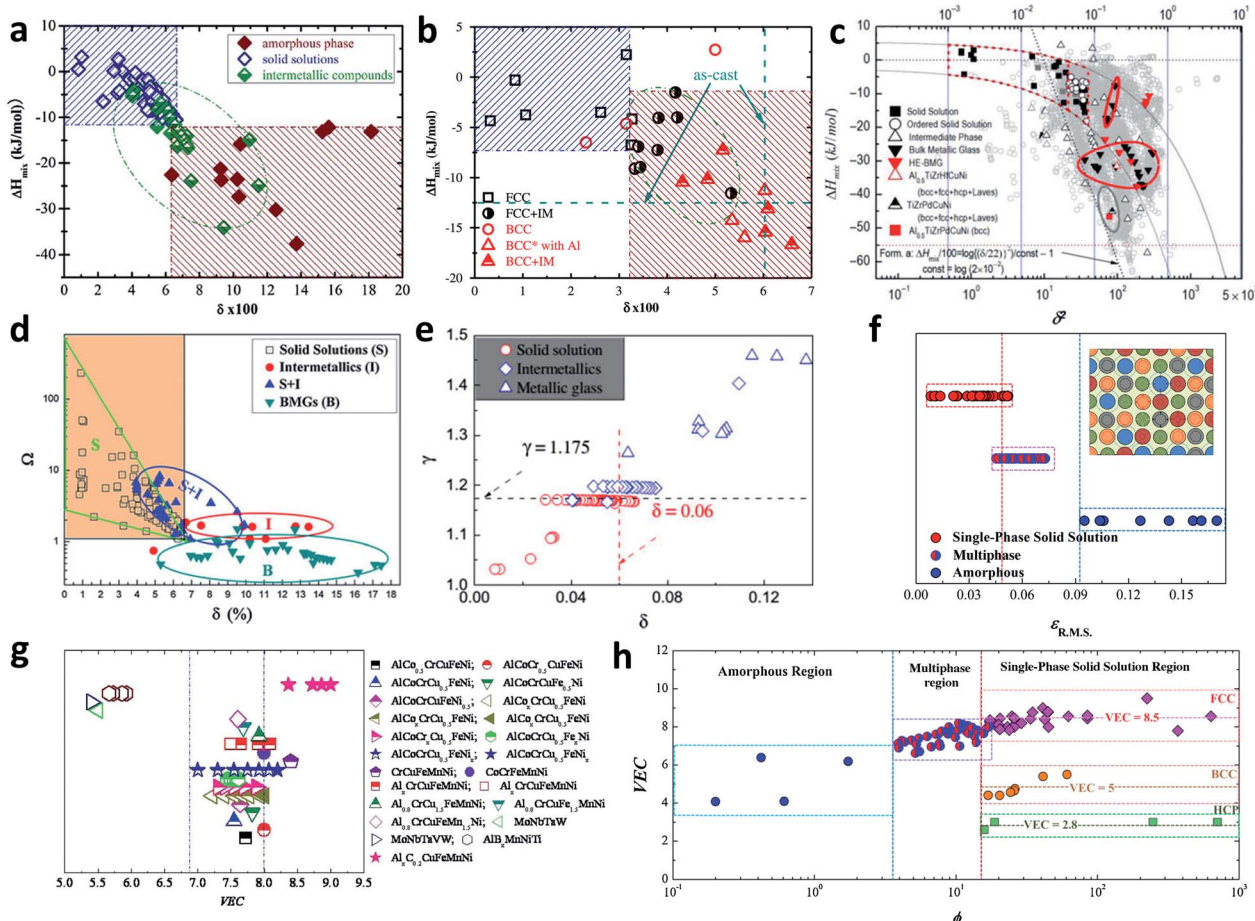


Fig. 3 (a) The  $\delta$ - $H_{\text{mix}}$  plot describing the phase selection in HEAs. Reproduced with the permission from ref. 28. Copyright © 2013 Elsevier Ltd. (b) A plot of  $\Delta H_{\text{mix}}$  vs.  $\delta$  using results from alloys heat-treated in the range of  $0.5 < T/T_m < 0.9$ . Reproduced with the permission from ref. 31. Copyright © 2014, Springer Nature. (c) The  $\delta^2$ - $\Delta H_{\text{mix}}$  plot showing the phase selection in HEAs. Reproduced with the permission from ref. 29. Copyright © 2013, MDPI. (d) The  $\Omega$ - $\delta$  plot showing the phase selection in HEAs. Reproduced with the permission from ref. 26. Copyright © 2011 Elsevier. (e) Comparison of  $\gamma$  and  $\delta$  in distinguishing solid solutions from intermetallic compounds and metallic glasses. Reproduced with the permission from ref. 30. Copyright © 2014, Elsevier Ltd. (f) Based on the inherent root-mean-squared (RMS) residual strain, the HEA of different stages were grouped. Reproduced with the permission from ref. 32. Copyright © 2015, Elsevier Ltd. (g) Relationship between VEC and the phase structures for various HEAs. Reproduced with the permission from ref. 25. Copyright © 2011, AIP Publishing. (h) The plot of VEC vs.  $\phi$  for different HEAs. Reproduced with the permission from ref. 32. Copyright © 2015, Elsevier Ltd.

Table 1 Different established thermodynamic parameters in HEA studies

Thermodynamic parameters	Proposed criteria		Stable solid solution	Ref.
	Amorphous phase	Multiphase		
$\Delta H_{\text{mix}}$	$-49 \leq \Delta H_{\text{mix}} \leq 25.5 \text{ (kJ mol}^{-1}\text{)}$		$-22 \geq \Delta H_{\text{mix}} \geq 7 \text{ (kJ mol}^{-1}\text{)}$	33
$\Delta S_{\text{mix}}$	$7 \leq \Delta S_{\text{mix}} \leq 16 \text{ (J K}^{-1} \text{ mol}^{-1}\text{)}$		$11 \geq \Delta S_{\text{mix}} \geq 19.5 \text{ (J K}^{-1} \text{ mol}^{-1}\text{)}$	33
VEC	—		FCC phase VEC $\geq 8$ BCC phase VEC $< 6.87$ HCP phase VEC around 3	32 and 33
$\Omega$	$\Omega < 1$		$\Omega \geq 1.1$	26
Atomic size mismatch ( $\delta$ )	$\delta \geq 9\%$		$6.6\% < \delta \leq 9\%$	26
RMS residual strain ( $\varepsilon_{\text{RMS}}$ )	$\varepsilon_{\text{RMS}} > 10\%$		$5\% < \varepsilon_{\text{RMS}} < 10\%$	34
$\Phi$	—		$\Phi < 1$	35
$\Phi_f$	—		$\Phi_f < 1$	35
$\phi$	When $\phi$ is too small		$1 < \phi < 20$	27

However, their fluctuation (represented by their RMS value,  $\varepsilon_{\text{RMS}}$ ) is not zero, which is related to the elastic energy storage in the HEA and drives the phase transition. When  $\varepsilon_{\text{RMS}}$  is less than 5%, a casting HEA tends to form a single-phase solid solution, an amorphous structure if  $\varepsilon_{\text{RMS}}$  exceeds 10%, and a multiphase structure if  $\varepsilon_{\text{RMS}}$  lies between 5% and 10% (Fig. 3f). However, it should be noted that the criterion based on residual strain is a necessary condition at best because the chemical effects are ignored.

It seems that the most important factor determining whether the alloy crystallizes into the BCC or FCC structure is its VEC value (the VEC of an alloy is calculated from the weighted average of the VEC values of the constituents). Guo *et al.*<sup>25</sup> summarized the relationship between the VEC and structure (Fig. 3g). Evidently, the FCC structure is stable when the VEC is larger than 8. When the VEC of the alloy is smaller than 6.87, the BCC structure tends to be stable. When the VEC value is between 6.87 and 8, the FCC and BCC structures coexist. However, till now, the mechanism of the VEC effect on phase formation has not been fully understood. Based on the work of Guo,<sup>25</sup> Fig. 3h shows the plot of VEC *vs.*  $\phi$  for numerous HEAs, including multiphase structures; metallic glasses; and single-phase FCC, BCC, and HCP solid solutions. In the region of the single-phase solid solution ( $\phi > \phi_c \approx 20$ ), FCC prevails around a VEC of 8.5, BCC around a VEC of 5, and HCP around a VEC of 2.8. However, when the HEA falls into the other phase regions ( $\phi < \phi_c$ ), this obvious difference between the phases disappears, and other effects (such as atomic-size difference) override the influence of VEC.

### 3. Novel synthesis approaches for HEAs

The discovery of HEAs is related to the study of bulk amorphous alloys. Therefore, their synthesis approaches inherit those of amorphous alloys, which can be classified into three main strategies (Fig. 4). The primary method is liquid-state synthesis, which includes arc melting,<sup>9</sup> electric resistance melting,

induction melting,<sup>36</sup> selective laser melting,<sup>37,38</sup> selective electron beam melting,<sup>39</sup> and laser-engineered net shaping (LENS).<sup>40</sup> Although they are popular for synthesizing HEAs, a very high processing temperature is needed to ensure sufficient uniformity. Furthermore, this type of production mainly leads to a dendritic microstructure, which requires extensive heat treatment to homogenize. The second way is solid-state methods, including mechanical alloying<sup>41</sup> and spark plasma sintering (SPS) for compaction.<sup>42</sup> Due to its high energy consumption and easy oxidation, sufficient uniformity might not be achieved, which needs subsequent pressing and sintering. The final one is the gas-state synthesis, including magnetron sputtering deposition,<sup>43</sup> pulsed laser deposition, atomic layer deposition, and vapor-phase deposition. These methods require complex and expensive equipment and are not easy to operate for large quantities. Therefore, the preparation of HEAs with unique properties by novel synthesis methods is an important prerequisite for the development of new applications.

#### 3.1 Electrochemical synthesis

Electrodeposition is one of the most efficient methods to grow metal nanoparticles (NPs),<sup>50</sup> using which the nucleation and growth of the NPs can be easily controlled *via* different morphologies. Moreover, the production process of electrodeposition is simple and the composition can be adjusted by changing the parameters. Besides, electro-deoxidation (or the FFC Cambridge process) is a new metallurgical method for obtaining alloys from solid oxides,<sup>51,52</sup> which has been observed amongst NiTiHf, NbTiHf, Nb<sub>3</sub>Sn, LaNi<sub>5</sub>, and TbFe<sub>2</sub>. Another attractive property is that the near-net-shape and free-standing alloy bodies can be made from oxides of suitable geometry.<sup>53</sup> Traditionally, in an electrolytic cell, a metal oxide is used as the cathode, graphite is used as the anode, and molten salt is used as the electrolyte. The key parameters for electrodeposition include the geometry, density, and porosity of the oxide precursor; operating temperature; applied potential; and duration of electrolysis.<sup>54</sup>

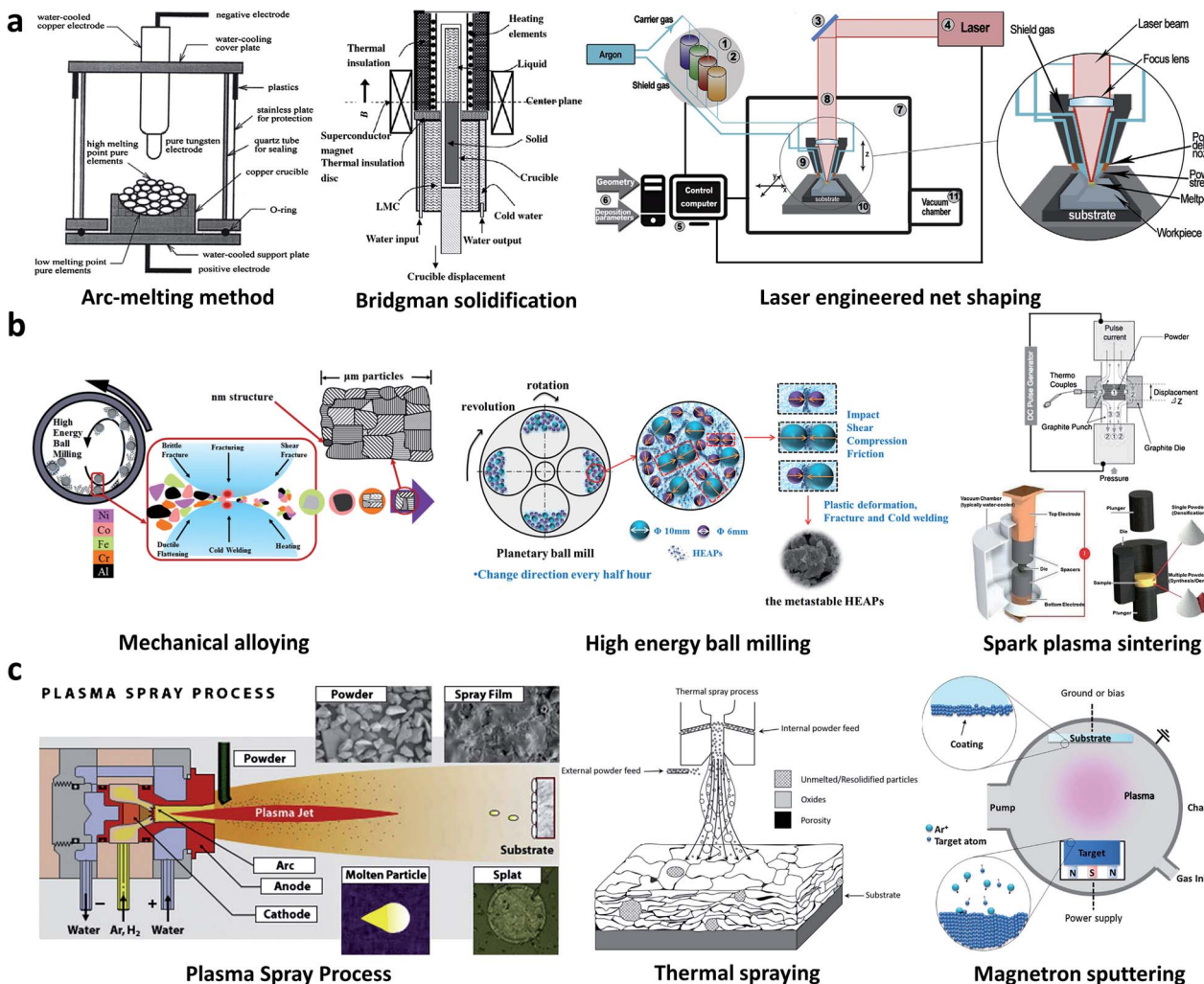


**Fig. 4** Traditional synthesis methods for HEAs. (a) Liquid-state synthesis, including arc-melting method,<sup>44</sup> Bridgeman solidification,<sup>45</sup> and laser-engineered net shaping.<sup>40</sup> (b) Solid-state synthesis, including mechanical alloying,<sup>46</sup> high-energy ball milling,<sup>47</sup> and spark plasma sintering.<sup>48</sup> (c) Gas-state synthesis, including plasma spray process, thermal spraying,<sup>49</sup> and magnetron sputtering.<sup>43</sup> Reproduced with the permission from ref. 44. Copyright © 2004, Elsevier Ltd. Reproduced with the permission from ref. 45. Copyright © 2006, Elsevier Ltd. Reproduced with the permission from ref. 46. Copyright © 2017, Elsevier Ltd. Reproduced with the permission from ref. 47. Copyright © 2019, Elsevier Ltd. Reproduced with the permission from ref. 48. Copyright © 2018, Elsevier Ltd. Reproduced with the permission from ref. 49. Copyright © 2019, Springer Nature. Reproduced with the permission from ref. 43. Copyright © 2016, Elsevier Ltd. Reproduced with the permission from ref. 40. Copyright © 2019, Springer Nature.

At first, researchers prepared an HEA in an organic electrolyte system. For example, Yao *et al.*<sup>55</sup> were the first to prepare BiFeCoNiMn HEA films by using an electrochemical method in DMF-CH<sub>3</sub>CN mixed solvents. A Bi<sub>19.3</sub>Fe<sub>20.7</sub>Co<sub>18.8</sub>Ni<sub>22.0</sub>Mn<sub>19.2</sub> amorphous film was synthesized by electrodeposition at -2.0 V, but the main FCC structure is observed after the films were annealed under an N<sub>2</sub> atmosphere (Fig. 5a). In 2011, Yao *et al.*<sup>56</sup> also reported NdFeCoNiMn HEA films using the same route. The styles of the nanostructures and surface morphologies of the deposits can be effectively controlled by changing the deposition time (Fig. 5b).

Apart from the organic electrolyte, the electrochemical synthesis of HEAs can also be conducted in a molten salt system. Sure *et al.*<sup>57</sup> demonstrated, for the first time, that HEAs can be electrochemically synthesized in molten salt (Fig. 5c).

This cathodic polarization was conducted in an electrolytic cell in which premixed-metal oxides (TiNbTaZrHf and TiNbTaZr refractory alloys) were present in molten CaCl<sub>2</sub> salt at 1173 K. This approach has the following advantages: more cost affordability due to the oxide precursor and considerably mild synthesis temperature. Furthermore, the process of electrochemical synthesis would be feasible and attractive in the synthesis of cheap HEAs containing Fe, Co, Ni, and Cr. For example, Wang *et al.*<sup>58</sup> prepared powdery FeCoNiCrMn HEA with the FCC structure in addition to the uniform distribution of components by one-step electrolysis in CaCl<sub>2</sub> molten salt at 1123 K (Fig. 5d). Although the melting step was unnecessary during electrolysis, a certain number of carbon dopants were introduced into the alloy due to the dissolution of the graphite anode. In order to explore the mechanism during electrolysis,

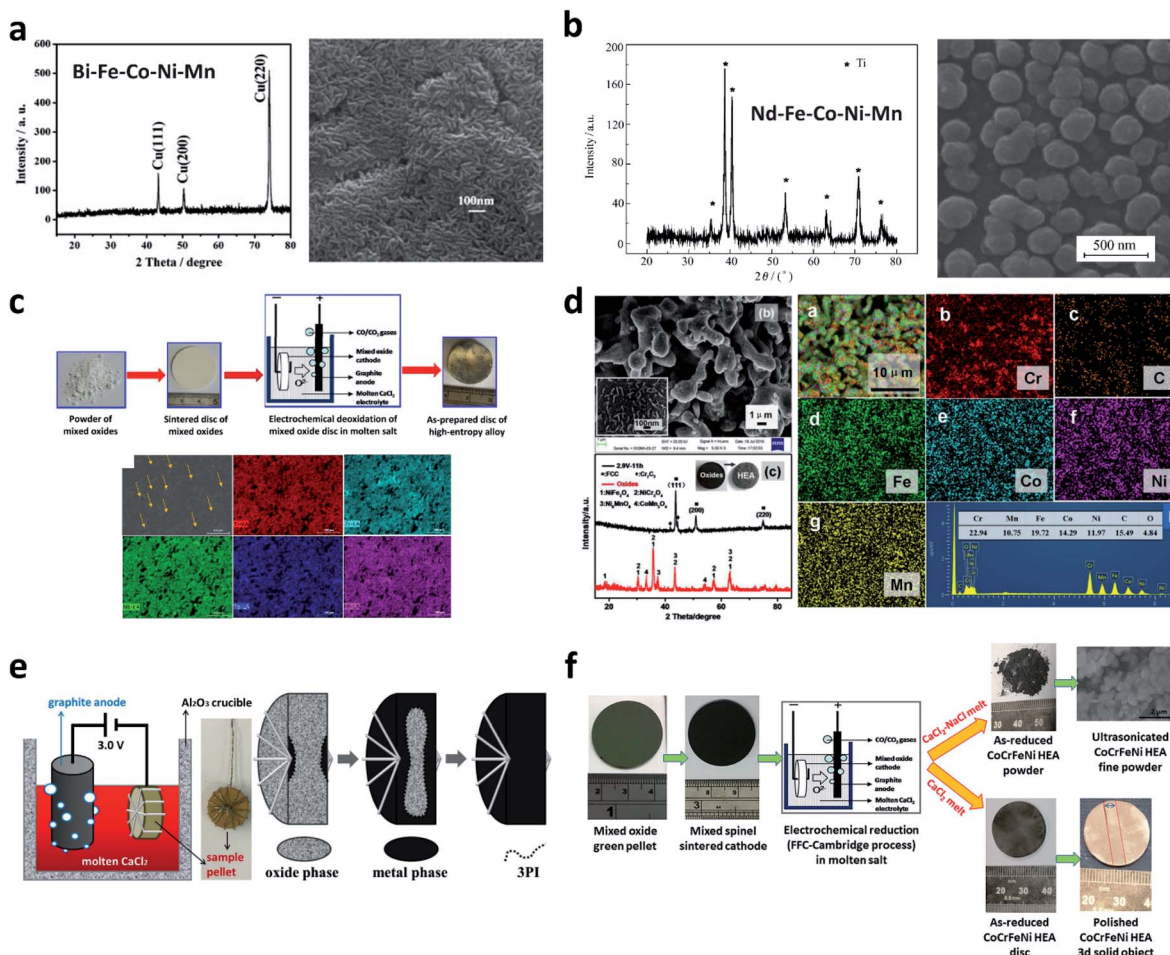


**Fig. 5** XRD pattern and SEM image of Bi–Fe–Co–Ni–Mn HEA<sup>55</sup> (a) and Nd–Fe–Co–Ni–Mn HEA<sup>56</sup> (b) in an organic system. (c) Schematic of the electrochemical synthesis of TiNbTaZrHf and the corresponding EDX area maps.<sup>57</sup> (d) SEM image, XRD patterns, and elemental distribution mapping of the FeCoNiCrMn HEA in molten CaCl<sub>2</sub>.<sup>58</sup> (e) Schematic of the propagation mechanism on the surface of the oxide pellet.<sup>59</sup> (f) Electrochemical synthesis of CoCrFeNi HEA in CaCl<sub>2</sub>–NaCl and pure CaCl<sub>2</sub>.<sup>60</sup> Reproduced with the permission from ref. 55. Copyright © 2008, Elsevier Ltd. Reproduced with the permission from ref. 56. Copyright © 2008, Elsevier Ltd. Reproduced with the permission from ref. 57. Copyright © 2017, Elsevier Ltd. Reproduced with the permission from ref. 58. Copyright © 2017, The Electrochemical Society. Reproduced with the permission from ref. 59. Copyright © 2018, The Electrochemical Society. Reproduced with the permission from ref. 60. Copyright © 2018, Elsevier Ltd.

Jiao *et al.*<sup>59</sup> achieved homogeneous AlCrNbTaTi HEAs *via* a simple electrochemical approach. The obtained results suggest that the reduction process complies with a three-phase interline propagation mechanism (Fig. 5e). This electro-deoxidation reaction is found to initiate at the interline of nickel wire, molten salt, and oxide pellet surface; subsequently, it proceeds into the interior of the oxide pellet. Sure *et al.*<sup>60</sup> synthesized equiautomic CoCrFeNi HEA by means of electro-deoxidation in molten eutectic CaCl<sub>2</sub>–NaCl and pure CaCl<sub>2</sub> molten salt (Fig. 5f). This process requires less energy consumption in the molten salt mixture than pure molten salt.

### 3.2 Carbothermal shock (CTS) synthesis

HEAs have been primitively synthesized *via* melting or plasma methods that produced atomically mixed phases. In comparison, nanostructured alloys are often prepared *via* wet chemical synthesis by co-reducing metal salts with capping agents that

prevent crystal growth and aggregation.<sup>61</sup> However, the types of synthesized alloys are limited due to the different reaction rates of the precursors.<sup>62</sup> To date, only a limited number of HEAs have been explored because it is difficult to blend elements with various properties and the constraints induced by faster cooling rates. In addition, downsizing HEAs to the nanoscale is a dispiriting task using traditional methods. Therefore, developing a synthesis strategy that can precisely control the composition, particle size, and phase of alloys can yield many novel HEAs with unprecedented functionalities.

Multimetallic NPs can be used in various fields, but effective strategies for synthesizing such structures are still lacking. Therefore, Chen *et al.*<sup>63</sup> were the first to formulate systematic studies of individual poly-elemental NPs based on their previous work,<sup>64</sup> where the composition and size could be precisely controlled and the formation of the microstructure could be understood. They synthesized HEAs containing five

elements (Au, Ag, Co, Cu, and Ni) *via* a polymer nanoreactor-mediated method (Fig. 6a and b). Through this work, the understanding of alloy formation and phase segregation at the nanoscale could be achieved, and routes for developing HEA nanostructures that are difficult to obtain *via* conventional methods are also explored.

The controllable incorporation of multiple immiscible elements into a single NP has immeasurable scientific and technological value; however, achieving this using conventional synthesis methods is still a challenge. In order to prepare multi-metallic NPs, Yao *et al.*<sup>65</sup> presented a common path of

synthesizing alloys comprising up to eight elements into single-phase NPs (Fig. 6c and d) by thermally shocking metal salt mixtures loaded onto carbon supports. The corresponding parameters were as follows: temperature, 2000 K; time, 55 ms; rate,  $10^5$  K s<sup>-1</sup>. Multicomponent NPs with the desired composition, size, and phase were synthesized by tuning the above CTS parameters. Fig. 6e shows the formation mechanism and size control kinetics of NPs at higher temperatures at which a high O<sup>\*</sup> concentration accelerates the vigorous metabolism of frequent catalyst activities. Therefore, the liquid metal movement driven by O<sup>\*</sup> harvesting allows different droplets to

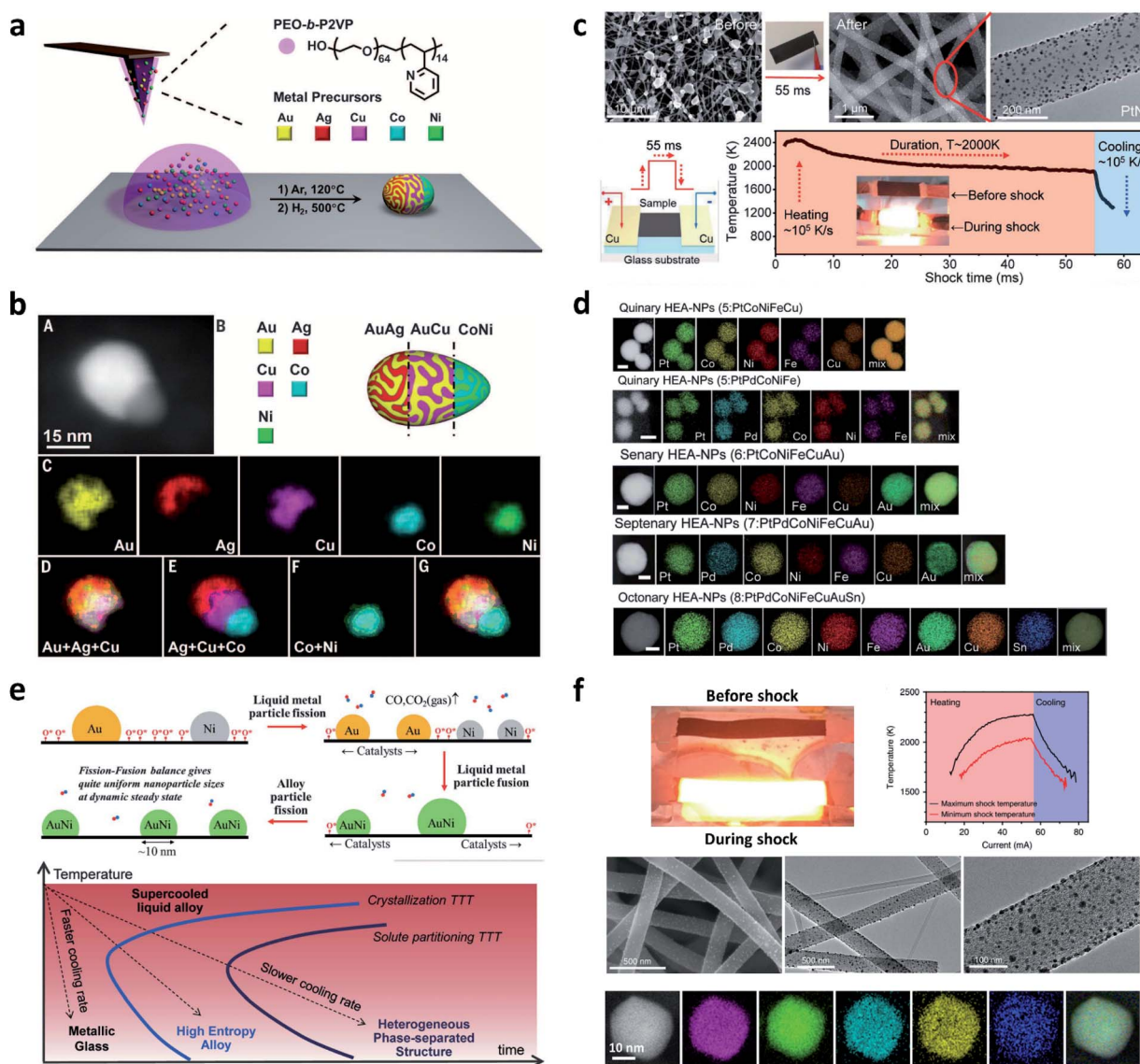


Fig. 6 (a) Schematic of the preparation process for poly-elemental NPs *via* the polymer nanoreactor-mediated method. (b) EDS elemental mapping of the HEA NPs and phase-separated NPs, showing the distribution of each metal. Reproduced with the permission from ref. 63. Copyright © 2016, American Association for the Advancement of Science. (c) Microscopy images of precursors on the CNF support, and the synthesized PtNi NPs after CTS. The process of sample preparation and temporal evolution. (d) HAADF images and STEM elemental maps of HEA NPs. (e) Schematic of the mechanism for synthesizing uniformly dispersed HEA NPs. The kinetics of metallic glass, HEA, and phase-separated NPs as a function of cooling rate. Reproduced with the permission from ref. 65. Copyright © 2018, American Association for the Advancement of Science. (f) Digital images of the samples before and during CTS synthesis. Representative microstructures of the obtained HEA-Co<sub>25</sub>Mo<sub>45</sub> NPs loaded onto carbon nanofibers. Reproduced with the permission from ref. 68. Copyright © 2019, Springer Nature.

continually meet and fuse into single-phase alloys during the CTS process. Meanwhile, the high-entropy state of the liquid metals produces single-phase solid-solution NPs and prevents the NPs from aggregating *via* rapid quenching. Skrabalak *et al.*<sup>66</sup> summarized the above CTS method, which involves thermally shocking mixed-metal salt precursors loaded on carbon supports. Interestingly, the input ratio of the metal could be extended to the product, and this synthesis approach can be easily promoted. Wu *et al.*<sup>67</sup> also praised this work. Xie *et al.*<sup>68</sup> synthesized single-phase CoMoFeNiCu NPs with precise control over the Co/Mo atomic ratio enabled by the CTS process (Fig. 6f). They demonstrated that the miscibility limitation in bimetallic Co–Mo alloys could be broken by adjusting the Co/Mo ratio of CoMoFeNiCu NPs.

The synthesis of unstable alloy NPs and carbonaceous nanomaterial could cause uneven mass and charge transfer at the interface of the electrode and electrolyte. In order to load the alloy NPs on the support, Xu *et al.*<sup>69</sup> reported the CTS synthesis of FeNiCoMnMg and FeNiCoMuCu NPs on super-aligned electrospun carbon nanofibers. Only when coupling a self-designed collector and a suitable CTS current direction, nanostructured HEAs could be precisely prepared. This work highlights the role of the aligned CNFs, which accelerate the electron transport, further facilitating the formation of HEA NPs.

### 3.3 Plasma-related synthesis

HEAs NPs have been confirmed to exhibit enhanced performance in biomedicine, gas sensing, and catalysis. Therefore, fabricating bulk HEAs into NPs is important. Until now, many traditional metallurgy methods (arc-melting or induction-melting method) are still popular in the industry. However, these approaches produce either phase-segregated or inhomogeneous microstructures, and they cannot produce HEA NPs. Besides the wet chemical synthesis technique and CTS method, plasma discharge is another adequate strategy to synthesize nanoalloys.<sup>70</sup> Therefore, plasma-related synthesis can be a suitable alternative method.

HEAs NPs or quantum dots with superior properties have represented various applications, but synthesizing HEA NPs is difficult in the simultaneous reduction of many kinds of precursors *via* the co-reduction reaction. Wu *et al.*<sup>71</sup> were the first to fabricate HEA NPs from bulk alloys using spark discharge in water. The TEM and elemental mapping data confirm that the NPs have uniform size and elemental distribution. Mao *et al.*<sup>72</sup> synthesized spherical CoCrCuFeNi NPs with size in the range of 80–120 nm by a modified plasma arc discharge method. Because of the evaporating pressure and molar mass of the raw materials, the components of the raw materials and as-prepared NPs are significantly different. Xia *et al.*<sup>73</sup> prepared MoNbTaVW and AlCuCrTaTi HEA thin films *via* arc deposition on polyimide substrates and studied their electromechanical properties. Park *et al.*<sup>74</sup> fabricated spherical WTaMoNbV refractory HEAs by milling and spheroidizing using inductively coupled thermal plasma. Using this process, spherical WTaMoNbV HEA powders with  $d_{50}$  of 45.1  $\mu\text{m}$  could be successfully fabricated. Lee *et al.*<sup>75</sup> fabricated spherical V-

Nb–Mo–Ta–W HEA powder with the BCC phase using hydrogen embrittlement and spheroidization by thermal plasma. After treating with inductively coupled thermal plasma, the shape of the HEA powder was transformed from angular to spherical, along with a  $d_{50}$  value of 28.0  $\mu\text{m}$ .

### 3.4 Microwave-assisted synthesis

Since the pioneering work of Roy *et al.*,<sup>76</sup> heating powdery metals by microwaves has become popular and used in many fields of metallurgy because of its characteristic selective and volumetric heating and sintering enhancement.<sup>77</sup> Microwave-assisted synthesis has already been used for preparing intermetallics.<sup>78</sup> The advantages of applying microwaves are high purity of the products,<sup>79</sup> rapid ignition during the reaction,<sup>80</sup> and ease of controlling their microstructures. Given these premises, exploring a new microwave-assisted technology for the synthesis of HEA can overcome the limitations of the current smelting technology.

Veronesi *et al.*<sup>81</sup> were the first to prepare FeCoNiCuAl, FeCrNiTiAl, and FeCoCrNiAl<sub>2.5</sub> HEAs by heating the metal precursor mixtures with microwaves at a frequency of 2450 or 5800 MHz. This microwave-assisted technology can overcome the disadvantages of melting technologies (easy-to-form defects) and solid-state methods (consuming plenty of time). Using this new method, it is possible to control the cooling rate of the as-prepared HEAs, particularly in the ignition and sustenance of such reactions. Veronesi *et al.*<sup>82</sup> also produced Si-modified Mn<sub>25</sub>Fe<sub>x</sub>Ni<sub>25</sub>Cu<sub>(50-x)</sub>, ( $x = 25, 30, 35$ , and 40) HEAs by the rapid heating of the metallic mixtures at 2450 MHz under an Ar atmosphere. With the assistance of a SiC absorber, the compact material experienced direct heating *via* microwave absorption as well as indirect heating *via* the auxiliary absorber. Lan *et al.*<sup>83</sup> fabricated the AlFeCuCrNiTiB HEA composites reinforced by TiB<sub>2</sub> particles by the microwave heating method. The distribution state of TiB<sub>2</sub> changes with the volume fraction of the reinforcement. When the volume fraction of the reinforcement was 10%, it afforded regular morphology with uniform distribution. When the volume fraction of the reinforcement increases to 15%, TiB<sub>2</sub> partially aggregates in the matrix.

### 3.5 Combustion-assisted synthesis

Extensive studies toward synthesizing HEAs have been recently conducted, which make them potentially serve as functional materials. The sol–gel auto-combustion technique is a rapid and economical method for the preparation of particulates, and it has been widely generalized for the synthesis of various alloy NPs at the atomic level.<sup>84</sup> Combustion-assisted synthesis relies on the highly exothermic aluminothermic reactions to prepare HEAs instead of heating in a furnace, and HEAs can be separated from the ceramic ingot under ultrahigh gravity.<sup>85</sup> Although this method was confirmed to be effective in preparing many ceramic materials, it was rarely applied in HEAs until now. In contrast to the traditional sintering method, combustion synthesis is a cheap and facile preparation method that employs a self-sustaining combustion reaction under a high-gravity field, as well as shortens the processing time.

Niu *et al.*<sup>86</sup> were the first to propose a sol-gel auto-combustion technique to synthesize CoCrCuNiAl HEA NPs with an FCC and BCC structure and a grain size of 14 nm (Fig. 7a). During the reaction, chelation between citric acid and metal ions is the *in situ* chemical reaction oxidized by nitrate ions. Li *et al.*<sup>87</sup> presented a new method of combustion synthesis under high gravity for preparing Al<sub>x</sub>CoCrFeNi HEAs (Fig. 7b). The obtained results reveal that the crystal structures evolved from FCC to BCC structures with an increase in the Al content, which is in agreement with earlier works. Meanwhile, the microstructure is not only related to the Al content, but also affected by high gravity. Furthermore, CoCrFeNiMn-type<sup>88</sup> and C-containing CoCrFeNiMn-type<sup>89</sup> HEA were produced by self-propagating combustion synthesis.

Apart from the HEA component, combustion synthesis can also be used to synthesize ceramic/metal composites. For example, Wang *et al.*<sup>90</sup> prepared a ceramic/metal composite (TiC-TiB<sub>2</sub>/Al<sub>0.3</sub>CoCrFeNi) by this synthesis method under an

ultrahigh gravity field (Fig. 7c). After the combustion reaction, the two components are separated because of the different densities, which leads to the gradient distribution of ceramics dispersed in the HEA matrix. Zhang *et al.*<sup>91</sup> fabricated innovative WC/CoCrFeNiAl<sub>0.2</sub> composites by an economical and effective combustion synthesis method with inexpensive metal oxides as the raw materials (Fig. 7e). The interface between the HEA and ceramic particles was apparent; further, the particles were closely combined. A relative density of more than 99% could be achieved for the composites after the upregulation of the gravity field (Fig. 7f). Rogachev *et al.*<sup>92</sup> also prepared TiC-HEA composites *via* the same method. Self-sustained synthesis begins from an exothermic reaction ( $Ti + C = TiC$ ) and propagates across the samples in the form of a combustion wave. Following the above process, the various metal powders melt and finally produce multicomponent CoCrFeNiMe (Me = Mn, Ti, or Al) HEA as a binder phase.

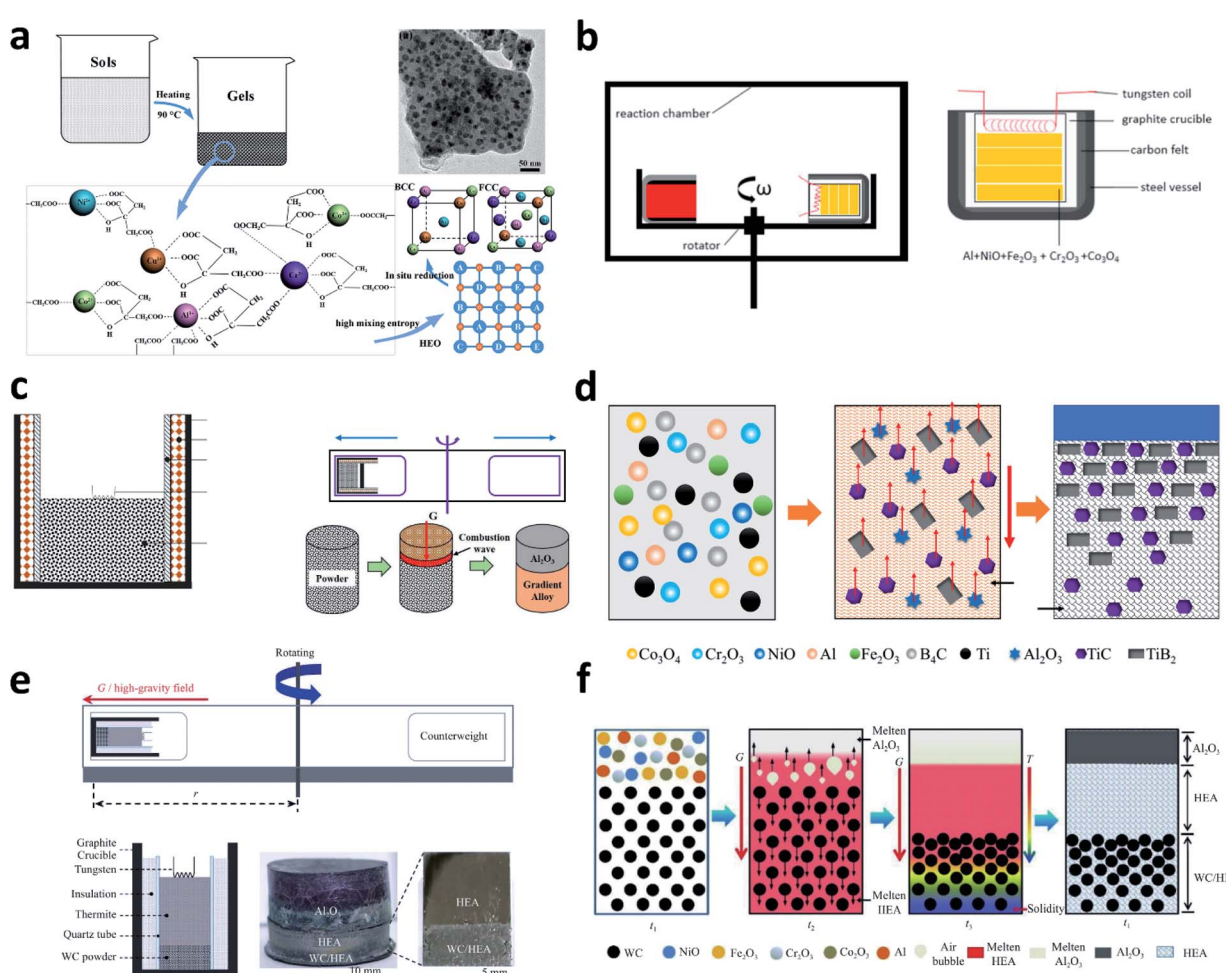


Fig. 7 (a) Schematic of the sol–gel auto-combustion process and the microstructure of the dried gel. Reproduced with the permission from ref. 86. Copyright © 2017, Springer Nature. (b) Schematic of the combustion synthesis of Al<sub>x</sub>CoCrFeNi HEAs. Reproduced with the permission from ref. 87. Copyright © 2017, Elsevier Ltd. (c) Schematic of the combustion synthesis of TiC–TiB<sub>2</sub>/Al<sub>0.3</sub>CoCrFeNi under high gravity. Reproduced with the permission from ref. 90. Copyright © 2018, Elsevier Ltd. (d) Reaction mechanism of TiC–TiB<sub>2</sub>/Al<sub>0.3</sub>CoCrFeNi. (e) Schematic of the combustion synthesis under ultrahigh gravity; the other figures are the macrostructure and photographs of CoCrFeNiAl<sub>0.2</sub> and WC/CoCrFeNiAl<sub>0.2</sub> composites. (f) Formation mechanism of the gradient distribution of ceramic in the HEA matrix. Reproduced with the permission from ref. 91. Copyright © 2020, Springer Nature.

### 3.6 Laser-related synthesis

HEAs have been recently developed as one of the most important materials in fundamental research and application. However, most of the research has been focused on the HEA bulk rather than HEA NPs, because a scalable and straightforward synthesis for HEA NPs is not available. Although Rekha *et al.*<sup>93</sup> immobilized CoCrCuFeNi-HEA NPs on graphene by mechanical ball milling, this solid-state synthesis could not meet the goal of their chemical distributions. The plasma-related synthesis of CoCrCuFeNi NPs could be achieved in a reactive gas atmosphere,<sup>72</sup> however, this method must be in the gas phase and it can only produce HEA NPs with a large particle size. By sputtering CoCrFeMnNi ingot into an ionic liquid, ultrasmall NPs could be obtained.<sup>94</sup> However, expensive ionic liquids and complicated methods are not conducive to practical applications. Therefore, the synthesis of scalable and isolated colloidal HEA NPs with the desired composition and microstructure has remained undeveloped.

The formulation of synthesis methods to control the chemical composition and phase composition of colloidal HEA NPs can bring novel prospects for the new application of nanoalloys. Waag *et al.*<sup>95</sup> developed colloidal CoCrFeMnNi NPs by the ultrafast laser synthesis method (Fig. 8a). The overall synthesis comprised three steps. The first step is ultrashort-pulsed laser irradiation of the HEA bulk. Following the atomization of the bulk to form a plume, the nucleation and condensation of the ablated matter were generated in the liquid and the colloidal HEA NPs finally stabilized in ethanol. The colloidal state of

ultrasmall (<5 nm) HEA NPs was verified by centrifugal size measurement techniques (Fig. 8b). Furthermore, multiple characterizations confirmed the FCC structure as well as the uniform distribution of elements, as shown in Fig. 8c–e. The isolated and colloidal feature of CoCrFeMnNi NPs without the assistance of stabilizers is capable of immobilizing the as-prepared NPs on many kinds of substrates. Interestingly, this approach can be scaled up to industrial applicability with a yield of 3 g h<sup>-1</sup>. In the future, the ability to rapidly produce HEA by changing the alloy composition, combining the target and environment, and immobilization substrate make laser-based synthesis superior for screening nanomaterials.

### 3.7 Other synthesis methods

Nanostructured alloys have remarkable properties; however, it is difficult to mutually fuse various metals, which limits the composition of catalytic design. It is well known that nanoalloys cannot be obtained by the liquid-phase reaction; therefore, it often requires exotic shock synthesis or severe decomposition reactions. However, the above methods are only effective under laboratory conditions, which greatly limits its practical applications. Singh *et al.*<sup>96</sup> produced isolated NiFeCrCuCo NPs by the wet chemical synthesis method. As per the analysis data, the as-synthesized NP exhibited the FCC structure with an average size of 26.7 nm. A compositional analysis of the NPs reveals that all the elements were uniformly distributed. Bondesgaard *et al.*<sup>97</sup> reported a universal solvothermal method to synthesize HEAs. Quinary HEA systems were synthesized by changing the solvents and precursors. This method offers a facile and universal preparation method to synthesize unnamed HEAs over their entire composition range, which may allow a detailed adjustment of the performance of the nanoalloy catalyst.

HEA NPs with great technical potential are a worthwhile family of materials. However, strategies for preparing homogeneously dispersed NPs on granular substrates (such as carbon,  $\gamma$ -Al<sub>2</sub>O<sub>3</sub>, and zeolite) have remained underdeveloped even though they are very important for practical applications. Gao *et al.*<sup>98</sup> developed a fast moving bed pyrolysis (FMBP) strategy to synthesize HEA NPs (MnCoNiCuRhPdSnIrPtAu) loaded onto many kinds of matrixes (Fig. 9a and b). This strategy ensures that the mixed-metal precursors are pyrolyzed at higher temperatures, resulting in high monomer supersaturation, small nuclear size, and highly dispersed HEA NPs on the carrier. The parameters and mechanism of the FMBP method have been carefully investigated. Apart from the above method, another aerosol-droplet-mediated synthesis technique also enables the batch preparation of particulate HEAs. For example, Yang *et al.*<sup>99</sup> reported an aerosol-droplet-mediated scalable synthesis method of HEA NPs, which have an atomic-level mixture of immiscible metal elements (Fig. 9e). Aerosol droplets of 1  $\mu$ m are formed by atomizing the aqueous solution of metal salts, which lead to the decomposition of precursors and freezing of metal atoms when subjected to rapid heating and quenching.

Generally speaking, the new preparation methods are still a continuation of the traditional liquid-phase, solid-phase, and

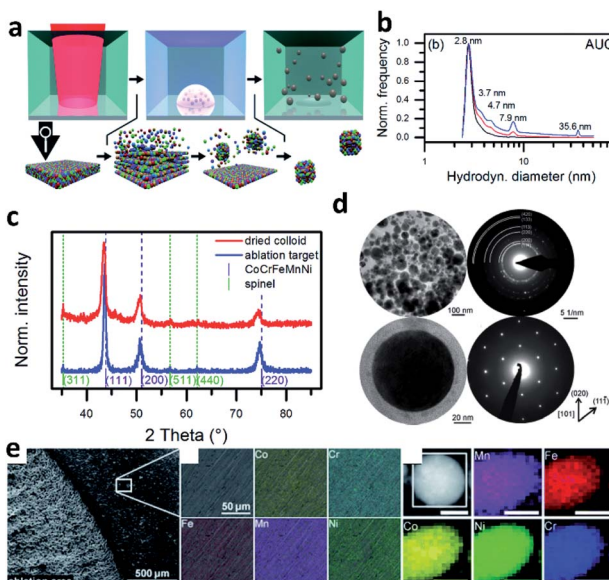
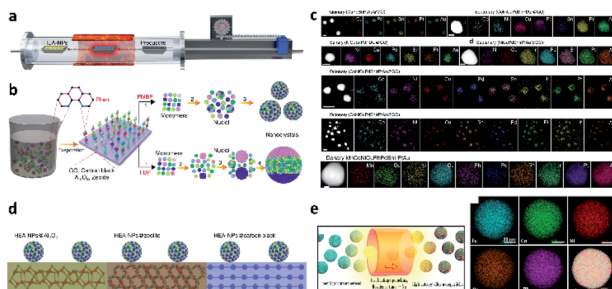


Fig. 8 (a) Schematic of the laser-related synthesis of HEA NPs. (b) Relative number, surface, and volume frequencies vs. the hydrodynamic diameter measured by analytical ultracentrifugation. (c) XRD patterns of the ablation target and as-prepared colloidal HEA NPs. (d) TEM images of CoCrFeMnNi NPs and the corresponding SAED results. (e) SEM image and elemental maps of a nonablated target, and STEM images and elemental maps of a single NP. Reproduced with the permission from ref. 95. Copyright © 2019, Royal Society of Chemistry.



**Fig. 9** (a) Schematic of the FMBP device for synthesis of HEA NPs. (b) Comparison of processes for the synthesis of HEA NPs and phase-separated NPs by different methods. (c) HAADF and elemental maps for FMBP-synthesized HEA NPs. Reproduced with the permission from ref. 98. Copyright © 2020, Springer Nature. (d) Schematic of HEA NPs loaded onto  $\gamma$ -Al<sub>2</sub>O<sub>3</sub>, zeolite, and carbon black. (e) Aerosol-droplet-mediated HEA NPs as a scalable synthesis technology. Reproduced with the permission from ref. 99. Copyright © 2020, American Chemical Society.

gas-phase methods. However, different from the traditional methods, the energy source for decomposing metallic raw materials is not limited to thermal energy and mechanical energy. In addition, the HEAs synthesized by these new methods could have a smaller size, which endows these materials with endless possibilities. However, it is evident that the bottleneck for the functional application of such materials lies in their nano and quantum effects, active sites of defects, *etc.*

## 4. Advanced functional applications of HEAs

As one of the three major material systems in the world, alloys have been widely used in various engineering fields, such as high-strength building materials and corrosion-resistant coating materials. With the emergence of HEAs in the early twenty-first century, their excellent mechanical properties have made them widely investigated and applied in a large number of engineering fields. For example, HEAs have ultrahigh strength and toughness at higher temperatures. In addition, in a variety of harsh environments, they can maintain stability and extremely long lifespan. In the past decade, the unique functional properties of HEAs have attracted increasing attention and their applications in many scenarios have been expanded (Fig. 10). In the following section, we will mainly focus on the application of HEAs as advanced energy and environmental materials.

### 4.1 Environmental protection

Nowadays, azo dye wastewater from textile, rubber, food, plastic, and other industries has become a serious environmental problem, which poses a grave threat to human health.<sup>100,101</sup> The primary obstacle to degrade these dyes is their complex and stable chemical structures containing double bonds of “–N=N–”.<sup>102</sup> Besides, azo dye seriously affects the photosynthesis of aquatic plants or the growth of fish. More

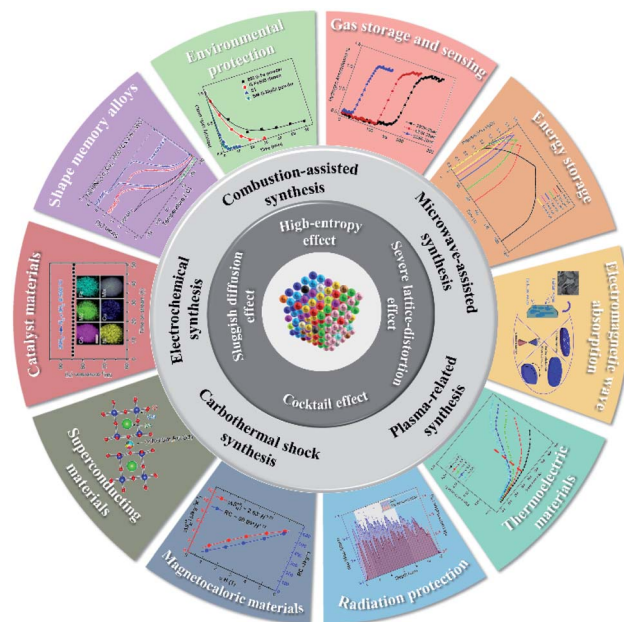


**Fig. 10** Based on the unique properties of HEAs and the new preparation methods recently developed, their energy and environmental applications in various fields have been summarized.

seriously, it is difficult to remove azo dyes from aqueous solutions.<sup>103</sup> Therefore, the detoxification of azo dyes has been a hot issue in the academic field in recent years. Many kinds of methods have been applied toward the treatment of azo dyes.<sup>104</sup> In terms of catalytic treatment, metals (Mg, Fe, Al, or Zn) have the advantages of environmental friendliness, low cost, and high efficiency, and they have broad application prospects in the decolorization of azo dyes. However, they have many disadvantages, namely, Mg is overconsumed because of its poor corrosion resistance, while Fe can easily agglomerate and lacks stability. Therefore, it is imminent to develop alloy materials that are environmentally friendly, inexpensive, have robust stability, and have strong decolorization ability toward azo dyes. The effect of alloy-based materials for the removal of contaminants is mainly due to their adsorption function.

HEAs, as an efficient decolorizing material for azo dyes, have attracted increasing attention. The degradation efficiency of Direct Blue 6 (DB6) by a new type of AlCoCrTiZn HEA synthesized by mechanical alloying is comparable with the best metallic glass reported so far.<sup>105</sup> It has a lower activation energy barrier ( $30 \text{ kJ mol}^{-1}$ ) and it can easily degrade azo dye compared with amorphous Fe-based catalysts (Fig. 11a and b). Its superior performance can be attributed to its unique atomic structures, which include residual stress, large specific surface area, chemical composition effect, and severe lattice distortion. Wu *et al.*<sup>106</sup> synthesized AlCrFeMn HEA *via* a ball-milling method for degrading the azo dye DB6. The results show that the decolorization rate of this HEA toward DB6 is 3 times higher than those for MgZn-based powders and AlCoCrTiZn (Fig. 11c). The oxidation-reduction reaction, special alloy composition, and unique crystal structure mostly contribute to the process of decolorization. Based on the excellent performance of

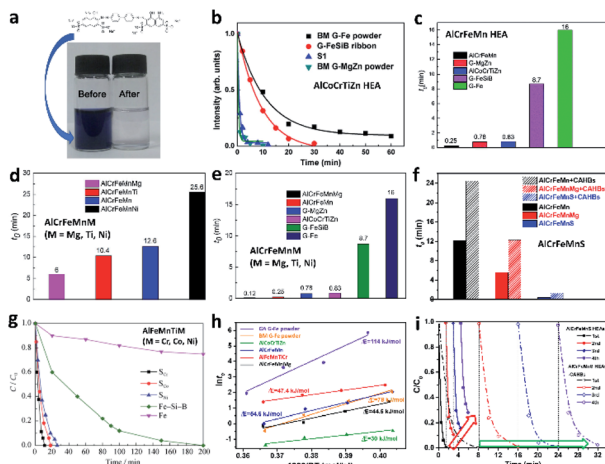


**Fig. 11** (a) Appearances of the DB6 solution before and after degradation by AlCoCrTiZn HEA. (b) Degradation performances of the AlCoCrTiZn HEA and the contrast sample. Reproduced with the permission from ref. 105. Copyright © 2016, Springer Nature. (c) Comparison of the reaction efficiencies of AlCrFeMn and other materials. Reproduced with the permission from ref. 106. Copyright 2018, Royal Society of Chemistry. (d) Contrast of the decoloration performance of AlCrFeMnM ( $M = Mg, Ti, Ni$ ). (e) Comparison of the reaction efficiencies of AlCrFeMnM ( $M = Mg, Ti, Ni$ ) and other materials. Reproduced with the permission from ref. 107. Copyright © 2019, Elsevier. (f) Comparison of the AlCrFeMnMg and AlCrFeMnS HEAs and their composites. Reproduced with the permission from ref. 109. Copyright © 2019 IOP Publishing Ltd. (g) Degradation efficiency of AlFeMnTiM ( $M = Cr, Co, Ni$ ). Reproduced with the permission from ref. 108. Copyright © 2019, Springer Nature. (h) Kinetic data of the decoloration of DB6 by various HEAs. (i) Decoloration performances of bare HEA powders and HEA-CAHBs in four cycles.

AlCrFeMn HEA, the fifth elements (Mg or Ti or Ni) were added to improve the decoloration efficiency.<sup>107</sup> Both Mg and Ti are beneficial for improving the decolorization properties, while Ni plays a negative role (Fig. 11d and e). Except for the above AlCrFeMn-based HEA system, Wu *et al.*<sup>108</sup> also developed new AlFeMnTiM ( $M = Cr, Co, Ni$ ) HEAs applied in the degradation of DB6 using mechanical metallurgy. The degradation efficiency of AlFeMnTiCr is about 19 times higher than that of Fe–Si–B amorphous ribbons and more than 100 times that of commercial Fe powder (Fig. 11g). The considerable degradation performance of the material can be attributed to the galvanic cell effect and unique crystal structure.

In the actual process of dye degradation, the adsorption capacity and adsorption rate of adsorbents are not the only factors to be considered, but also the recovery and reuse of adsorbents, particularly considering the cost issue. Although the rate of dye degradation by HEA is very fast, it is difficult to recover the adsorbent. Therefore, researchers need to pay attention to the selection and influence of carriers. They are required to be nontoxic, biocompatible, cheap, and easy to produce. Wu *et al.*<sup>109</sup> also found that ball-milled AlCrFeMnM ( $M = Mg, S$ ) HEAs have significant decolorization properties toward DB6 (Fig. 11f). Due to the rapid reaction between the powder HEAs and DB6, controlling the reaction rate is difficult, resulting in the loss of most HEA powder and poor recyclability.

Therefore, bare HEA powders were immobilized in the calcium alginate hydrogel balls (CAHBs) using electrostatic spray and microfluidics. The reaction of the AlCrFeMnS HEA-CAHBs with DB6 can be recycled four times without obvious activity loss and catalyst loss (Fig. 11i). In terms of the recycling ability of HEAs, Wu *et al.*<sup>110</sup> reported three kinds of Co-free HEA powders (AlCrFeMn, AlCrFeNi, and FeCrNiMn) synthesized by ball milling and investigated their prominent decolorization performances for azo dyes. Although AlCrFeMn shows the best decolorization efficiency, it is not easy to be recycled. Therefore, they immobilize bare HEA powders in calcium alginate beads (CABs) by electrospray and microfluidics.

Through four cycles of reaction, the loss rate of the HEA powders could be reduced from 40 to 5 wt% and the HEA-CAHBs shows better stability and easier separation than that of bare HEA powders. These works provide a new practical idea for the decolorization of azo dyes using HEAs and promote their industrial application.

## 4.2 Gas storage and sensing

Recently, hydrogen has become renowned as a renewable and sustainable fuel to reduce fossil fuel consumption. However, hydrogen storage is still a bottleneck for practical applications. Among all kinds of storage materials, alloys have the advantages of high bulk density, good safety, and good reversibility, which play an important role. In particular, alloys containing BCC and Laves phases have high hydrogen reaction activity and are considered to be promising hydrogen storage materials.<sup>111</sup>

In 2010, Kao *et al.*<sup>112</sup> were the first to find that the CoFeMnTiVZr HEA with C14 Laves phase could absorb and desorb up to 1.6 wt% of H<sub>2</sub> at room temperature. The effect of the chemical composition of the alloy on H<sub>2</sub> storage can be revealed by the lattice constant, element segregation, and hydride formation enthalpy. The high-entropy effect promotes the formation of a single C14 Laves phase, and the maximum H<sub>2</sub> storage capacity is closely correlated with the formation enthalpy of H<sub>2</sub> and the alloy. Hence, multicomponent HEAs with BCC and/or Laves phases offer numerous opportunities for superior H<sub>2</sub> storage in practical applications.

Kunce *et al.* synthesized ZrTiVCrFeNi<sup>40</sup> and TiZrNbMoV<sup>113</sup> HEAs using the LENS technology. ZrTiVCrFeNi has a two-phase structure, which is mainly composed of the C14 Laves phase and a small amount of  $\alpha$ -Ti solid solution. The Laves phase plays an important role in hydrogen storage. The pressure-composition-temperature (PCT) isotherms were measured after annealing at 500 °C for 2 h in a vacuum. The maximum H<sub>2</sub> capacity after synthesis of the as-prepared material was 1.81 wt% and 1.56 wt% after activation. However, the equilibrium pressure of H<sub>2</sub> desorption is too low to desorb, causing the formation of the C14 hydride phase after the PCT test. With regard to the TiZrNbMoV HEA, the maximum H<sub>2</sub> capacity of the alloy after synthesis is 2.3 wt% and it is 1.78 wt% after annealing. This finding indicates that titanium and niobium, including these phases, absorb H<sub>2</sub>.

Besides increasing the capacity of hydrogen storage, it is also significant to understand the change in the microstructure in

the process of hydrogen storage. For example, Sahlberg *et al.*<sup>114</sup> prepared the TiVZrNbHf HEA and found that it can absorb a large amount of H<sub>2</sub> and the maximum H/M ratio is 2.5, which is similar to that of rare-earth alloys. The formation of FCC or BCT structures with fully hydrogenated alloys is similar to that for rare-earth compounds. The results show that the ultrahigh H<sub>2</sub> storage capacity is the strain effect in the deformed HEA lattice, which is conducive to H<sub>2</sub> occupying both tetrahedral and octahedral sites. Due to the high mass of Hf and Zr, the H<sub>2</sub> storage capacity is just about 2.7 wt%. Therefore, a higher storage capacity can be realized by replacing Zr and Hf. Karlsson *et al.*<sup>115</sup> synthesized HfNbTiVzr by heating in a furnace and subsequent ball milling. The *in situ* SR-PXD of the H<sub>2</sub> cycling experiments show that the BCC phase can be transformed into the body-centered tetrahedral hydride phase, and the H/M ratio is at least 2.5. The hydrogen atoms occupy both tetrahedral and octahedral interstitial sites in the structure, and the large lattice strain facilitates absorption at both octahedral and tetrahedral sites. Zlatea *et al.*<sup>116</sup> discovered that the TiZrNbHfTa HEA with the BCC phase experiences a two-step phase transition to an FCC dihydride phase and an intermediate tetragonal monohydride, as proven by the *in situ* SR-XRD result (Fig. 12).

Activation is another significant item for H<sub>2</sub> absorption. Zhang *et al.*<sup>117</sup> proposed that the H<sub>2</sub> absorption temperature of TiZrNbTa is markedly decreased from 715 K to room temperature, and the H<sub>2</sub> absorption kinetics are dramatically enhanced after activation. Meanwhile, a two-step activation mechanism has been proposed, namely, the surface oxide is reduced to the suboxide and it is further converted to sub-hydroxides. After activation, the size and concentration of the vacancy clusters significantly increase, which is the reason for improvement in the H<sub>2</sub> absorption kinetics. They also found that the maximum H<sub>2</sub> absorption of TiZrNbTa decreases from 1.67 to 1.25 wt% with an increase in the temperature from 293 to 493 K.<sup>118</sup> This

HEA also exhibits rapid H<sub>2</sub> absorption kinetics at room temperature and a shorter incubation time. In addition, the H<sub>2</sub> absorption capacity slowly decreases with the number of cycles, retaining 86% capacity after 10 cycles. Since the first application of HEAs in hydrogen storage, there have been many examples with great performance to expand their utilizations, such as LaNiFeVMn,<sup>119</sup> MgZrTiFe<sub>0.5</sub>Co<sub>0.5</sub>Ni<sub>0.5</sub>,<sup>120</sup> TiZrHfScMo,<sup>121</sup> TiVzr-NbTa<sub>1-z</sub>,<sup>122</sup> MgTiVCrFe,<sup>123</sup> and TiZrCrMnFeNi.<sup>124</sup>

Apart from chemical hydrogen storage, electrochemical hydrogen storage is also significant and could be used in metal-hydrogen batteries. For example, Zhang *et al.*<sup>125</sup> prepared the AB<sub>2</sub>-type alloys La<sub>0.8-x</sub>Ce<sub>0.2</sub>Y<sub>x</sub>MgNi<sub>3.4</sub>Co<sub>0.4</sub>Al<sub>0.1</sub> ( $x = 0, 0.05, 0.10, 0.15, 0.20$ ) via the melt spinning technology. The change in spinning speed and the content of Y element obviously changes the phase content, but does not change the phase composition. After electrochemical tests, these alloys exhibit good activation ability and reach the maximum discharge capacity in the first cycle. The discharge capacity initially increases and then decreases with an increase in the spinning speed. With an increase in the Y content, the cycling stability exhibits significant improvement, but the discharge capacity decreases. In addition, with an increase in the Y content and spinning rate, the electrochemical kinetics including the charge transfer rate, limiting current density, hydrogen diffusion coefficient, and high-rate discharge capacity initially increase and then decrease. This work expands the range of hydrogen storage materials used in traditional Ni-MH batteries.

Apart from H<sub>2</sub> storage, H<sub>2</sub> sensing is also important for practical applications involving H<sub>2</sub> gas considering the dangers of H<sub>2</sub> leakage. In order to ensure the safety of hydrogen storage and use, hydrogen-sensitive materials are needed to have the characteristics of high sensitivity, fast response, long recovery time, good stability, and recyclability.<sup>126</sup> Sharma *et al.*<sup>127</sup> designed an HEA by adding Pd and explored the possibility of

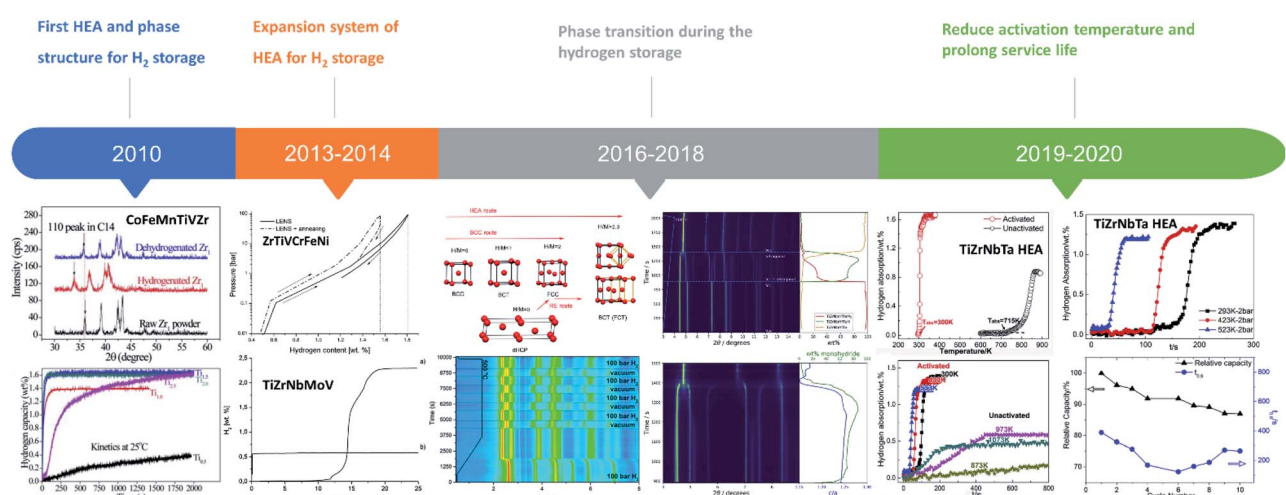


Fig. 12 Progress and development of HEA-related materials as hydrogen storage materials since 2010. Reproduced with the permission from ref. 112. Copyright © 2010, Elsevier Ltd. Reproduced with the permission from ref. 40. Copyright © 2013, Elsevier Ltd. Reproduced with the permission from ref. 113. Copyright © 2014, Elsevier Ltd. Reproduced with the permission from ref. 114. Copyright © 2016, Springer Nature. Reproduced with the permission from ref. 115. Copyright © 2018 American Chemical Society. Reproduced with the permission from ref. 117. Copyright © 2018, Elsevier Ltd. Reproduced with the permission from ref. 118. Copyright © 2019, Elsevier Ltd.

the new alloy for H<sub>2</sub> sensing. Similar to binary alloys, the diffusion of H atoms in Pd-rich HEA is usually achieved through octahedral cavities rather than tetrahedrons. Transition metals are the preferred elements for Pd-based alloys. Because the removal and addition of electrons take place on Pd atoms, the number of vacancies of Pd can be adjusted by the deformation of the Pd electronic structure. Theoretical calculations further verify that the upper and lower limits of the octahedral pore size are consistent in the range of Pd–M alloys. These HEAs open a new field for high-performance H<sub>2</sub>-sensitive materials in the future.

#### 4.3 Energy storage

Electrochemical supercapacitors are considered to be one of the most promising energy storage devices due to their advantages of fast energy transfer, long lifespan, and ultrahigh power density.

In particular, it can store more electrical energy by faradaic redox on the surface of the metal oxide, such as NiO, Co<sub>3</sub>O<sub>4</sub>,<sup>128</sup> and Fe<sub>2</sub>O<sub>3</sub>,<sup>129</sup> than the traditional double-layer capacitance mechanism. The unique electrochemical property of HEAs endows it to become a new type of electrochemical material; however, the evaluation of their electrochemical storage properties is still rare. Multicomponent oxides show better electrochemical activity and higher electronic conductivity, which are at least two orders of magnitude higher than those of single oxides.<sup>130</sup> Therefore, multicomponent nanoporous HEAs are taken as one of the candidates of supercapacitor materials. For example, Kong *et al.*<sup>131</sup> fabricated nanoporous metal core/oxide shell structure by the selective phase dissolution of AlCoCrFeNi HEA and enquired its electrochemical property (Fig. 13a). By selectively dissolving the Al–Ni-rich phase and retaining the remaining Cr–Fe-rich phase, the nanoporous structure could be obtained, which exhibited high capacitance (700 F cm<sup>-3</sup>) and impressive durability (3000 cycles) when used as a binder-free electrode. With the refinement of the as-prepared microstructure, the nanoporous structure afforded better performance.

Metal oxides are uniformly deposited on aligned carbon nanofibers (ACNFs) *via* electrodeposition for energy storage applications.<sup>132</sup> ACNFs afford favorable conditions for the formation of uniform films, and the thickness of the oxides can be adjusted by controlling the deposition current and time.<sup>133</sup> Xu *et al.*<sup>69</sup> reported the FeNiCoMnMg (30 nm) and FeNiCoCuMn (50 nm) HEA NPs through the uniform CTS approach (Fig. 13f). ACNFs possess a higher electron transport efficiency and play an important role in the formation of NPs. In terms of the capacitor performance (Fig. 13g), the electrodes synthesized by a 5 mM precursor display high capacitance (203 F g<sup>-1</sup>) and improved specific energy density (21.7 W h kg<sup>-1</sup>). These discoveries suggest that the HEA NPs/carbonaceous components are potential candidates for energy storage.

#### 4.4 Electromagnetic (EM) wave absorption

With the rapid development in new wireless communication technology, a large number of electronic devices have been applied in the gigahertz frequency range, and the ensuing EM

interference and pollution are also increasing.<sup>134</sup> It is important to develop EM-absorbing materials for the gigahertz frequency band.<sup>135</sup> EM interference shielding effect includes two mechanisms, that is, reflection and absorption. In order to obtain good reflection effect, the materials must have movable carriers (electrons or holes) to effectively interact with the incident EM field. Therefore, metals and alloys are widely used to shield EM radiation because of their high conductivity.<sup>136</sup> Absorption requires that electric or magnetic dipoles interact with the EM vectors of the incident radiation. Electric or magnetic dipoles usually exist in materials with high dielectric and magnetic constants. Therefore, magnetic metals (iron, cobalt, nickel, and so on) have huge practicability. In contrast to metals, ferromagnetic alloys with high saturation magnetization have better gigahertz permeability due to their higher Snoek's limitation frequency.<sup>137</sup> Similar to the famous FeSiAl with great performance, HEAs usually have relatively high  $\epsilon$  mismatching to the  $\mu$ , which weakens their absorption ability.

The reflection loss (RL) value is a significant parameter to evaluate these materials, and it can be calculated by using the following equations:<sup>138</sup>

$$RL = 20 \log |R| = 20 \log \left| \frac{Z_{in} - Z_0}{Z_{in} + Z_0} \right| \quad (16)$$

$$Z_{in} = Z_0 \left( \frac{\mu_r}{\epsilon_r} \right)^{\frac{1}{2}} \tanh \left\{ j \left( \frac{2\pi f d}{c} \right) (\mu_r \epsilon_r)^{\frac{1}{2}} \right\} \quad (17)$$

where  $Z_{in}$  and  $Z_0$  are the input impedance of the absorber and air, respectively;  $f$  is the frequency;  $d$  is the thickness of the material; and  $c$  is the velocity of light. The higher the absolute value of RL, the better is the performance of the absorber.

Microwave attenuation ( $\alpha$ ) is another factor for materials. The  $\alpha$  value is calculated by using the following equation:<sup>139</sup>

$$\alpha = \frac{\sqrt{2}\pi f}{c} \sqrt{(\mu''\epsilon'' - \mu'\epsilon') + \sqrt{(\mu''\epsilon'' - \mu'\epsilon')^2 + (\mu'\epsilon'' + \mu''\epsilon')^2}} \quad (18)$$

Yang *et al.*<sup>140</sup> (2016) were the first to prepare FeCoNiCrAl powders with a flaky shape by ball milling for 70 h. In the range of 2–18 GHz, the EM-wave absorption characteristics of the powder (70 wt%) dispersed in a paraffin matrix were studied. The  $RL_{min}$  reaches −35.3 dB at 10.35 GHz and an effective absorption bandwidth is 2.7 GHz (9.2–11.9 GHz), as shown in Fig. 14a and b. Due to its unique morphology and crystal structure, it has excellent microwave-absorbing properties in the intermediate- and high-frequency ranges. In order to study the influence of the crystalline structure on the performance, they also investigated FeCoNiCrAl<sub>0.8</sub> HEA and amorphous alloy *via* ball milling for 10 and 20 h, respectively.<sup>141</sup> The  $RL_{min}$  of FeCoNiCrAl<sub>0.8</sub> HEA is −41.8 dB at 11.9 GHz and the effective bandwidth (RL ≤ −10 dB) is up to 4.7 GHz, which are better than those of amorphous alloys.

It is well known that the size and shape of the material can influence its performance. Therefore, Zhang *et al.*<sup>142</sup> synthesized AlCoCrFeNi powders by the ball-milling method. In addition,

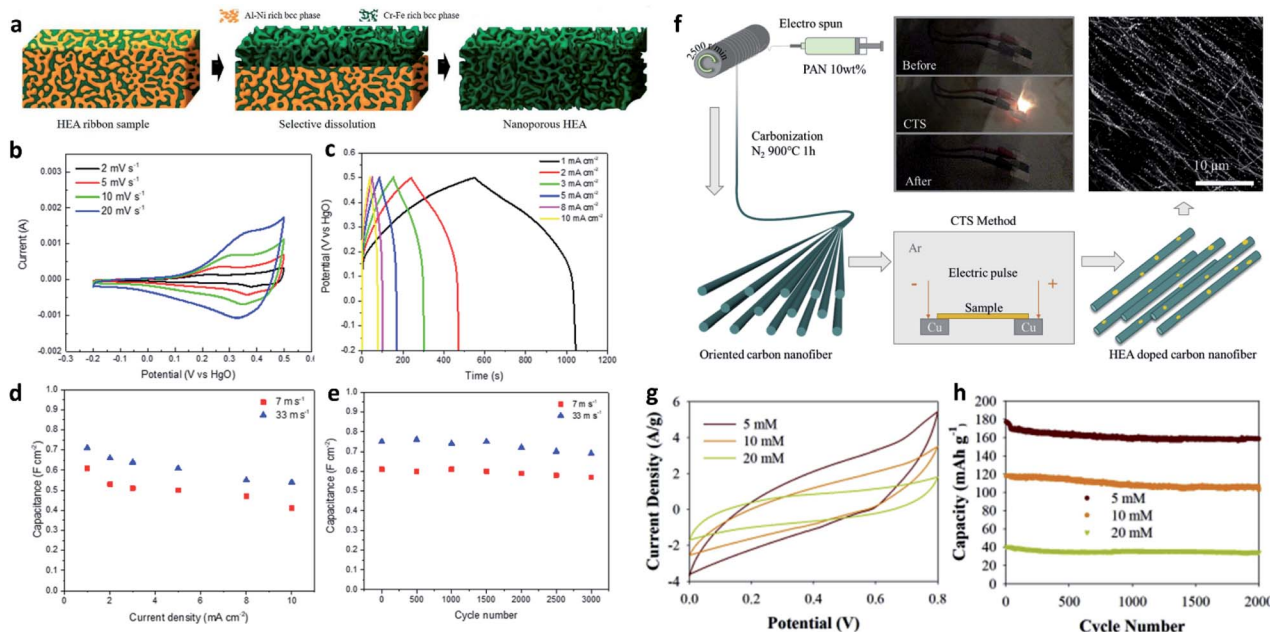


**Fig. 13** (a) Schematic of the phase-separated HEA dissolution process. The electrochemical performance of nanoporous HEA NPs, including cyclic voltammetry curves (b), galvanostatic charge–discharge curves (c), area-specific capacitance as a function of the current density (d), and area-specific capacitance as a function of number of cycles (e). Reproduced with the permission from ref. 131. Copyright © 2019, Elsevier Ltd. (f) Synthesis of HEA NPs/ACNFs. Electrochemical characterization of FeNiCoMnMg, including cyclic voltammetry (g) and durability (h). Reproduced with the permission from ref. 69. Copyright © 2020, Elsevier Ltd.

wet milling can downsize the powder and optimize the shape for EMI applications. The obtained results show that small HEAs embody good microwave-shielding performance in the frequency range of 26.5–40 GHz due to its small size and flaky shape compared with large HEAs (Fig. 14c and d). The maximum total shielding of the small HEA sample is 20 dB, while that of the large HEA sample is 8.44 dB, which is mainly increased from 6.8 dB of the large sample to 18 dB of the small sample by absorption. Therefore, the small-size HEA synthesized by wet milling is an attractive microwave-shielding material. Zhang *et al.*<sup>143</sup> also prepared FeCoNiSi<sub>0.4</sub>Al<sub>0.4</sub> by a mechanical-milling (M-HEA) and melting-strip casting-milling (C-HEA) method. The powders prepared by the C-HEA method exhibited smaller magneto-crystallinity, lower stress anisotropy, and larger shape anisotropy than that prepared by the M-HEA method (Fig. 14e). The EM parameters of the C-HEA powder are obviously larger than those of the M-HEA powder, and the conduction loss was mainly observed in the high-frequency range. By melting, strip casting, and milling to adjust the crystallinity of the materials, a series of FeCoNiSi<sub>x</sub>-Al<sub>0.4</sub> were further prepared.<sup>144</sup>

As-prepared alloys are always full of defects, and annealing as the conventional treatment in alloying may influence their properties in relation to microwave absorption. Duan *et al.*<sup>145</sup> fabricated FeCoNiCuAl HEA powders by mechanical alloying. The main absorption characteristics are due to the polarization and resonance caused by the large-aspect-ratio flake particles and high saturation magnetization. The optimum RL of 30 h-milled sample with a thickness of 2 mm is 19.17 dB. The

performances are improved after annealing, including the magnetic properties, EM parameters, and absorption properties (Fig. 14f). Duan *et al.*<sup>47</sup> also prepared flake-shaped FeCoNiAlCr<sub>x</sub> ( $x = 0.1, 0.3, 0.5, 0.7$ , and  $0.9$ ) powders using the same method and then they were annealed at 500 °C. With the addition of Cr, the particles become flatter and the number of polarization sites increase, which improve the surface polarization and the real and imaginary parts of complex permittivity. Meanwhile, with an increase in the Cr ratio, the RL<sub>min</sub> moves to the low-frequency region (8.23–11.20 GHz). When the sample was annealed, the enhanced saturation magnetization ( $M_s$ ) increases  $\mu_r$ , and the improvement in crystallinity also increases  $\epsilon_r$ . For the FeCoNiAlCr<sub>0.9</sub> sample, RL<sub>min</sub> directly increases from –26.88 dB (8.23 GHz) to –47.55 dB (7.375 GHz) after annealing, indicating that this treatment has a positive effect on the reflection loss (Fig. 14g).

Other FeCoNi-based HEAs are also developed using other synthesis methods. For example, FeCoNiCuZn was synthesized using high-frequency EM-field-assisted ball milling.<sup>146</sup> Its RL<sub>min</sub> reaches 14.69 dB at 10.96 GHz, corresponding to a thickness of 1.5 mm and effective bandwidth below 10 dB of 2.5 GHz. FeCoNi(Si<sub>0.6</sub>Al<sub>0.2</sub>B<sub>0.2</sub>) HEA was prepared by melt spinning and ball milling.<sup>147</sup> The composites with thicknesses of 1.2–2.0 mm have RL<sub>min</sub> of –38.1 to –44.1 dB with an effective bandwidth (RL < 10 dB) of 1.3 GHz, as shown in Fig. 14h. Lan *et al.*<sup>148</sup> transformed the spherical HEAs (Fe-Co-Ni-Cr-Cu-Al) into a porous hollow structure by using strong oxidizing nitric acid and divalent copper ion etching, which greatly improve the EM-wave absorption ability of the HEAs by improving their

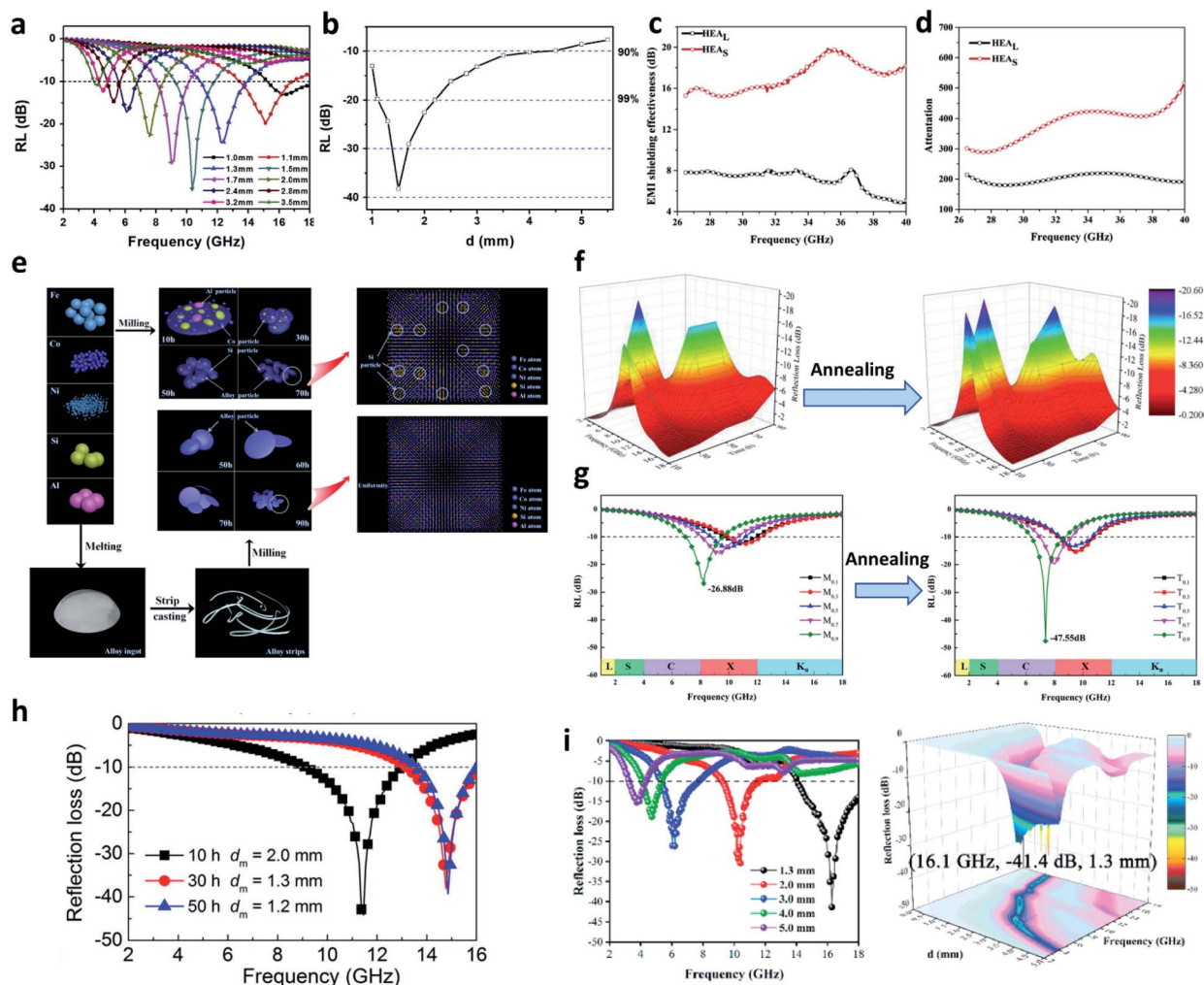


**Fig. 14** (a) RL curves and (b)  $RL_{\min}$  for FeCoNiCrAl at different thicknesses. Reproduced with the permission from ref. 140. Copyright © 2016, Elsevier Ltd. (c) EMI SET of HEA<sub>L</sub>/epoxy composite and HEA<sub>S</sub>/epoxy composite. (d)  $\alpha$  values of HEA<sub>L</sub>/epoxy and HEA<sub>S</sub>/epoxy composites. Reproduced with the permission from ref. 142. Copyright © 2018, Elsevier Ltd. (e) Flow chart of HEA powders formed by two methods and their aspect ratio and uniformity change. Reproduced with the permission from ref. 143. Copyright © 2018, Elsevier Ltd. (f) The RL of the FeCoNiCuAl HEA powders. The RL increased after annealing. Reproduced with the permission from ref. 145. Copyright © 2019, Elsevier Ltd. (g) RL curves for FeCoNiAlCr<sub>x</sub> HEA. The annealing treatment has a positive effect on  $RL_{\min}$ . Reproduced with the permission from ref. 47. Copyright © 2020, Elsevier Ltd. (h) Frequency dependence of RL at the different thicknesses of FeCoNi(Si<sub>0.6</sub>Al<sub>0.2</sub>B<sub>0.2</sub>) HEA. Reproduced with the permission from ref. 147. Copyright © 2019, AIP Publishing. (i) Frequency dependence of RL at different thicknesses of HEA@air@Ni-NiO microspheres. Reproduced with the permission from ref. 149. Copyright © 2019, Elsevier Ltd.

impedance matching. The effective absorption bandwidth of porous HEAs can reach 4.48 GHz with a thickness of 1.7 mm and  $RL_{\min}$  can reach  $-40.2$  dB (Table 2).

Apart from many kinds of HEAs used as a microwave absorber, HEA-based composites might be the next high-performance EM-wave absorbers. For example, Wu *et al.*<sup>149</sup> constructed core-shell microspheres with FeCoNiCrCuAl<sub>0.3</sub> as the core and Ni-NiO as the shell *via* a two-step hydrothermal method. The effective absorption bandwidth of the composites was 4 GHz with an ultrathin thickness (1.3 mm), as shown in Fig. 14i. The exterior nanosheets immensely enhanced the impedance matching of the materials and facilitated the incident EM waves to enter the interior of the materials. Besides, the magnetic loss caused by the internal core and the dielectric

loss caused by the external shell boost the EM energy dissipation by synergistic effects. A reasonable strategy makes the combination of two independent components, which have almost no independent EM-wave absorption performance, afford amazing EM-wave absorption capacity.

#### 4.5 TE materials

Waste heat recovery technology is a vital supplement to renewable energy in the future.<sup>150</sup> Over the past 20 years, new interest in efficient waste heat recovery for TE materials has led to the development of nanostructured materials. TE materials, as a type of material that can directly convert heat into electricity, have attracted the attention of countries all over the world in terms of waste heat recovery from engine exhaust to

Table 2 EM-wave absorption performance in recently published works

Samples	$RL_{min}$ (dB)	$f_E$ (GHz)	Thickness (mm)	Percentage (wt%)	Ref.
FeCoNiCrAl	35.3	2.7	1.5	70	140
FeCoNiCrAl <sub>0.8</sub>	41.8	4.7	2.3	70	141
FeCoNiCuAl	19.7	2.5	2.0	60	145
Annealed FeCoNiAlCr <sub>x</sub>	47.55	—	2.5	—	47
HEA@air@Ni-NiO	41.4	4.0	1.3	50	149
Porous Fe-Co-Ni-Cr-Cu-Al	40.2	4.48	1.7	—	148
FeCoNiCuZn	14.69	2.5	1.5	—	146
FeCoNi(Si <sub>0.6</sub> Al <sub>0.2</sub> B <sub>0.2</sub> )	44.1	3.8	2.0	60	147

improve fuel efficiency.<sup>151</sup> The Seebeck coefficient can be calculated by the following equation:

$$S = \frac{8\pi^2 k_B^2}{3eh^2} m^* \left( \frac{\pi \mu e}{3\sigma} \right)^2 \quad (19)$$

where  $n$  is the carrier concentration (mobility can be calculated as  $\mu = \sigma/en$ ) and  $m^*$  is the density-of-states effective mass of the carrier.<sup>152</sup>

In order to investigate the high-performance TE materials, the figure-of-merit  $zT$  value is used to measure the property. It can be expressed using the below equation:

$$zT = \frac{S^2 \sigma}{\kappa_{tot}} T \quad (20)$$

where  $\sigma$  is the electrical conductivity,  $T$  is the temperature in Kelvin, and  $\kappa_{tot}$  is the total thermal conductivity. It is the most popular strategy to obtain the best  $zT$  value by maximizing the power factor ( $PF = S^2 \sigma$ ) and minimizing  $\kappa_{tot}$ . For this reason, new methods related to low-dimensional materials and nanostructures for separation and independent parameter change have greatly improved the  $zT$  values of the most advanced TE materials.

High-performance TE materials must contain low-cost, low-toxic elements in order to achieve industrialization and global applications. However, at intermediate and low temperatures up to 600 °C, most high-performance TE materials ( $Bi_2Te_3$ ,  $PbTe$ , and  $(Bi_{1-x}Sb_x)_2(Se_{1-y}Te_y)_3$ ) include toxic or rare elements based on p-block elements; therefore, recent focus has shifted to the use of new structural types (half-Heusler alloys<sup>153</sup>) to meet this precondition. Moreover, the above materials based on p-block elements rapidly degrade at a temperature over 800 °C; therefore, attention has been focused on materials with higher thermal stability.

It has been found that at  $T = 505$  °C and  $x = 2.0$  and 2.25, the composition reaches  $zT = 0.015$ , which is the upper limit of thermal conductivity. Although many effective TE materials are valid at lower temperatures, few are effective at higher temperatures. Shafeie *et al.*<sup>154</sup> investigated the TE properties of the  $Al_xCoCrFeNi$  system ( $0.0 \leq x \leq 3.0$ ) in the range of 100–900 °C (Fig. 15a). The addition of elemental Al can increase the Seebeck coefficient ( $1 \mu V K^{-1}$  for  $x = 0.0$  to  $23 \mu V K^{-1}$  for  $x = 3.0$ ) and decrease the electrical conductivity ( $0.85 \text{ MS m}^{-1}$  for  $x = 0.0$  to  $0.36 \text{ MS m}^{-1}$  for  $x = 3.0$ ) at the same time. Moreover, the compositions reach a  $zT$  value of 0.015 for  $x = 2.0$  at

a temperature of 505 °C, reaching the upper limit of the measuring instruments. By changing the VEC of the system with appropriate replacement elements, the TE properties can be significantly tuned. With a decrease in VEC, the electrical and thermal transport properties of the system simultaneously decrease. In general, the high structural complexity and low average VEC can be used to reduce the total thermal conductivity and lattice thermal conductivity. This relationship of TE performance and VEC were confirmed by the work of Kush *et al.*<sup>155</sup> The TE properties of  $Ni_2CuCrFeAl_x$  HEA can be significantly controlled by changing the VEC with suitable replacement elements (Fig. 15b). The relationship between the electrical and thermal properties and the VEC is the same as the above work. Based on the transition metal material, Dong *et al.*<sup>156</sup> presented rare-earth-metal-doped  $Y_xCoCrFeNi$  and  $Gd_xCoCrFeNiCu$  as the TE materials (Fig. 15c). The thermal conductivity was reduced by controlling the phonon scattering because of the complexity of the HEAs. Here, Y/Gd-doped HEAs are promising TE materials. In addition, the  $Al_{0.3}CoCrFeNi$  HEA can achieve a  $zT$  value of 0.008.

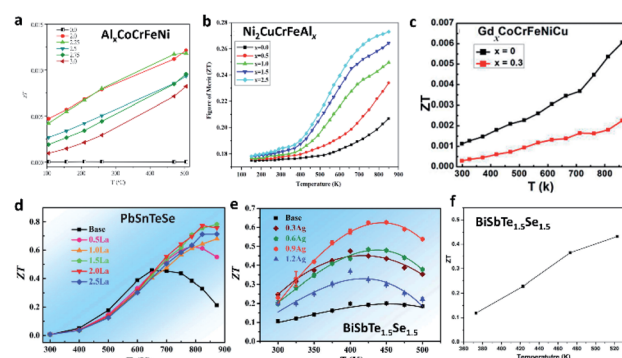


Fig. 15 (a) TE figure-of-merit  $zT$  for the  $Al_xCoCrFeNi$  samples. Reproduced with the permission from ref. 154. Copyright © 2015, AIP Publishing. (b) Temperature dependence of  $zT$  of  $Ni_2CuCrFeAl_x$  alloy. Reproduced with the permission from ref. 155. Copyright © 2020, IOP Publishing Ltd. (c)  $zT$  values of  $Gd_xCoCrFeNiCu$  alloy. Reproduced with the permission from ref. 156. Copyright © 2018, MDPI. (d) Figure-of-merit  $zT$  for the samples of  $PbSnTeSeLa_x$ . Reproduced with the permission from ref. 157. Copyright © 2016, Taylor and Francis Online.  $zT$  values of  $BiSbTe_{1.5}Se_{1.5}Ag_x$  (e) and  $BiSbTe_{1.5}Se_{1.5}$  (f). Reproduced with the permission from ref. 158. Copyright © 2016, Royal Society of Chemistry.

Additionally, many main group elements, such as IVA and VA elements, are also commonly used as TE materials. For example, Fan *et al.*<sup>157</sup> prepared polycrystalline PbSnTeSe HEA using melting and subsequent SPS with the substitution of Pb by La (Fig. 15d). The PbSnTeSe HEA exhibits low lattice thermal conductivity at a low temperature (less than  $0.6 \text{ W m}^{-1} \text{ K}^{-1}$  at 300 K). Small component changes not only increase the Seebeck coefficient and conductivity, but also partly decrease the bipolar thermal conductivity, leading to enhancement in the  $zT$  value. When doped with 1.5% La, the  $zT$  value is about 0.8 at 873 K. The addition of a small amount of La not only improves the Seebeck coefficient and high-temperature electrical conductivity, but also suppresses the bipolar effect to a certain extent. Therefore, reducing the lattice thermal conductivity is one of the most effective ways to improve the properties of TE materials. Fan *et al.*<sup>158</sup> prepared polycrystalline BiSbTe<sub>1.5</sub>Se<sub>1.5</sub> HEA with different amounts of Ag by melting and SPS treatment (Fig. 15e). The dependence of conductivity and thermal conductivity on temperature is very weak, which may be due to the high entropy effect of HEAs. The results suggest that the lattice thermal conductivity of this HEA is very low ( $0.47 \text{ W m}^{-1} \text{ K}^{-1}$  at 400 K), which can be attributed to the presence of serious lattice distortion. Moreover, the addition of trace Ag can increase the Seebeck coefficient and further reduce the lattice thermal conductivity. Therefore, the maximum  $zT$  value is 0.63 at 450 K after adding 0.9 at% Ag. Karati *et al.*<sup>159</sup> synthesized Ti<sub>2</sub>NiCoSnSb with a half-Heusler structure by arc melting and ball milling. The half-Heusler phase was formed in the form of nanocrystals when ball milling was conducted for 5 h. Compared with a nanocrystalline alloy ( $zT$  of 0.047 at 860 K), the  $zT$  value of a microcrystalline alloy is 0.144 at 860 K. Inspired by the above work of Ti<sub>2</sub>NiCoSnSb HEA with a VEC of 18, they<sup>160</sup> extended this concept by substituting Sn atoms by Sb atoms in Ti<sub>2</sub>NiCoSn<sub>1-x</sub>Sb<sub>1+x</sub> ( $x = 0.5, 1$ ) to increase the VEC from 18 to 18.5. Ti<sub>2</sub>NiCoSn<sub>1-x</sub>Sb<sub>1+x</sub> was synthesized by vacuum arc melting, ball milling, and SPS. The alloy with  $x = 0.5$  exhibits a low lattice thermal conductivity of  $2.48 \text{ W m}^{-1} \text{ K}^{-1}$  and improved  $zT$  of 0.29 at 873 K. Therefore, this work opens the road for exploring HEAs with a VEC >18 for TE applications. Raphael *et al.*<sup>161</sup> synthesized the BiSbTe<sub>1.5</sub>Se<sub>1.5</sub> HEA by mechanical metallurgy and SPS. High-entropy engineering and nanostructure phenomena reduce the lattice thermal conductivity ( $<0.2 \text{ W mK}^{-1}$ ) and thermal diffusivity ( $<0.5 \text{ mm}^2 \text{ s}^{-1}$ ) in a collaborative manner, leading to an ultralow thermal conductivity ( $0.667 \text{ W mK}^{-1}$  at 523 K). The HEA has a good power factor ( $5.51 \times 10^{-4} \text{ W mK}^{-2}$ ) and an excellent  $zT$  value of 0.43 at 523 K.

#### 4.6 Radiation protection

Nuclear energy is the third largest energy source in the world after thermal power and hydropower because of its high thermal efficiency, cleanliness, and reliability. This indicates that it will become necessary to use structural materials in harsh environments with high temperature and high radiation dose (up to dozens of displacements per atom (dpa)).<sup>162,163</sup> Therefore, the challenge of structural materials becomes considerable,

particularly the requirement to resist radiation damage. High-dose neutron irradiation can lead to vacancy, dislocation, and solute precipitation, as well as hydrogen and helium transmutation gas damage, which can result in expansion, cavity, material embrittlement, hardening, and failure.<sup>164,165</sup> Traditional materials for nuclear reactors, including various martensitic or austenitic steels, nickel-based superalloys, and zirconium alloys, can only withstand up to 10 dpa irradiation and cannot withstand harsh environments. They can easily cause horrible H<sub>2</sub> explosions, such as the one that occurred in Fukushima.<sup>166</sup> In recent years, HEAs have attracted wide attention in the field of materials research due to their significant strength and toughness. In addition, they are particularly useful for high-dose irradiation applications because they claim to have self-healing capability,<sup>167</sup> which is caused by severe lattice distortion or atomic-level stress due to atomic-size mismatches between the major elements.

Xia *et al.*<sup>168</sup> studied the irradiation resistance performance of Al<sub>x</sub>CoCrFeNi ( $x = 0.1, 0.75$ , and  $1.5$ ) HEA under 3 MeV Au-ion irradiation (Fig. 16a). All the alloys exhibited excellent structural stability when irradiated by more than 50 dpa at 298 K. At the same irradiation dose, the radiation-induced volume expansion of Al<sub>x</sub>CoCrFeNi HEAs was significantly lower than that of traditional materials. Irradiation often leads to an increase in the defect content of the materials; therefore, it is very important to study the relationship between irradiation and defects. For example, Yang *et al.*<sup>169</sup> studied structural damage and chemical segregation in the Al<sub>0.1</sub>CoCrFeNi HEA at high temperatures. With an increase in the irradiation temperature, the defect density decreases but the defect size increases, which is caused by an increase in the defect mobility.

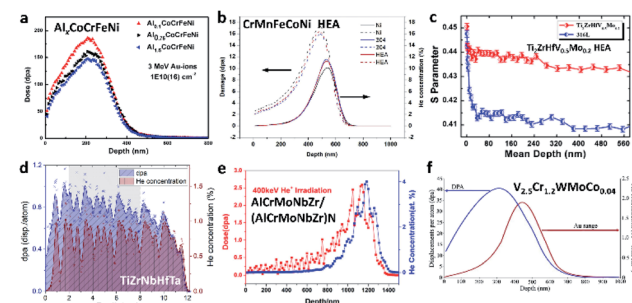


Fig. 16 (a) Irradiation-induced damage of Al<sub>x</sub>CoCrFeNi HEA under 3 MeV Au ions. Reproduced with the permission from ref. 168. Copyright © 2015, Springer Nature. (b) Stopping and Range of Ions in Matter (SRIM) simulation of He-ion irradiation damage indicates the radiation resistance of CrMnFeCoNi HEAs. Reproduced with the permission from ref. 171. Copyright © 2019, Elsevier Ltd. (c) SRIM-predicted damage profile from both full-cascade and quick option. Reproduced with the permission from ref. 172. Copyright © 2019, Elsevier Ltd. (d) Radiation-induced damage represented by the SRIM damage of TiZrNbHfTa. Reproduced with the permission from ref. 176. Copyright © 2019, Springer Nature. (e) SRIM calculation of damage and He concentration in AlCrMoNbZr/(AlCrMoNbZr)N. Reproduced with the permission from ref. 175. Copyright © 2019, Elsevier Ltd. (f) Damage profile calculated by the SRIM of V<sub>2.5</sub>Cr<sub>1.2</sub>WMoCo<sub>0.04</sub>. Reproduced with the permission from ref. 177. Copyright © 2020, Elsevier Ltd.

Results of the atomic probe tomography show that high-temperature ion irradiation can lead to enrichment of nickel and cobalt and depletion of iron and chromium in the defect clusters, mainly including dislocation loops and long dislocations. With an increase in the Al content in  $\text{Al}_x\text{CoCrFeNi}$  HEA, Pu *et al.*<sup>170</sup> synthesized ultrafine nanocrystalline  $\text{Al}_{1.5}\text{CoCrFeNi}$  HEA films by adjusting the radiofrequency magnetic sputtering rate at room temperature. The enhancement in helium-ion radiation tolerance for  $\text{Al}_{1.5}\text{CoCrFeNi}$  films has triggered significant research interest. No observable He bubbles were found in the damage region of the films, even though the He concentration was up to 8.50 at%. In addition, these HEA films exhibited higher swelling resistance than that of bulk coarse-grained HEAs because of the lower size of the He clusters. Therefore, these HEAs can be used as structural materials for advanced nuclear reactors in the future.

Yang *et al.*<sup>171</sup> revealed the He-ion irradiation resistance of CrMnFeCoNi HEA compared with pure Ni and 304 stainless steel (Fig. 16b). The CrMnFeCoNi HEA exhibits the smallest He bubble size, densest SFs/SFTs, and highest hardening, indicating that it has the best structural stability and best irradiation resistance. The reason for the above phenomenon is the smallest He atom and point defect mobility both at room temperature and at 450 °C. Lu *et al.*<sup>172</sup> reported novel BCC-type  $\text{Ti}_2\text{ZrHfV}_{0.5}\text{Mo}_{0.2}$  with outstanding irradiation resistance. The lattice constant of  $\text{Ti}_2\text{ZrHfV}_{0.5}\text{Mo}_{0.2}$  decreases after irradiation, which is contrary to traditional alloys. Positron annihilation experiments showed that the vacancy concentration of  $\text{Ti}_2\text{ZrHfV}_{0.5}\text{Mo}_{0.2}$  HEA was evidently higher than that of traditional alloys. The effect of these vacancies is similar to that of oxide dispersion-strengthened alloy, which endows HEAs with high radiation resistance. Atwani *et al.*<sup>173</sup> developed a BCC W-based HEA ( $\text{W}_{38}\text{Ta}_{36}\text{Cr}_{15}\text{V}_{11}$ ) with great radiation resistance. The dislocation loops were not observed even after 8 dpa. It is predicted that the formation of V-rich second-phase particles and the equal mobility of point defects are the root causes of the abnormal radiation tolerance.

Zhang *et al.*<sup>174</sup> investigated the growth and phase stability of  $\text{Ni}_{0.2}\text{Fe}_{0.2}\text{Co}_{0.2}\text{Cr}_{0.2}\text{Cu}_{0.2}$  HEA under thermally induced or irradiation-induced conditions (Fig. 16c). Under the irradiation of 3 MeV Ni ions up to extremely high 600 dpa, the FCC phase is stable and the average grain size increases from 15.6 to 25.2 nm. The high concentration of defects produced by radiation far exceed the defects of thermally induced conditions. Zhang *et al.*<sup>175</sup> studied the interfacial structure and mechanical properties of  $\text{AlCrMoNbZr}/(\text{AlCrMoNbZr})\text{N}$  coatings exposed under different doses of He irradiation (Fig. 16d). HEA with a thicker coating has good interfacial stability, better mechanical properties, and higher corrosion resistance. This work suggests the potential application of an HEA coating as nuclear fuel cladding.

Moschetti *et al.*<sup>176</sup> investigated the microstructure and mechanical properties of nanostructured  $\text{TiZrNbHfTa}$  after the irradiation of  $\text{He}^{2+}$  ions (Fig. 16e). The hardness of both recrystallized and nanocrystalline materials moderately increased after irradiation due to the radiation hardening caused by the formation of defects in the He lattice. Patel

*et al.*<sup>177</sup> fabricated  $\text{V}_{2.5}\text{Cr}_{1.2}\text{WMoCo}_{0.04}$  with the BCC structure by arc melting. Metastable as-cast  $\text{V}_{2.5}\text{Cr}_{1.2}\text{WMoCo}_{0.04}$  exhibits superior resistance to radiation-induced damage up to 40 dpa (Fig. 16f). The extraordinary phase stability is attributable to the combination of self-healing process and BCC structure.

#### 4.7 Magnetocaloric materials

Compared with the traditional refrigeration mode, magnetocaloric refrigeration provides a higher energy efficiency by 20% and has other advantages of environmental protection without using harmful ozone-damaging refrigerants.<sup>178</sup> In recent years, research has focused on room-temperature materials with high efficiency, low cost, and low dependence on rare-earth elements (REs) with large magnetocaloric response and working temperature.<sup>179</sup> However, the scarcity and high price of REs limit their commercial applications; therefore, researchers began to study more sustainable transition-metal-based alloys to reduce costs.<sup>180</sup> Based on the first-order and second-order magnetic-phase transitions, magnetocaloric materials can be divided into two categories. The first type is characterized by large- and narrow-peak magnetic entropy changes along with magnetic-structure phase transition. A large-peak entropy change is usually accompanied by an undesirable thermal lag,<sup>179,181</sup> and requires material grading of different  $T_c$ 's to span the corresponding thermodynamic cycle. The second type of material usually exhibits a low-peak entropy change, reduced hysteresis loss, and tunable  $T_c$ ,<sup>182</sup> but a wide peak value can lead to an enhancement in the refrigeration capacity (RC).<sup>183</sup> Although this kind of material is considered to be the best choice of magnetic refrigerant at present, alloys with large magnetic entropy change and RC are rarely developed and manufactured. It is paramount for the practical application of magnetic refrigerants to explore new alloys with large magnetic entropy changes and higher RC by innovative approaches, as shown in Fig. 17.

The magnetocaloric effect is measured by the temperature change in magnetic materials when they adiabatically enter or leave a magnetic field. In order to make the total entropy as zero, the thermal entropy of the system should be increased, which leads to a rise in the system temperature. On the contrary, when the magnetic field is removed, the change in thermal entropy can be quantified by indirectly measuring a change in magnetic entropy, which is calculated by

$$\Delta S_m = \int_0^{H_{max}} \left( \frac{\partial M}{\partial T} \right)_H dH \quad (21)$$

Using the above equation, the isothermal magnetization curve in a temperature range is integrated to reflect the change in magnetic entropy. A common figure of merit for evaluating magnetocaloric materials is the RC, which considers the temperature range and entropy change in a given material. RC can be measured by a variety of methods, but a common definition is that the peak entropy can be multiplied by the temperature span at the full-width at half-maximum (FWHM):

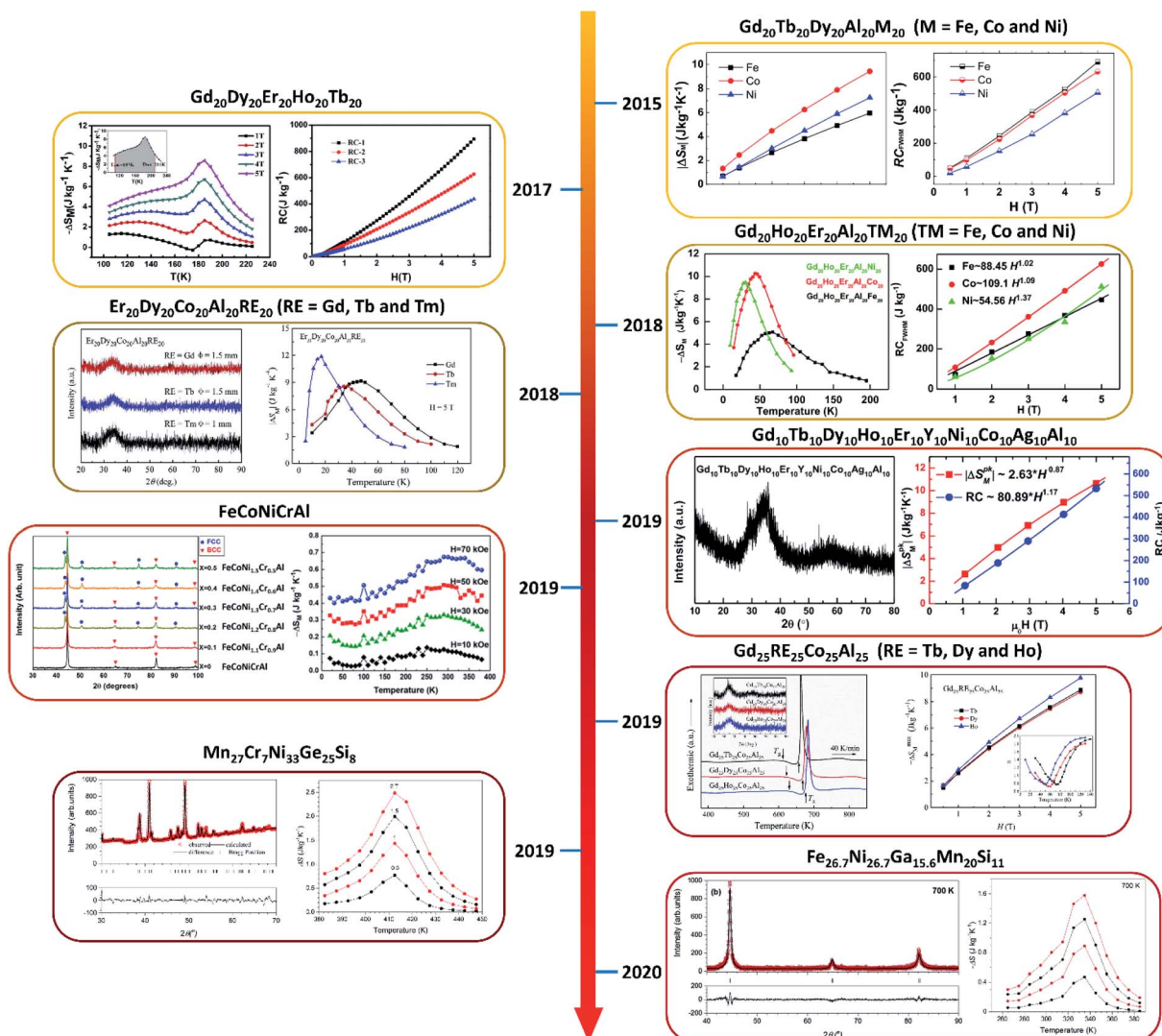


**Fig. 17** Time evolution of various TE materials in recent years. Reproduced with the permission from ref. 184. Copyright © 2014, Elsevier Ltd. Reproduced with the permission from ref. 186. Copyright © 2016, Elsevier Ltd. Reproduced with the permission from ref. 187. Copyright © 2018, Elsevier Ltd. Reproduced with the permission from ref. 188. Copyright © 2018, Elsevier Ltd. Reproduced with the permission from ref. 189. Copyright © 2018, Elsevier Ltd. Reproduced with the permission from ref. 190. Copyright © 2019, Elsevier Ltd. Reproduced with the permission from ref. 192. Copyright © 2019, AIP Publishing. Reproduced with the permission from ref. 101. Copyright © 2019, Elsevier Ltd.

$$RC_{\text{FWHM}} = |\Delta S_m \Delta T_{\text{FWHM}}| \quad (22)$$

As the electric field increases, the value of the peak entropy, corresponding RC scale, and temperature of the entropy peak also increase.

Rare-earth-metal-based materials are usually used as magnetocaloric materials. Therefore, the combination of multi-rare-earth-metal HEA is a promising direction in this field. For example, Huo *et al.*<sup>184</sup> reported the magnetocaloric properties of  $\text{Gd}_{20}\text{Tb}_{20}\text{Dy}_{20}\text{Al}_{20}\text{M}_{20}$  ( $\text{M} = \text{Fe}, \text{Co}$ , and  $\text{Ni}$ ) BMGs. Their  $|\Delta S_M^{\text{px}}$  under an applied field (5 T) are 5.96, 9.43, and 7.25  $\text{J kg}^{-1} \text{K}^{-1}$ , respectively, which are comparable to those of rare-earth-based materials. Interestingly, all the three HE BMGs have higher  $\delta T_{\text{FWHM}}$  (116 K for  $\text{M} = \text{Fe}$ ) and larger RC than their BMG counterparts. This may be due to the complex composition and spin recombination of these alloys. The research of

magnetocaloric materials mainly focuses on improving the refrigeration constant and controlling  $T_c$ . Kurniawan *et al.*<sup>185</sup> investigated the effect of metal additions on the exchange interaction distributions in equiatomic ferromagnetic alloys. The added metals include noble metals (*e.g.*, Cu, Ag), antiferromagnetic transition metals (*e.g.*, Mn), Stoner-enhanced transition metals (*e.g.*, Pt), and early transition metals (*e.g.*, Mo). Yuan *et al.*<sup>186</sup> investigated the quinary rare-earth-metal-based HEAs with large MCE (8.6  $\text{J kg}^{-1} \text{K}^{-1}$  at 5 T) and large RC (about 627  $\text{J kg}^{-1}$  at 5 T). The strong chemical disorder caused by the high configurational entropy enhances the difficulty of magnetic ordering, which leads to the slow magnetic-phase transition and enhancement in the magnetocaloric effect. Sheng *et al.*<sup>187</sup> fabricated  $\text{Gd}_{20}\text{Ho}_{20}\text{Er}_{20}\text{Al}_{20}\text{TM}_{20}$  ( $\text{TM} = \text{Fe}, \text{Co}$ , and  $\text{Ni}$ ) microwires by a melt-extraction method. The  $-\Delta S_{\text{max}}$  and RC under 5 T can reach 10.2  $\text{J kg}^{-1} \text{K}^{-1}$  and 625  $\text{J kg}^{-1}$ ,

respectively, which are significantly larger than those of most rare-earth-based MGs. Therefore, HE MG microwires are an ideal choice for magnetic refrigerants due to their suitable alloying with different transition elements. Li *et al.*<sup>188</sup> prepared Er<sub>20</sub>Dy<sub>20</sub>Co<sub>20</sub>Al<sub>20</sub>RE<sub>20</sub> (RE = Gd, Tb and Tm) HE BMGs with tunable magnetocaloric properties. The magnetic entropy changes ( $|\Delta S_M^{\max}|$ ) under 5 T were 9.1, 8.6, and 11.9 J kg<sup>-1</sup> K<sup>-1</sup>, respectively, affording RC<sub>max</sub> values of 619, 525, and 405 J kg<sup>-1</sup>, respectively. Huo *et al.*<sup>189</sup> reported the Gd<sub>10</sub>Tb<sub>10</sub>Dy<sub>10</sub>Ho<sub>10</sub>Er<sub>10</sub>Y<sub>10</sub>Ni<sub>10</sub>Co<sub>10</sub>Ag<sub>10</sub>Al<sub>10</sub> denary HE MG. The study of magnetocaloric effect shows that the denary HE MG has a large change in magnetic entropy in a wide temperature range; therefore, it has a large RC. Its  $|\Delta S_M^{\max}|$ ,  $\Delta T$ , and RC under 5 T are 10.64 J kg<sup>-1</sup> K<sup>-1</sup>, 6.66 K, and 532 J kg<sup>-1</sup>, respectively, which are comparable to those of rare-earth-based MGs. Combined with the alloy design of HEAs and the atomic-level homogeneous single-phase characteristics of MG, the magnetocaloric properties of HE MGs can be adjusted by changing the element or configurational entropy. Xue *et al.*<sup>190</sup> studied Gd<sub>25</sub>RE<sub>25</sub>Co<sub>25</sub>Al<sub>25</sub> (RE = Tb, Dy, and Ho) with different rare-earth substitutions. At the magnetic field of 5 T,  $-\Delta S_{\max}$  values for RE = Tb, Dy, and Ho are 8.88, 8.72, and 9.78 J kg<sup>-1</sup> K<sup>-1</sup>, respectively, and the corresponding RC values are 577, 567, and 626 J kg<sup>-1</sup>, respectively.

Apart from traditional RE-metal-based magnetocaloric materials, exploring alloys without expensive RE metals has been another focus, particularly considering the cost perspective. For example, Perrin *et al.*<sup>191</sup> explored the FeCoNiCuMn HEA, where small deviations from the equiatomic composition produced an interesting  $T_c$  of 300 K. The distributed exchange interactions ( $J_{ex}$ ) between the magnetic elements were proven by the Mössbauer spectroscopy measurements, which help to expand the magnetocaloric effect. Doping is the most commonly used strategy in alloy research. Na *et al.*<sup>192</sup> investigated the effects of substituting Ni/Al for Cr on the performances of FeCoNiCrAl-type HEAs. The annealed FeCoNi<sub>1.5</sub>Cr<sub>0.5</sub>Al alloy with the FCC phase shows a broad magnetic-phase transition at 150 K. This leads to a high RC<sub>FWHM</sub> of 242.6 J kg<sup>-1</sup> and  $-\Delta S_M$  value of 0.674 J kg<sup>-1</sup> K<sup>-1</sup> near room temperature at 70 kOe. These performances are comparable to those of Fe-based MGs and have similar transitions at room temperature. In addition, main group elements can also be employed in the HEA family. Sarlar *et al.* investigated Fe<sub>26.7</sub>Ni<sub>26.7</sub>Ga<sub>15.6</sub>Mn<sub>20</sub>Si<sub>11</sub> (ref. 101) and Mn<sub>27</sub>Cr<sub>7</sub>Ni<sub>33</sub>Ge<sub>25</sub>Si<sub>8</sub> (ref. 193) HEAs by arc melting and suction casting. The former HEA affords  $-\Delta S_M^{\max}$  of 1.59 J kg<sup>-1</sup> K<sup>-1</sup> (0–2 T) and RC of 75.68 J kg<sup>-1</sup> after the annealing process. The latter HEA yields  $-\Delta S_M^{\max}$  of 2.49 J kg<sup>-1</sup> K<sup>-1</sup>, among the highest reported values of alloys without RE elements. Even compared with HEAs with RE elements, these samples possess lower  $\Delta S_M$ , but their  $T_c$  values are close to room temperature.

#### 4.8 Superconducting materials

Superconductivity is a series of physical phenomena observed in some materials, which was discovered in 1911 by the Dutch physicist H. K. Onnes. The most significant difference between ordinary metal conductors and superconductors is that the

resistance of the latter gradually decreases with a decrease in the temperature, even close to absolute zero. Superconductors have a characteristic critical temperature ( $T_c$ ), below which the resistance suddenly drops to zero. Another characteristic is the Meissner effect, that is, when the superconductor changes into the superconductor state, the magnetic field lines are completely ejected from the interior of the superconductor. After more than a century of development, it is clear that superconductor systems with traditional metals and simple alloys have been basically studied. Since the twenty-first century, the newly developed HEAs have provided novel samples for the research of metal-based superconductors. It not only enriches the superconductor family with excellent properties, but also expands a new field for the theoretical development of superconductivity.

**4.8.1 BCC-type HEA superconductors.** Koželj *et al.*<sup>194</sup> were the first to synthesize Ta<sub>34</sub>Nb<sub>33</sub>Hf<sub>8</sub>Zr<sub>14</sub>Ti<sub>11</sub> with the BCC structure. The measurements revealed that this HEA is a type-II superconductor with a transition temperature  $T_c$  of 7.3 K, an upper critical field  $\mu_0 H_{C2}$  of 8.2 T, and a lower critical field  $\mu_0 H_{C1}$  of 32 mT. The investigated HEA is close to a BCS-type phonon-mediated superconductor in the weak electron-phonon coupling limit. Two years later, Jasiewicz *et al.*<sup>195</sup> applied the Korringa-Kohn-Rostoker method with the coherent potential approximation to formulate the first HEA superconductor. The result indicates comparatively strong electron-phonon coupling in Ta<sub>34</sub>Nb<sub>33</sub>Hf<sub>8</sub>Zr<sub>14</sub>Ti<sub>11</sub>. Rohr *et al.*<sup>196</sup> synthesized the [TaNb]<sub>1-x</sub>(ZrHfTi)<sub>x</sub> by arc melting and subsequent quenching. The superconducting transition temperatures of these HEAs (4.49–7.92 K) were found to be correlated with their VEC criteria, which can be categorized into simple solid solutions and amorphous materials. This work also investigates the influence of the complexity of HEAs on the superconductivity. Meanwhile, Vrtnik *et al.*<sup>197</sup> presented the superconductivity of Ta-Nb-Hf-Zr-Ti HEAs with different atomic concentrations. The  $T_c$  values fall between 5.0 and 7.3 K, which may be related to the structure and chemical inhomogeneity of the samples. Jasiewicz *et al.*<sup>198</sup> chose (TaNb)<sub>0.67</sub>(HfZrTi)<sub>0.33</sub> as an example and studied the influence of pressure on the electronic structure and superconductivity. The calculated  $T_c$  increases to 40–50 GPa, which subsequently stabilizes to a larger value than that under the ambient condition, which is consistent with the experimental results.

Doping as an efficient strategy used to enhance the performance of functional materials can also be applied to superconductors. For example, Rohr *et al.*<sup>199</sup> synthesized [TaNb]<sub>0.67</sub>(ZrHfTi)<sub>0.33</sub> substituted with isoelectronic mixtures of [Sc-Cr][Y-Mo], [Sc-Mo], and Al alloying. According to previous research, the  $T_c$  value strongly depends on the elemental composition of the alloy, not just its electron number. Therefore, substituting Nb or Ta with an isoelectronic mixture can reduce the  $T_c$  by more than 60%, while the effect of substituting hafnium, zirconium, or titanium with an isoelectronic mixture on the  $T_c$  is limited. The effect of Al alloying on the [TaNb]<sub>0.67</sub>(ZrHfTi)<sub>0.33</sub> HEA is further investigated. It is found that the dependence of  $T_c$  on the number of electrons for (HEA)

$\text{Al}_x$  is more crystalline-like than that of the  $[\text{TaNb}]_{1-x}(\text{ZrHfTi})_x$  solid solution.

Apart from the classical Ta–Nb–Hf–Zr–Ti homolog HEAs, other BCC-type HEA systems are further developed in recent years. For example, Marik *et al.*<sup>200</sup> prepared a single-phase polycrystalline  $\text{Nb}_{21}\text{Re}_{16}\text{Zr}_{20}\text{Hf}_{23}\text{Ti}_{20}$  HEA by arc melting. Various measurements have revealed that this HEA is a BCS-type phonon-mediated type-II superconductor with  $T_C = 5.3$  K,  $H_{C1}(0) = 33$  mT, and  $H_{C2}(0) = 8.88$  T. Yuan *et al.*<sup>201</sup> synthesized the BCC-structured  $\text{Ti}_{15}\text{Zr}_{15}\text{Nb}_{35}\text{Ta}_{35}$  HEA with  $T_C$  of  $\sim 8$  K. Ishizu *et al.*<sup>202</sup> found that BCC-type  $\text{Hf}_{21}\text{Nb}_{25}\text{Ti}_{15}\text{V}_{15}\text{Zr}_{24}$  HEA is a new superconductor with a  $T_C$  value of 5.3 K.

**4.8.2  $\alpha$ -Mn-type HEA superconductors.** Stolze *et al.*<sup>203</sup> described and characterized  $(\text{ZrNb})_{1-x}[\text{MoReRu}]_x$ ,  $(\text{HfTaWIr})_{1-x}[\text{Re}]_x$ , and  $(\text{HfTaWPt})_{1-x}[\text{Re}]_x$  systems with the BCC  $\alpha$ -Mn-type structures and mixed-site occupancies. The  $(\text{HfTaWIr})_{1-x}[\text{Re}]_x$  and  $(\text{HfTaWPt})_{1-x}[\text{Re}]_x$  systems are the first reported 5d-element-only HEA superconductors. All the three systems are type-II superconductors with strongly varying  $T_C$  depending on the cubic lattice parameter  $a$  and the VEC. The  $T_C$  values linearly increase with decreasing  $a$  and increasing VEC and fall between those of crystalline and amorphous alloy superconductors.

**4.8.3 CsCl-type HEA superconductors.** Stolze *et al.*<sup>215</sup> synthesized  $(\text{ScZrNb})_{1-x}[\text{RhPd}]_x$  and  $(\text{ScZrNbTa})_{1-x}[\text{RhPd}]_x$  HEAs by arc melting. Both HEAs are type-II superconductors with strongly varying  $T_C$  values depending on the VEC. The  $(\text{ScZrNb})_{0.65}[\text{RhPd}]_{0.35}$  HEA with the highest  $T_C$  (9.3 K) exhibits the largest  $\mu_0 H_{C2}(0)$  of 10.7 T. Pentanary and hexanary HEAs have higher  $T_C$  values than their binary intermetallic homologs. The presence of niobium, even up to 20 at%, has a positive influence on the  $T_C$ . However,  $(\text{ScZr})_{0.50}[\text{RhPd}]_{0.50}$  without the Nb element proves its intrinsic superconductivity (Fig. 18).

**4.8.4 HCP-type HEA superconductors.** Marik *et al.*<sup>204</sup> reported the synthesis of  $\text{Re}_{0.56}\text{Nb}_{0.11}\text{Ti}_{0.11}\text{Zr}_{0.11}\text{Hf}_{0.11}$ —the first hexagonal HEA superconductor fabricated by using the arc-melting technique. The results show that the HEA is a type-II superconductor with a  $T_C$  of 4.4 K,  $H_{C1}(0)$  of 2.3 mT, and  $H_{C2}(0)$  of 3.6 T. Liu *et al.*<sup>205</sup> reported the superconducting properties of new hexagonal  $\text{Nb}_{10+2x}\text{Mo}_{35-x}\text{Ru}_{35-x}\text{Rh}_{10}\text{Pd}_{10}$  ( $0 \leq x \leq 5$ ). With increasing  $x$ , the maximum  $T_C$  is 6.19 K at  $x = 2.5$ , while the  $H_{C2}(0)$  value increases monotonically, reaching 8.3 T at  $x = 5$ . Both these performances are the highest among hexagonal HEA superconductors. In addition, the results show that the  $T_C$  of these HEAs is not determined by the density of states at the Fermi level, but by reducing the VEC to increase  $T_C$ .

**4.8.5 f-Electron-containing HEA superconductors.** Nelson *et al.*<sup>206</sup> reported an f-electron-containing HEA, *i.e.*,  $[\text{TaNb}]_{0.31}(\text{TiUHf})_{0.69}$ , which is the first case to include an actinide ion. This HEA crystallizes in the BCC structure, which exhibits phonon-mediated superconductivity with a  $T_C$  value of 3.2 K and  $H_{C2}$  value of 6.4 T. These results extend the range of HEA superconductors containing actinides, indicating that superconductivity is stable in this subclass, which opens the way for the use of HEAs as functional wastes of various radioisotopes.

**4.8.6 Mixed-phase HEA superconductors.** The phase structure of HEAs not only influences their physical properties, but also has a close relationship with the performance of

superconductors. Apart from a single-phase HEA with superconductivity, many mixed-phase HEAs also represent unique performances. For example, Lee *et al.*<sup>207</sup> found that quaternary  $\text{Mo}_{0.25}\text{Re}_{0.25}\text{Ru}_{0.25}\text{Rh}_{0.25}$  (VEC of 7.5) is superconducting at 2.5 K due to its high electron count. In order to investigate the effect of Ru content on the superconductivity, materials with different Ru contents over  $\text{Mo}_{0.25}\text{Re}_{0.25}\text{Ru}_{0.25}\text{Rh}_{0.25}$  were also studied.  $\text{Mo}_{0.1}\text{Re}_{0.1}\text{Ru}_{0.55}\text{Rh}_{0.1}\text{Ti}_{0.15}$  (VEC = 7.20) shows the HCP phase with a  $T_C$  of 2.1 K. Decreasing the Ru content to  $\text{Mo}_{0.105}\text{Re}_{0.105}\text{Ru}_{0.527}\text{Rh}_{0.105}\text{Ti}_{0.158}$  (VEC = 7.158) and  $\text{Mo}_{0.118}\text{Re}_{0.118}\text{Ru}_{0.470}\text{Rh}_{0.118}\text{Ti}_{0.176}$  (VEC = 7.06) leads to superconductivity ( $T_C$  of 2.2 and 2.5 K, respectively), but along with a CsCl-type phase. Upon a further decrease in Ru content to  $\text{Mo}_{0.167}\text{Re}_{0.167}\text{Ru}_{0.25}\text{Rh}_{0.167}\text{Ti}_{0.25}$  (VEC = 6.674), although the  $T_C$  is comparatively high at 5.5 K, three phases (a dominant  $\sigma$  phase plus minor CsCl-type and HCP phases) are present. Wu *et al.*<sup>208</sup> reported the discovery of superconductivity in  $(\text{V}_{0.5}\text{Nb}_{0.5})_{3-x}\text{Mo}_x\text{Al}_{0.5}\text{Ga}_{0.5}$  ( $0.2 \leq x \leq 1.4$ ), which is a single BCC structure for  $x = 0.2$  and a mixture of BCC and A15 structures for higher  $x$  values. For the sample with  $x = 0.2$ , the BCC-structured HEA is not superconducting down to 1.8 K, whereas the A15 polymorph has a superconducting  $T_C$  (10.2 K) and estimated  $H_{C2}(0)$  of 20.1 T, which are the highest among HEA superconductors.

**4.8.7 HEA-derived superconductors.** Many HEA-derived oxides and tellurides also exhibit superconductivity, and the superconducting transition temperature is obviously higher than pure HEAs. Exploring this kind of material is a useful supplement to HEA-based superconductors. Sogabe *et al.*<sup>209</sup> synthesized  $\text{REO}_{0.5}\text{F}_{0.5}\text{BiS}_2$  with HEA-type REO-blocking layers. An obvious superconducting transition was observed for all the HEA-type samples, and the transition temperature is higher than that of typical  $\text{REO}_{0.5}\text{F}_{0.5}\text{BiS}_2$ . This phenomenon is mainly due to the effectiveness of the HEA states of the REO-blocking layers. Introducing the HEA effects into layered superconductors is believed to be an effective approach to improve the superconducting parameters such as  $T_C$ ,  $H_{C2}(0)$ , and so on. Shukunami *et al.*<sup>210</sup> synthesized HEA-type RE123 superconductors  $\text{Y}_{0.28}\text{Nd}_{0.16}\text{Sm}_{0.18}\text{Eu}_{0.18}\text{Gd}_{0.20}\text{Ba}_2\text{Cu}_3\text{O}_{7-\delta}$  and  $\text{Y}_{0.18}\text{La}_{0.24}\text{Nd}_{0.14}\text{Sm}_{0.14}\text{Eu}_{0.15}\text{Gd}_{0.15}\text{Ba}_2\text{Cu}_3\text{O}_{7-\delta}$  with a  $T_C$  above 90 K. Compared with traditional RE123 samples, the mixing entropy at the rare-earth site does not affect the  $T_C$  and critical current density ( $J_C$ ) of the RE123 samples. Mizuguchi *et al.*<sup>211</sup> synthesized polycrystalline  $\text{AgInSnPbBiTe}_5$  with an NaCl-type structure. This HEA exhibits superconductivity with a  $T_C$  of 2.6 K.  $\text{AgInSnPbBiTe}_5$  is the first HEA-type pseudo-binary superconductor having a cation site (Ag, In, Sn, Pb, and Bi) and an anion site (Te). Yamashita *et al.*<sup>212</sup> reported the synthesis of new HEA-type metal chalcogenides  $(\text{Ag},\text{In},\text{Pb},\text{Bi})\text{Te}_{1-x}\text{Se}_x$  ( $x = 0.0$ , 0.25, and 0.5) with a NaCl-type structure using high-pressure synthesis. Superconductivity with transition temperatures of 2.7, 2.5, and 2.0 K was observed with  $x = 0.0$ , 0.25, and 0.5, respectively. This trend may suggest that the superconducting properties can be improved by an increase in the entropy of mixing and it would be a useful strategy to explore new HEA-type superconductors with a high mixing entropy.

**4.8.8 Correlation of VEC or crystallinity with  $T_C$ .** A crucial factor that affects the stability of a solid solution without

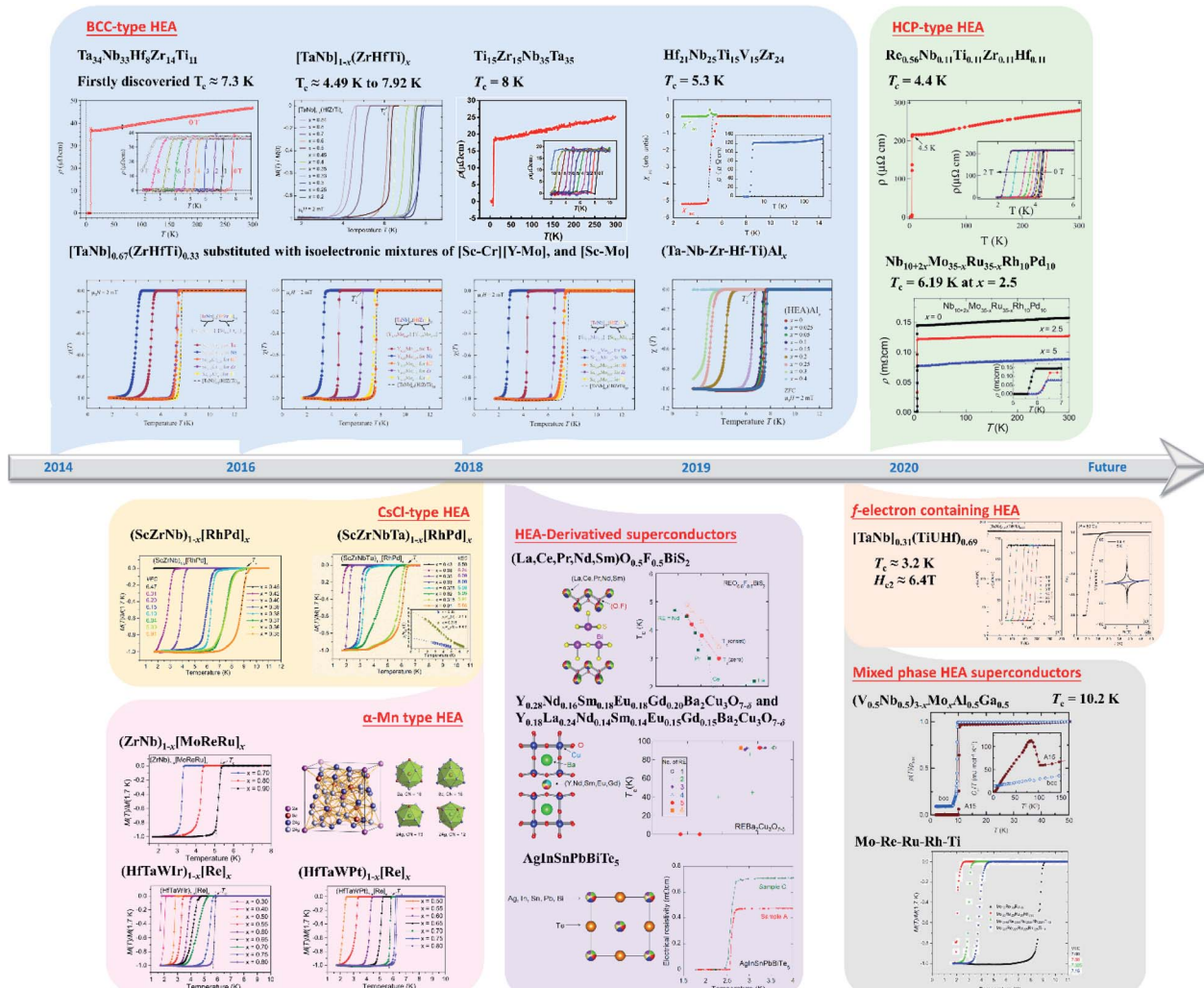


**Fig. 18** Evolution history of the application of HEAs in superconducting materials classified according to different material types. Reproduced with the permission from ref. 194. Copyright © 2014, American Physical Society. Reproduced with the permission from ref. 196. Copyright © 2016, National Academy of Sciences. Reproduced with the permission from ref. 199. Copyright © 2018, American Physical Society. Reproduced with the permission from ref. 201. Copyright © 2018, Frontiers. Reproduced with the permission from ref. 202. Copyright © 2019, Elsevier Ltd. Reproduced with the permission from ref. 203. Copyright © 2018, Royal Society of Chemistry. Reproduced with the permission from ref. 204. Copyright © 2019, American Physical Society. Reproduced with the permission from ref. 205. Copyright © 2020, Elsevier Ltd. Reproduced with the permission from ref. 206. Copyright © 2020, Springer Nature. Reproduced with the permission from ref. 207. Copyright © 2019, Elsevier Ltd. Reproduced with the permission from ref. 208. Copyright © 2020, Springer Nature. Reproduced with the permission from ref. 209. Copyright © 2018, The Japan Society of Applied Physics. Reproduced with the permission from ref. 210. Copyright © 2020, Elsevier Ltd. Reproduced with the permission from ref. 211. Copyright © 2019, The Physical Society of Japan. Reproduced with the permission from ref. 212. Copyright © 2020, Royal Society of Chemistry. Reproduced with the permission from ref. 215. Copyright © 2018, American Chemical Society.

considering the atomic-size effect is the VEC. Previous results have shown that the VEC plays a crucial role in their  $T_c$  values.  $T_c$  for the HEAs strongly depends on the VEC just like the Matthias plot of  $T_c$  vs. electron count in binary transition-metal-based alloys.<sup>196,199,215</sup> Taking BCC-type HEA superconductors  $(\text{TaNb})_{1-x}(\text{ZrHfTi})_x$  as an example,  $T_c$  increases with VEC and reaches the maximum value (7.3 K) near 4.7 K (light orange region in Fig. 19). A wider range of stable BCC-type VEC materials may be available at very fast cooling rates, which will be a rewarding addition to the knowledge base. The relationship between the VEC and  $T_c$  is also observed in CsCl-type superconductors such as  $(\text{ScZrNb})_{1-x}(\text{RhPd})_x$ .<sup>215</sup> The

superconductivity appears in the VEC range of 5.9–6.3, and the maximum  $T_c$  (9.3 K) appears at a VEC of 5.9. Considering the  $T_c$  values of all types of HEA superconductors, a full electron count trend can be observed. Small unit-cell BCC-type and CsCl-type HEAs seem to follow the two-peak character for binary alloys, while the complex  $\alpha$ -Mn-type HEAs do not follow this general trend. Apart from the above three types of HEAs, the novel HCP-type HEAs with the highest VEC among HEAs were gradually developed in the last year, which is an excellent addition to the HEA superconductors. The application of HEAs in the field of superconducting materials in recent years shows that the superconducting transition temperature of this type of

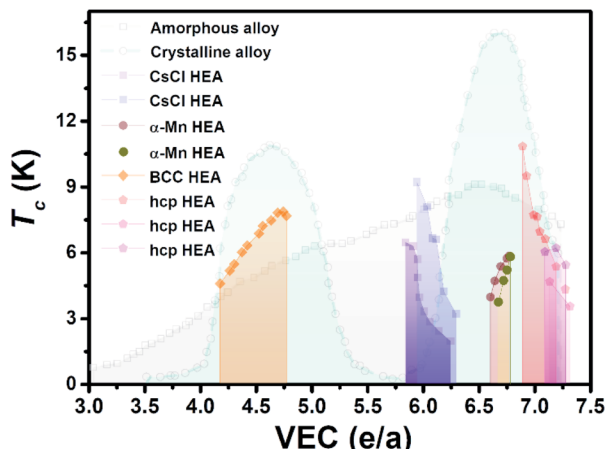


**Fig. 19** Relationship of VEC and crystallinity with the superconducting transition temperatures for BCC-type, CsCl-type,  $\alpha$ -Mn-type, and HCP-type HEA superconductors compared with amorphous alloys and crystalline alloys. The data were taken from ref. 218.

materials gradually increases, which is different from the traditional single-metal superconductors. It can deepen our understanding of superconductivity. In the future, the superconducting transition temperature of HEAs may reach the liquid nitrogen temperature (Table 3).

Apart from the influence of VEC on the superconducting performances, crystallinity is another issue that needs to be considered. A comparison of the  $T_c$  values of the crystalline transition metals and their alloys,<sup>216</sup> amorphous films,<sup>217</sup> and BCC-type HEAs revealed that the  $T_c$  of HEAs is clearly lower than those of the crystalline alloys and higher than those of the amorphous alloys. The fact that the  $T_c$  of HEAs lies between those of the crystalline alloy and amorphous material at the same electron count indicates that crystallinity has a prominent influence on  $T_c$ . Although detailed evidence of different crystallized samples has not been discovered, this suggests that the smearing of the electron energy *vs.* electron wave-vector relations and the broadening of the electronic density of states due to disorder probability lead to this phenomenon.

#### 4.9 Catalyst materials

A catalyst is known as a vitamin in the industry, which plays an important role in many industrial productions. It can reduce energy consumption, improve the selectivity and rate of reaction, and even change the elementary reaction. For example, in the basic ammonia synthesis and Fischer-Tropsch reactions in modern industry, the selection and preparation of catalysts play a decisive role in the types of products. Even the Nobel Prize in Chemistry has been awarded three times for the invention, improvement, and mechanism research of ammonia catalysts. Therefore, the development of a new catalyst system is of great importance for both scientific value and practical significance. As an “old” but “novel” alloy system, HEAs provide unlimited possibilities for the expansion of the catalyst family.

**4.9.1 HEAs for thermocatalysis.** Small-molecule oxidation reactions, such as ammonia and carbon monoxide, are critical

steps in the practical synthesis of nitric acid and efficient elimination of toxic pollutants. Moreover, they are efficient evaluation platforms for many unconventional model catalysts. Although numerous new catalysts have been explored, PtPdRh-based catalysts are still widely used in industrial ammonia oxidation. Except for the drawback of expensive precious metals, the high reaction temperatures ( $>800$  °C), unsatisfactory product selectivity, and degradation under continuous operation limit their large-scale application.<sup>219</sup>

HEAs have the potential to be used in thermocatalysis. Yao *et al.*<sup>65</sup> demonstrated quinary PtPdRhRuCe HEA NPs made by the CTS method and applied in ammonia oxidation. Introducing higher amounts of Ru and Ce not only improves the catalytic activity, but also lowers the Pt content. The conversion of NH<sub>3</sub> can be  $\sim 100\%$  and the selectivity toward NO<sub>x</sub> approaches 99% at a relatively low temperature (700 °C), as shown in Fig. 20a. For comparison, controlling catalysts (PtPdRhRuCe MMNPs) were prepared by the wet impregnation method, which produce a 18.7% yield of NO<sub>x</sub> under the same condition (Fig. 20b). The enhanced selectivity can be attributed to the homogeneous feature of the solid-solution NPs compared with the phase-separated catalysts. The stability test (Fig. 20c) shows that there is no degradation of the activity or selectivity over  $\sim 30$  h. Moreover, the precious metal content can be further reduced by substituting Pt with Co and eliminating Ru. Therefore, HEA NPs will be a promising candidate for the ammonia oxidation by rational materials design.

Ammonia is a promising liquid fuel for hydrogen storage, but its large-scale application is limited by the requirement of precious metal catalysts. During the utility of NH<sub>3</sub>, the efficient NH<sub>3</sub> decomposition is needed to release H<sub>2</sub> and eliminate NH<sub>3</sub> pollution. Apart from efficient but high-cost Ru as the catalyst, Xie *et al.*<sup>68</sup> synthesized CoMoFeNiCu NPs by precisely controlling the Co/Mo atomic ratio. Compared with the Ru catalyst, these HEA NPs exhibit improved the catalytic performance for NH<sub>3</sub> decomposition with an improvement factor of over 20, which is even better than those of traditional Co-Mo catalysts (Fig. 20e and f). The catalytic activity can be regulated by changing the Co/Mo ratio, thereby optimizing the surface properties and maximizing the reaction activity under different conditions (Fig. 20d). It is further found that their catalytic activity and kinetics show volcanic behavior independent of the Co/Mo ratio, which could be successfully explained by the nitrogen adsorption energy as the descriptor and the mixed surface site mechanism obtained by atomic simulation.

CO oxidation is a useful supplement for pollutant removal and test platform for catalysts. Qiu *et al.*<sup>220</sup> presented a versatile route to synthesize nanoporous HEA (np-HEAs) by combining bulk melting, fast cooling, and dealloying. Compared with the other two samples, the np-HEA with an oxide coating has the highest catalytic activity (Fig. 20k), which proves the synergistic effect between a thin oxide film and the HEA core. The presence of thin mixed-metal oxides on the surface of HEA ligaments may increase the dissociation efficiency of O<sub>2</sub>, which is considered to be the rate-limiting step for CO oxidation on Au- or Pt-based catalysts.<sup>221</sup> Different from TiO<sub>2</sub>-coated np-Au, which needs a high-temperature (600 °C) annealing process to break the

**Table 3** Overview with compositions, critical parameters, and structures of HEA superconductors

HEA superconductor	$T_C$ (K)	$H_{C2}$ (0) (T)	$H_{C1}$ (0) (mT)	Structure	Ref.
Ta <sub>34</sub> Nb <sub>33</sub> Hf <sub>8</sub> Zr <sub>14</sub> Ti <sub>11</sub>	7.3	8.2	32	BCC	194
Hf <sub>21</sub> Nb <sub>25</sub> Ti <sub>15</sub> V <sub>15</sub> Zr <sub>24</sub>	5.3	—	—	BCC	202
Nb <sub>21</sub> Re <sub>16</sub> Zr <sub>20</sub> Hf <sub>23</sub> Ti <sub>20</sub>	5.3	8.88	33	BCC	200
(TaNb) <sub>0.7</sub> (ZrHfTi) <sub>0.3</sub>	8.0	6.7	—	BCC	196
(NbV) <sub>67</sub> (HfZrTi) <sub>33</sub>	7.2	—	—	BCC	196
(TaV) <sub>67</sub> (HfZrTi) <sub>33</sub>	4.0	—	—	BCC	196
(TaNbV) <sub>67</sub> (HfZrTi) <sub>33</sub>	4.3	—	—	BCC	196
Ta <sub>34</sub> Nb <sub>33</sub> Hf <sub>8</sub> Zr <sub>14</sub> Ti <sub>11</sub>	7.3	8.2	—	BCC	213
NbTaTiZrFe	6.9	—	—	BCC	214
NbTaTiZrGe	8.4	1.3	—	BCC	214
NbTaTiZrSiV	4.3	—	—	BCC	214
NbTaTiZrSiGe	7.4	0.9	—	BCC	214
(ZrNb) <sub>0.1</sub> (MoReRu) <sub>0.9</sub>	5.3	7.9	—	$\alpha$ -Mn	203
(HfTaWIr) <sub>0.4</sub> Re <sub>0.6</sub>	4.0	4.7	—	$\alpha$ -Mn	203
(HfTaWPt) <sub>0.4</sub> Re <sub>0.6</sub>	4.4	5.9	—	$\alpha$ -Mn	203
(ScZrNbTa) <sub>0.65</sub> (RhPd) <sub>0.35</sub>	9.3	10.7	2.3	CsCl	215
(ScZrNb) <sub>0.63</sub> (RhPd) <sub>0.37</sub>	7.5	9.6	—	CsCl	215
Nb <sub>10+2x</sub> Mo <sub>35-x</sub> Ru <sub>35-x</sub> Rh <sub>10</sub> Pd <sub>10</sub>	6.19 K at $x = 2.5$	8.3 T at $x = 5$	—	hcp	205
Re <sub>0.56</sub> Nb <sub>0.11</sub> Ti <sub>0.11</sub> Zr <sub>0.11</sub> Hf <sub>0.11</sub>	4.4	8.3	—	hcp	204
[TaNb] <sub>0.31</sub> (TiUhf) <sub>0.69</sub>	3.2	6.4	—	f-Electron containing HEA	206
(V <sub>0.5</sub> Nb <sub>0.5</sub> ) <sub>3-x</sub> Mo <sub>x</sub> Al <sub>0.5</sub> Ga <sub>0.5</sub>	10.2	20.1	—	Mixed phase	208
Mo <sub>0.167</sub> Re <sub>0.167</sub> Ru <sub>0.25</sub> Rh <sub>0.167</sub> Ti <sub>0.25</sub>	5.5	—	—	Mixed phase	207
Mo <sub>0.1</sub> Re <sub>0.1</sub> Ru <sub>0.55</sub> Rh <sub>0.1</sub> Ti <sub>0.15</sub>	2.1	—	—	Mixed phase	207
Y <sub>0.28</sub> Nd <sub>0.16</sub> Sm <sub>0.18</sub> Eu <sub>0.18</sub> Gd <sub>0.20</sub>	93	—	—	HEA-derivatived	210
Y <sub>0.18</sub> La <sub>0.24</sub> Nd <sub>0.14</sub> Sm <sub>0.14</sub> Eu <sub>0.15</sub> Gd <sub>0.15</sub>	93	—	—	HEA-derivatived	210
AgInSnPbBiTe <sub>5</sub>	2.6	—	—	HEA-derivatived	211
(Ag <sub>0.237</sub> In <sub>0.215</sub> Pb <sub>0.268</sub> Bi <sub>0.258</sub> )Te <sub>1.23</sub>	2.7	18	—	HEA-derivatived	212
(Ag <sub>0.291</sub> In <sub>0.260</sub> Pb <sub>0.219</sub> Bi <sub>0.241</sub> )Te <sub>0.784</sub> Se <sub>0.195</sub>	2.5	19	—	HEA-derivatived	212
(Ag <sub>0.336</sub> In <sub>0.151</sub> Pb <sub>0.236</sub> Bi <sub>0.286</sub> )Te <sub>0.649</sub> Se <sub>0.344</sub>	2.0	—	—	HEA-derivatived	212

continuous TiO<sub>2</sub> coating and induce catalytic activity,<sup>221</sup> np-HEA has high activity and stability for CO oxidation without any activation process.

**4.9.2 HEAs for methanol oxidation.** The electrooxidation of methanol in acidic media can be described as a two-step process: adsorption of molecules on the metal surface and the dehydrogenation and oxidation of the adsorbate to CO<sub>2</sub>. So far, many precious metals (Pt–Ru, Ir–Pt alloys) have shown the best activity.<sup>222</sup> Recently, some ternary and quaternary alloys based on platinum-group metals (PGMs) have been considered as heterogeneous substrates for methanol electrooxidation, including CoPtRu, OsPtRu, IrOsPtRu, NiPtRuZr, and NiPtRhRu.<sup>223,224</sup> Research on the catalytic activity of alloys with more than five elements is still in its infancy.

In 2008, Tsai *et al.*<sup>225,226</sup> fabricated Pt<sub>50</sub>Fe<sub>11</sub>Co<sub>10</sub>Ni<sub>11</sub>Cu<sub>10</sub>Ag<sub>8</sub> NPs on gas-diffusion electrodes by radiofrequency sputter deposition. In terms of mass activities, electrodes with 5 nm NPs exhibit the best activity of 400–600 mA mg<sup>-1</sup>. Compared with Pt–Ru alloy, it also shows the lowest onset potential. Wang *et al.*<sup>227</sup> were the first to prepare the PdNiCoCuFe nanotube arrays (NTAs) by a template-assisted electrodeposition method. The NTAs exhibited catalytic activity and stability for methanol electrooxidation due to their large surface area, hollow structures, and synergistic effects. Its mass activity approaches 100 mA mg<sup>-1</sup>, which is better than Pd NTAs but inferior to Pt<sub>50</sub>–Fe<sub>11</sub>Co<sub>10</sub>Ni<sub>11</sub>Cu<sub>10</sub>Ag<sub>8</sub> NPs. In order to obtain better catalytical

performance, Chen *et al.*<sup>228</sup> fabricated nanoporous PtRuCuOsIr by the chemical dealloying of the AlCuPtRuOsIr precursor. Here, np-HEA achieves a higher mass activity (857.5 mA mg<sub>Pt</sub><sup>-1</sup>) and specific activity (3.0 mA cm<sup>-2</sup>) compared with the Pt/C catalyst (229.5 mA mg<sub>Pt</sub><sup>-1</sup> and 0.5 mA cm<sup>-2</sup>, respectively). In 2017, Yusenko *et al.*<sup>229</sup> prepared PGMs-containing HCP HEAs, which do not require high temperature or mechanical alloying. The HCP-Ir<sub>0.19</sub>Os<sub>0.22</sub>Re<sub>0.21</sub>Rh<sub>0.20</sub>Ru<sub>0.19</sub> and the two-phase Ir<sub>0.18</sub>–Os<sub>0.19</sub>Pt<sub>0.16</sub>Re<sub>0.17</sub>Rh<sub>0.16</sub>Ru<sub>0.15</sub> possess remarkable catalytic activity in a sulfuric acid solution compared with pure metals. Platinum atoms are responsible for the adsorption of methanol molecules, and transition metals provide surface oxides to oxidize the adsorbate at low potential. This theory may imply that nanostructured alloys are beneficial for electrooxidation, as shown by the oxidation potential of Ir<sub>0.18</sub>Os<sub>0.18</sub>Pt<sub>0.16</sub>Re<sub>0.17</sub>–Rh<sub>0.16</sub>Ru<sub>0.15</sub> ( $E_{ox} = 0.503$  V vs. SHE) and Ir<sub>0.19</sub>Os<sub>0.22</sub>Re<sub>0.21</sub>–Rh<sub>0.20</sub>Ru<sub>0.19</sub> ( $E_{ox} = 0.505$  V vs. SHE).

**4.9.3 HEAs for hydrogen evolution reaction (HER).** Electrochemical water splitting, including HER and oxygen evolution reaction (OER), is a promising hydrogen production method. In addition, it can also effectively relieve the energy crisis by converting electricity from renewable energy into chemical energy.<sup>230</sup> However, the practical cell voltage (1.8–2.0 V) is much larger than the theoretical value (1.23 V), causing low efficiency and poor economic effectiveness. It is well known that Pt-based catalysts accelerate the HER kinetics, but low-Pt or

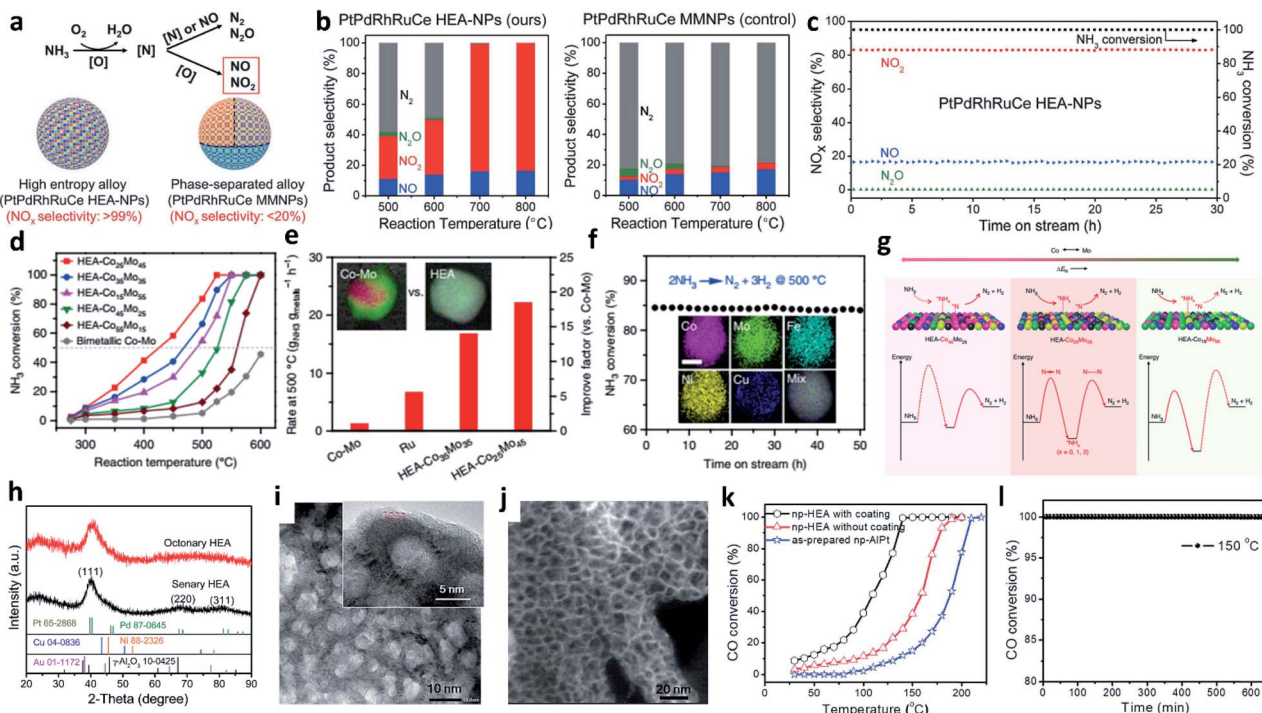


**Fig. 20** (a) Differences in performance between the PtPdRhRuCe NPs and PtPdRhRuCe MMNPs to NH<sub>3</sub> oxidation. (b) Product distribution and conversion of NH<sub>3</sub> for the above catalysts. (c) Catalytical stability of PtPdRhRuCe HEA NPs. Reproduced with the permission from ref. 65. Copyright © 2018, American Association for the Advancement of Science. (d) NH<sub>3</sub> conversions over different HEA-Co<sub>x</sub>Mo<sub>y</sub> NPs and bimetallic Co–Mo with different Co/Mo ratios. (e) Comparison of reaction rates among bimetallic Co–Mo, Ru, and HEA-Co<sub>x</sub>Mo<sub>y</sub> catalysts ( $T = 500\text{ }^\circ\text{C}$ ). (f) Stability measurement tests of the HEA-Co<sub>25</sub>Mo<sub>45</sub> catalyst. (g) Schematic of the reaction mechanism in NH<sub>3</sub> decomposition. Reproduced with the permission from ref. 68. Copyright © 2019, Springer Nature. XRD patterns (h), TEM images (i), and dark-field STEM image (j) of senary and octenary alloys after dealloying. (k) CO conversion of np-HEA with and without an oxide coating. (l) Durability of np-HEA with an oxide coating. Reproduced with the permission from ref. 220. Copyright © 2019, Royal Society of Chemistry.

non-Pt catalysts are more promising in terms of cost effectiveness. Based on the “volcano plot” between the activity and Me–H bond strength, multicomponent alloys are expected to possess higher activities due to the synergetic effects and partially filled d orbitals.<sup>231</sup> Consequently, HEAs with a disordered structure, metastable characteristics, and tunable compositions are reasonable to catalyze the HER.

In order to achieve the universality of HER catalysts in all kinds of electrolytes, the corrosion resistance of metal-based catalysts is the primary problem to be resolved, which is exactly the superiority for HEAs. Zhang *et al.*<sup>232</sup> reported that Ni<sub>20</sub>Fe<sub>20</sub>Mo<sub>10</sub>Co<sub>35</sub>Cr<sub>15</sub> HEA with high corrosion resistance can be used as a high-performance HER electrocatalyst in pH-universal electrolytes. The overpotential of HEA is only 107 mV in acid solution and 172 mV in the basic solution at 10 mA cm<sup>-2</sup>, which is much better than that of the dual-phase counterpart and even comparable to most of the reported noble-metal-free catalysts (Fig. 21a–c).

Although bulk HEAs have shown catalytic activity for HER in the previous work,<sup>232</sup> the performance of catalysts represents a positive correlation with the electrochemically active surface area. Therefore, reducing HEAs to the nanoscale is a challenging task.<sup>233</sup> Nanoporous metals prepared by the dealloying strategy have shown great promise in catalysis, energy storage, sensing, and so on. In order to increase the surface area, Qiu

*et al.*<sup>220</sup> presented a general approach to synthesize np-HEAs by combining bulk melting, fast cooling, and dealloying. Senary AlNiCuPtPdAu and octenary AlNiCuPtPdAuCoFe were synthesized with sizes of 2–3 nm and tuned by dealloying the precursors. After getting activated by cyclic voltammetry in acidic solutions, np-HEA exhibits a higher current density and a smaller Tafel slope (28 mV dec<sup>-1</sup>) compared with Pt/C. The Pt mass-specific activity of np-HEA is 6.9 A mg<sup>-1</sup>, which is 5.5 times that of Pt/C. Even when all the noble metals are taken into account, the mass activity (2.5 A mg<sup>-1</sup>) is still much higher than that of Pt/C (1.3 A mg<sup>-1</sup>). In addition, np-HEA is very stable for 2000 CV cycles (Fig. 21g). For the sake of reducing the noble metal content of the HEA, Jin *et al.*<sup>234</sup> obtained np-HEAs by dealloying precursor alloys. In addition, np-HEAs greatly improved the electrochemical cycling stability due to the high-entropy effect and slow diffusion effect of HEAs. Np-AlNiCoIrMo possesses the best HEA performance in a series of np-HEAs with a Tafel slope of 33 mV dec<sup>-1</sup> in acidic solutions (Fig. 21h). Besides np-HEAs, HEA NPs are important materials with great development potential, and their uniform dispersion on the carrier is significantly important for its application. For example, Gao *et al.*<sup>98</sup> presented a FMBP strategy to immobilize HEA NPs on granular supports. This strategy ensures that the mixed-metal precursors can be rapidly pyrolyzed at higher temperatures to produce small-sized nuclei. The FeCoPdIrPt

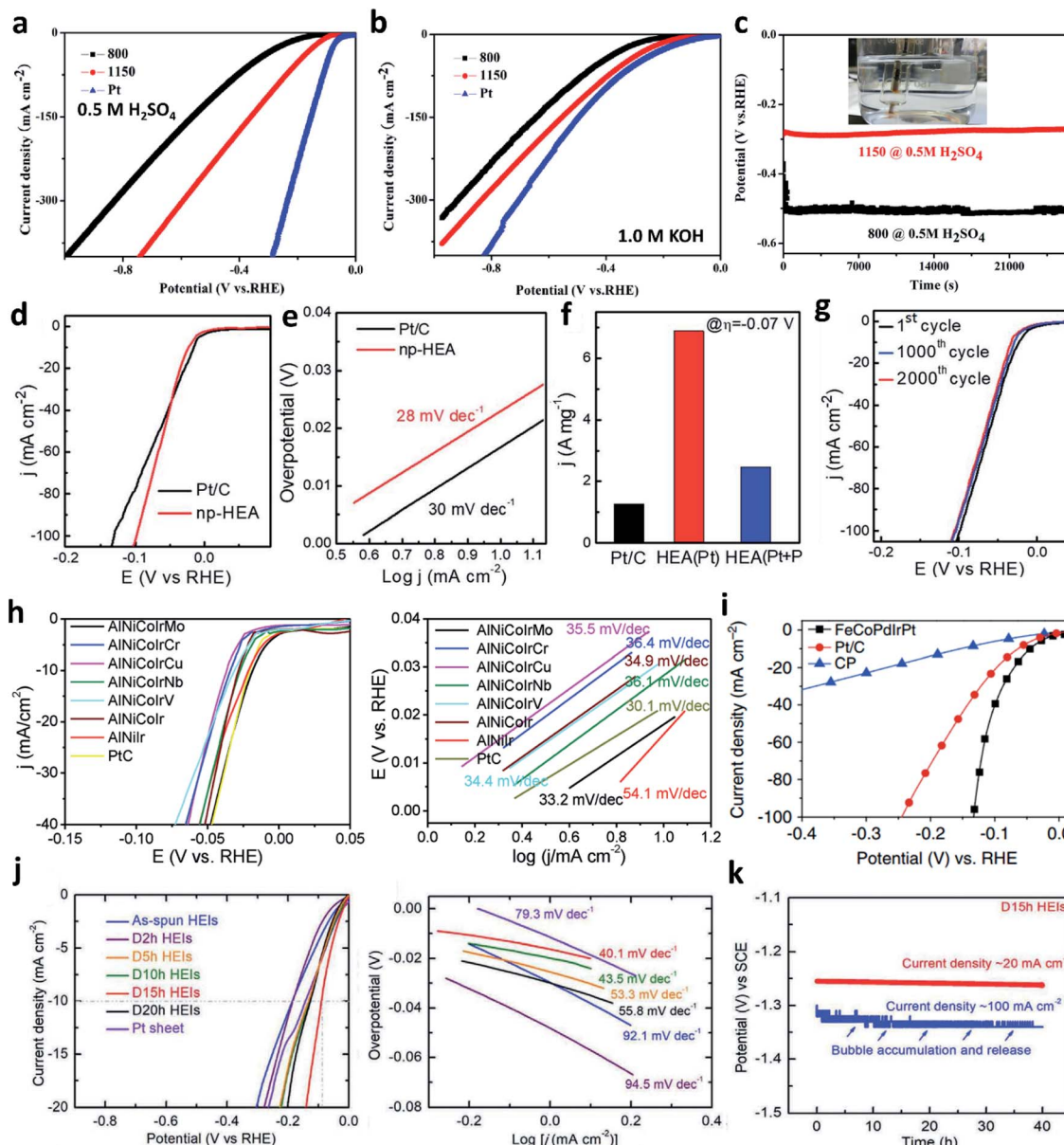


**Fig. 21** Polarization curves of dual-phase alloy and HEA in an acidic solution (a) and an alkaline solution (b). (c) Stability of HEA in an acidic solution. Reproduced with the permission from ref. 232. Copyright © 2018 Elsevier Ltd. HER polarization curves (d), Tafel curves (e), mass-specific activities at 0.07 V (f), and durability test (g) of np-HEA. Reproduced with the permission from ref. 220. Copyright © 2019, Royal Society of Chemistry. (h) HER polarization and the corresponding Tafel curves of FeCoPdIrPt HEA. Reproduced with the permission from ref. 234. Copyright © 2019 WILEY-VCH Verlag GmbH & Co. KGaA, Weinheim. (i) Activities toward HER of the prepared FeCoPdPtIr@GO by the FMBP strategy. Reproduced with the permission from ref. 98. Copyright © 2020, Springer Nature. (j) Polarization curves and Tafel plots of nonnoble HEI. (k) Catalytic stability of the HEI. Reproduced with the permission from ref. 235. Copyright © 2020 WILEY-VCH Verlag GmbH & Co. KGaA, Weinheim.

HEA NPs have high stability (150 h), which is 26 times higher than that of Pt/C at an overpotential of 100 mV (Fig. 21i). The improvement in HER performance is due to the synergistic effect of elements in HEA NPs.

The ultimate goal for advanced HER catalysts is noble-metal-free materials. Hence, Jia *et al.*<sup>235</sup> reported a nonnoble high-entropy FeCoNiAlTi intermetallic (HEI). The results show that the HEI exhibits good activity under alkaline conditions, and the overpotential is 88.2 mV at 10 mA cm<sup>-2</sup> and a Tafel slope of 40.1 mV dec<sup>-1</sup>, which is equivalent to that of noble metal

catalysts (Fig. 21j and k). Its superior performance vests in the fine-tuning of the electronic structure through chemical synergy and surprising structural site isolation effect.

**4.9.4 HEAs for OER.** Improving the sluggish kinetics for OER is important for water splitting and metal-air batteries.<sup>236</sup> Among the various electrocatalysts, noble metals (such as Ir and Ru) are superior OER electrocatalysts.<sup>237,238</sup> Considering their high cost and low abundance, reducing the content of noble metals is a desirable direction to enhance the catalytic activity.<sup>239</sup> HEAs exhibit potential applications in catalysis/

electrocatalysis because of the high-entropy feature and severe lattice distortion. Therefore, nanostructured HEAs with a high specific surface area and abundant active sites can improve the catalytic activity.

Based on the deficiency of noble metal catalysts, decreasing their content and further lowering the cost are two research hotspots for Ir- or Ru-based electrocatalysts. For example, Jin *et al.*<sup>234</sup> controllably incorporated Ir with four metal elements at merely ~20 at% Ir by dealloying Al-based alloys. The obtained np-HEA provides unlimited possibilities for adjusting the electronic properties of the alloy and maximizing the catalytical activity. For example, the addition of Co to the AlNiIr alloy can decrease its activity. In terms of AlNiCoIr alloy, elemental Mo and V play a positive role, while Nb and Cr play a negative role. Therefore, the np-AlNiCoIrMo affords a lower onset potential of 1.42 V and a smaller Tafel slope of 55.2 mV dec<sup>-1</sup> (Fig. 22a and b). At the current density of 10 or 20 mA cm<sup>-2</sup>, the overpotentials are only 233 and 255 mV, respectively, which are much lower than those of Ir-based nanocatalysts. Moreover, due to the high-entropy effect and slow diffusion effect of HEA, quinary np-HEAs can also greatly improve the structural and catalytic durability (Fig. 22c).

In order to lower the cost, non-noble-metal-based HEA catalysts are the next development focus. Waag *et al.*<sup>95</sup> reported the synthesis of colloidal CoCrFeMnNi NPs with equimolar stoichiometry by liquid-phase, ultrashort-pulsed laser ablation of the consolidated and heat-treated micro-powders. Electrochemical analysis reveals the unique redox behavior of HEA NPs immobilized on carbon black in an alkaline solution and its potential application as the OER electrocatalyst. In the actual situation, many kinds of easily oxidized metals would be transferred into oxides or oxyhydroxides on the HEA surfaces before the initiation of OER. For example, Dai *et al.*<sup>240</sup> reported MO<sub>x</sub> (M = Mn, Fe, Co, and Ni) nanosheets on MnFeCoNi HEA. After electrochemical activation, the compound MO<sub>x</sub> (M = Mn, Fe, Co, and Ni) nanosheets are grown on the MnFeCoNi HEA to form a core-shell structure with enhanced surface area and active site. The core-shell structure exhibits a low overpotential (302 mV at 10 mA cm<sup>-2</sup>), a small Tafel slope (83.7 mV dec<sup>-1</sup>), and long-term stability (over 20 h) in an alkaline electrolyte, which is comparable to those of RuO<sub>2</sub>. In this paper, a general and customized strategy for new HEA-based catalysts has been proposed to improve the OER performance by replacing and/or alloying catalytic components (Fig. 22d-f). Another example is that Qiu *et al.*<sup>241</sup> controllably incorporated inexpensive metals into one nanostructured alloy with an oxidized surface by the dealloying route. The np-HEAs covered with high-entropy (oxy) hydroxides (HEOs) exhibit OER activity. The results show that np-AlNiCoFeX (X = Mo, Nb, Cr) play a leading role in improving the OER activity. Compared with ternary and quaternary HEAs, quinary HEAs provide more structural and chemical degrees of freedom to improve the catalytic performance. After exploring quinary HEAs, the np-AlNiFeCoMo shows the lowest onset potential (1.44 V) and smaller Tafel slope (46 mV dec<sup>-1</sup>) than those of the other HEAs. To reach 10 mA cm<sup>-2</sup>, the required potential is just 1.47 V. The HEA containing these five components promotes rapid electron transport and interfacial

reaction between the alkaline solution and the electrode. Compared with the other combinations, these effects lead to an increase in the OER performance. In addition, the np-AlNiCoFeMo shows no obvious change in potential for 50 h (Fig. 22i). Huang *et al.*<sup>242</sup> developed an approach to grow metal-organic frameworks (MnFeCoNiCu HEAN MOFs) on carbon cloth by a one-step solvothermal method. Following pyrolysis at a suitable temperature and time, it produces FCC-phase MnFeCoNiCu HEA NPs at a size of sub-5 nm. The NPs exhibit many lattice defects (twins, dislocations, and stacking faults), which are favorable for the catalytic process. A much smaller overpotential of 263 mV enables the OER in 1.0 M KOH at a current density of 10 mA cm<sup>-2</sup> with a low Tafel slope of 43 mV dec<sup>-1</sup>. This performance along with excellent stability is much better than that of the state-of-the-art electrocatalysts. This work shows that lattice deformation controls the atomic displacement on the surface of the NPs, which contributes to their higher catalytic activity than the most advanced counterparts reported in the literature.

**4.9.5 HEAs for oxygen reduction reaction (ORR).** The sluggish kinetics of ORR is an urgent bottleneck in the application of metal-air batteries and fuel cells.<sup>243</sup> Although Pt-based materials are the most active electrocatalysts, their high cost and low abundance hinder their practical applications. Therefore, exploring noble-metal-free electrocatalysts have drawn attention in the past decade.<sup>244</sup> Besides reducing the Pt-loading amount, the performance of single-metal electrocatalysts is limited by their inherent characteristics, and this aporia can be resolved by alloying. The reason for this enhanced activity of alloys is due to three factors: synergistic effect, ligand effect, and strain effect. The first effect indicates that the presence of another metal can have a positive impact on the ORR, such as facilitated OH adsorption on the Pt surface. The ligand effect is a short-range electronic charge-transfer effect and the strain effect is a long-range geometric lattice strain. Both of them result in a modified electronic structure of Pt, making the Pt d-band center downshift to the Fermi level.<sup>245-247</sup> The large specific surface area, high material utilization efficiency, and nanoscale-size effect of HEAs make them very attractive to be ORR catalysts.

Qiu *et al.*<sup>220</sup> fabricated np-HEAs with a low Pt loading by using a fast cooling and dealloying strategy, which have uniformly distributed nanoligaments. The np-HEA exhibits a significant positively shifted halfwave potential (0.90 V vs. RHE) compared with Pt/C (0.82 V). In terms of mass activity, np-HEA also delivers a high value of 2.24 A mg<sup>-1</sup>, which is 10 times that of Pt/C (0.22 A mg<sup>-1</sup>) and much higher than the 2020 target set by the U.S. Department of Energy (DOE). Even when the masses of all noble metals are considered, the mass activity is still 0.87 A mg<sup>-1</sup>. After 100 000 cycles, np-HEA maintains 92.5% of its initial activity in acidic solutions (Fig. 23c).

Li *et al.*<sup>248</sup> reported a top-down dealloying synthesis method to incorporate five immiscible metals in one nanoscale FCC phase. By predetermining four elements (Al, Cu, Ni, and Pt) and alternating the fifth element including Pd, V, Co, Mn, etc., a series of np-HEAs with Pt contents of 20–30 at% were obtained. By studying and screening the composition effect, np-

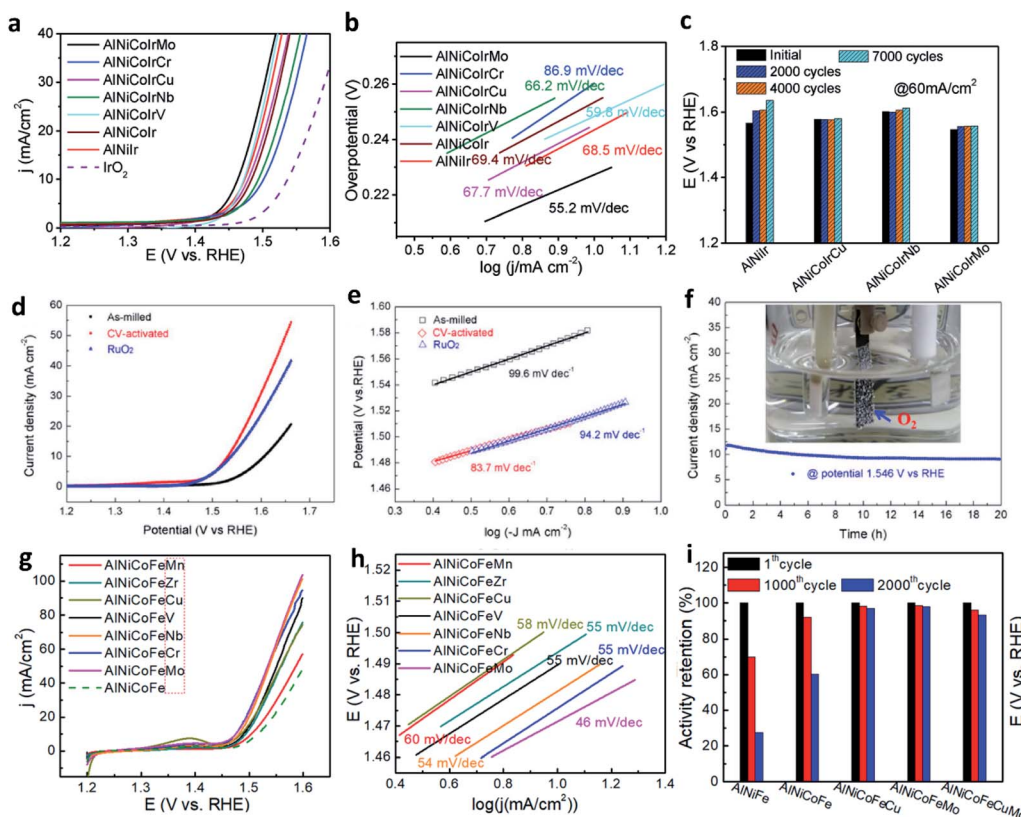


**Fig. 22** (a) OER polarization and (b) Tafel curves of all np-AlNiCoIrX samples and IrO<sub>2</sub>. (c) Potential changes of these samples after long-term tests in an acidic solution. Reproduced with the permission from ref. 234. Copyright © 2019, WILEY-VCH Verlag GmbH & Co. KGaA, Weinheim. (d) Electrochemical characterizations of the MnFeCoNi HEA in a basic solution. (e) Tafel slopes derived from the LSV curves shown in (d). (f) Chronamperometry curve of the activated HEA and electrolyzer with three-electrode configuration. Reproduced with the permission from ref. 240. Copyright © 2019, Elsevier Ltd. (g) LSV curves of the np-AlNiCoFeX electrodes. (h) The corresponding Tafel curves of the np-AlNiCoFeX. (i) Current retentions at 1.55 V after long-term cycling. Reproduced with the permission from ref. 241. Copyright © 2019, American Chemical Society.

AlCuNiPtMn exhibits the best ORR catalytic activity (the highest halfwave potential of 0.945 V in acidic media and a 16-fold mass activity of Pt/C) and durability, well exceeding the Pt/C catalysts, as shown in Fig. 23d–f.

**4.9.6 HEAs for carbon dioxide reduction reaction (CO<sub>2</sub>RR).** Converting gaseous CO<sub>2</sub> into fuels by the electrocatalytic reduction of carbon dioxide (CO<sub>2</sub>RR) is a useful attempt to resolve the problems posed by the ever-increasing energy crisis. However, its practical application is severely limited due to its unsatisfactory activity and selectivity derived from the sluggish kinetics and competition reaction of HER.<sup>249</sup> Although precious metal catalysts demonstrate high activity toward CO<sub>2</sub>RR, low reserves and high prices limit their practical applications in industry. Inexpensive copper has attracted much attention due to its ability to convert carbon dioxide into hydrocarbon fuel. However, due to the large amount of hydrogen generated, copper-based materials show limited selectivity. Alloying is a conventional and efficient strategy to resolve the above problems. Recently, HEAs have been developed that have shown potential in methanol electrooxidation, ORR, HER, and OER. The application of HEAs in CO<sub>2</sub>RR has rarely been reported until now. Therefore, it has great potential to expand their applications in CO<sub>2</sub>RR.

Nellaippan *et al.*<sup>250</sup> used nano-AuAgPtPdCu to convert CO<sub>2</sub> into hydrocarbons in 2020. A high faradaic efficiency of near 100% for gas products (CO, CH<sub>4</sub>, C<sub>2</sub>H<sub>4</sub>, and H<sub>2</sub>) could be obtained at a low potential (−0.3 V vs. RHE). The reason for the high activity and selectivity can be attributed to the reversal in adsorption trends for two out of the total eight intermediates, namely, \*OCH<sub>3</sub> and \*O on the Cu(111) and HEA surfaces. Although there are many elements in the catalyst, its electrocatalytic activity is mainly described by the presence of redox-active Cu metals (Cu<sup>2+</sup>/Cu<sup>0</sup>), while other metals only offer synergistic effects. At the same time, Pedersen *et al.*<sup>251</sup> proposed a platform to discover new catalysts for the CO<sub>2</sub>RR and CORR, such as CoCuGaNiZn and AgAuCuPdPt HEAs. Based on the necessary but insufficient criteria for weak H adsorption and strong CO adsorption, the authors predicted the local optimum composition of disordered alloys, and also provided an understanding of how to adjust the composition to affect the distribution of adsorption energy and affinity of H<sub>2</sub> generation.

#### 4.10 Shape memory alloys (SMAs)

Stress-induced transformation, including stress-induced martensitic transformation (SIMT) and mechanical twinning,

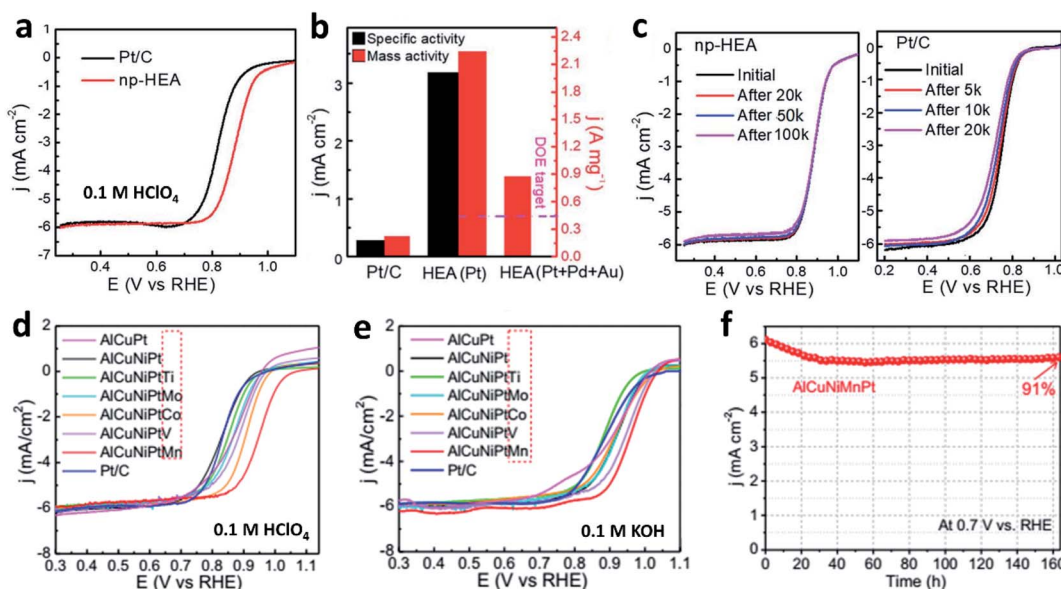


Fig. 23 (a) ORR polarization curves of np-HEA. (b) Specific and mass activity of np-HEA. (c) Durability after different cycles in O<sub>2</sub>-saturated 0.1 M HClO<sub>4</sub>. Reproduced with the permission from ref. 220. Copyright © 2019, Royal Society of Chemistry. ORR polarization curves of np-HEA in acidic (d) and alkaline (e) solutions. (f) Long-term current–time curve of the np-AlCuNiMnPt for ORR. Reproduced with the permission from ref. 248. Copyright © 2020, Elsevier Ltd.

is an important way to improve the plastic deformation ability of traditional alloys. Following the pioneering works of Kurdumov, Buehler discovered the shape memory effect phenomenon,<sup>253</sup> and shape memory alloys were created. For example, TiNi-based alloys<sup>254</sup> were extensively developed for various biomedical applications such as a metallic implant material<sup>255</sup> and became industrial SMAs as they experience a martensitic transformation (MT) of the thermoelastic type. The traditional method is to adjust the properties of TiNi SMAs by adding Zr, Hf, Pd, Au, Co, and Cu.<sup>256</sup> However, these shape memory materials are prone to a measure of plastic relaxation at the austenite/martensite interface (generation and movement of total dislocations). Subsequently, thermal cycling effects<sup>257</sup> (or thermal fatigue) and degradation of shape memory effect<sup>258</sup> appear, which have limited their industrial applications so far. The B2 structure<sup>33</sup> and the slow diffusion and resistance to the plastic deformation processes for HEAs facilitate the realization of the diffusion-less MT. Therefore, HEA could be a promising candidate for the efficient high-temperature SMAs.

Preventing irreversible plastic deformation during reversible MT is one of the methods to improve shape memory properties. In 2014, Firstov *et al.*<sup>252</sup> were the first to observe the MT phenomenon and shape memory in Ti<sub>16.667</sub>Zr<sub>16.667</sub>Hf<sub>16.667</sub>Ni<sub>25</sub>Cu<sub>25</sub> with a M<sub>s</sub> (MT starting temperature) and A<sub>f</sub> (austenitic transformation finishing temperature) of 500 K and 610 K, respectively. In order to improve the performance of famous Ti-Ni alloy, HE-SMAs were designed by substituting Ti atoms by Zr and Hf and adding Co and Cu to substitute Ni atoms. In industrial applications, due to the lack of understanding of high-temperature MT characteristics, high-temperature SMAs have remained underdeveloped. Firstov *et al.*<sup>259</sup> proposed that HEAs could be a solution to the plastic deformation problem in

high-temperature SMAs, and they concluded the Ti<sub>16.667</sub>Zr<sub>16.667</sub>Hf<sub>16.667</sub>Co<sub>10</sub>Ni<sub>25</sub>Cu<sub>15</sub> exhibited the best performance of reversible shape memory strain (1.63%) over 800 °C. In recent years, Chen<sup>260</sup> and Lee<sup>261</sup> *et al.* also studied the effects of heating treatment at 1000 °C on the transformation behavior and shape memory functions of (TiZrHf)<sub>50</sub>Ni<sub>25</sub>Co<sub>10</sub>Cu<sub>15</sub>. After annealing, it reveals a broad transition temperature with M<sub>s</sub> = 36.0 °C and M<sub>f</sub> = -80.4 °C by a three-point bending test. The results show a reversible strain of 4.8% under 650 MPa with a much higher output work density, which is better than that of the Ti<sub>50</sub>Ni<sub>50</sub> alloy. The non-oxygen stable Ti<sub>2</sub>Ni-like phase was partially dissolved by solution treatment. This phenomenon leads to an increment in the Ti, Zr, and Hf contents in the matrix, which results in an increase in the M<sub>s</sub> and A<sub>f</sub> temperatures. Meanwhile, the solution treatment induces a high-entropy effect and increases the degree of lattice distortion. The distortion further causes an increase in the friction force during the MT process, which leads to a broad transformation temperature range. The results show that solution treatment is an effective way to improve the functional performance of HE-SMAs.

Apart from the most widely studied TiZrHfNiCoCu HEA, there are other kinds of shape memory HEAs. For instance, Canadinc *et al.*<sup>262</sup> presented the MT characteristics of (Ni-Pd)<sub>50</sub>(Ti-Hf-Zr)<sub>50</sub> alloys. They were the first to report the austenite finish temperatures beyond 1070 K in pure NiTi-based SMAs. The increase in transformation temperature, transformation stress, and recovery strain at a high temperature can be attributed to the high configurational entropy of alloys. Wang *et al.*<sup>263</sup> were the first to report the prominent superelastic properties in TiZrHfAlNb HEAs, which are revealed by the maximum total recovery strain, fully recoverable strain, and corresponding tensile strength of up to 5.2%, 4.0%, and

900 MPa, respectively. In order to lower the manufacturing cost, Lee *et al.*<sup>264</sup> designed CrMnFeCoNi HEA with the shape memory feature at high temperature. It shows heat-induced and stress-induced MT between the FCC and HCP phases. The shape recovery temperature in non-equiautomic CrMnFeCoNi alloys can be increased to 698 K, which is much higher than that of conventional SMAs. It is also comparable to that of B2-based SMAs containing Pd, Pt, Zr, and Hf. This result opens a wide range for 3d HEAs to be applied in high-temperature SMAs. Piorunek *et al.*<sup>265</sup> explored a new HE-SMA (NiCuPdTiZrHf), which provides the maximum shape memory strain of 15%. Therefore, this material is expected to exhibit higher shape memory strain. Peltier *et al.*<sup>266</sup> studied the shape memory effect of NiCuTiHfZr, which can be maintained for 200 cycles between 25 and 325 °C without the protection of inert gases. These results show that the alloy can be effectively used in high-temperature actuators.

## 5. Conclusions and outlook

Although over 3700 papers related to HEAs have been published since 2004, a deeper understanding of the HEA family is still in its infancy. Therefore, several outstanding issues and future prospects can be put forward at this juncture:

1. Fundamental understanding of HEAs. More fundamental and basic scientific studies toward HEAs are required, such as prediction of phase stability and microstructure evolution. Since traditional alloy science is mainly on account of the study of materials with a few elements, what happens in HEAs would cause many concerns and become a valuable scientific problem.

2. Processing and characterization of HEAs. Although the bulk and nanostructured HEAs have been widely explored in recent years, novel synthesis methods that are targeted to particular applications are imperative. For example, HEAs can be fabricated by a forging process containing transitional mechanical preparation means with a nano-chemical approach, which can be used to realize a combination of engineering and functional applications. Advanced characterization methods, such as ground neutron and synchrotron radiation diffraction, high-resolution TEM, and atomic probe microscopy, are needed to reveal the deformation mechanism of HEAs at the atomic level.

3. Developing more HEA systems. HEA is an extensive “mineral reserve” with untold alloy systems. The understanding of novel HEAs is still very limited and primary. In order to further comprehend the capacity of HEAs, more elements and combinations need to be developed. For example, lightweight HEAs can be used in mobile devices, battery electrodes, and transportation industries.

Equimolar compositions of HEAs are usually the easiest ones to be obtained; however, they may not have the best properties. Therefore, there may be more wealth in non-equimolar alloys with carefully designed compositions and customized microstructures. A good way to find high-performance alloy systems is to start with an equimolar alloy and then extract the required non-equimolar components. Available synthesis strategies include the dopants of metallic elements and following

dealloying and even the dopants of nonmetallic elements (N, B, C, etc.) can be used to render unique properties and performances.

4. Developing high-entropy chemistry and expanding more practical applications. More investigations on high-entropy oxides, nitrides, carbides, MXenes,<sup>267</sup> and their compositions are needed. A certain number of surveys have suggested that four core effects of HEAs also apply to high-entropy ceramics. Moreover, many hopeful characteristics have been applied to the diffusion barrier layer and functional coatings.

A reasonable design of the phase structure engineering can make HEAs possess many unexpected characteristics, such as catalysis, invar, magnetism, and so on. Therefore, it promotes the development of latent groundbreaking applications, such as diffusion barrier layer of electronic devices, soft magnetic materials, batteries,<sup>268</sup> catalysts,<sup>269–271</sup> and medical applications.<sup>272–276</sup> Due to the unique design strategy and novel properties, HEAs and other high-entropy materials (such as ceramics or polymers) may be applied in more fields than the above applications. For example, oxides derived from HEAs have shown excellent performance as cathode materials in alkali-metal-ion batteries, which is mainly due to the high-entropy effect. This exciting new virgin land is waiting for more explorations.

5. Study on the structure–activity relationship of functional materials. In emerging fields, the performances of materials usually have close relationships with their structures and evolution. Therefore, the *in situ* characterizations<sup>277</sup> and high-precision simulations are urgently needed. Compared to density functional theory calculations, the calculated phase diagram (CALPHAD) method allows users to employ thermodynamic and kinetic calculations based on different phenomena. However, multiple elements and microstructures (solid solutions) of HEAs make the computational process much more complicated and time consuming than traditional alloys. Moreover, there is a certain gap between the experimental results and the CALPHAD method. Therefore, it is very important to establish a dependable database by the “Materials Genome Initiative.” Advanced calculation methods, which simulate the dislocation-related properties in HEAs, are a research hotspot.

6. Establishment of database based on high-throughput preparation. Existing databases need to be evaluated to find potential applications, which can resolve many bottlenecks encountered in traditional materials. Therefore, it must be remembered to correlate the HEA data with industrial applications and take advantage of their promising features. Researchers can get closer to using or modifying HEAs to meet application requirements through this effort. High-throughput screening tests are an essential part of this strategy. A series of small samples with different compositions or a kind of sample with a composition gradient can be prepared by using high-throughput experimental method in HEA research. With rapid developments in characterization, measurement, and calculation techniques, a large amount of data and credible relationships between the composition and properties can be obtained within a short time.

Meanwhile, we put forward two prospects for HEAs. The first one is that whether HEAs can show unique properties due to the uniqueness and limitations of their nanostructures. When the size of the material is reduced to the nanoscale, strong strain and high surface state are introduced, which can lead to the evolution of HEA performance with a decrease in the dimensions. The second one is to promote the practical application of HEAs. The future development direction of HEAs is to unprecedentedly combine the mechanical properties and functional properties of the alloy composition, such that the alloy composition has multifunctionalities and unlimited potential. In brief, we anticipate that the significant momentum in this field can continue, and the research of HEAs moves toward the application of these materials in various engineering designs.

## Conflicts of interest

The authors declare that they have no known competing financial interests or personal relationships that could have appeared to influence the work reported in this paper.

## Acknowledgements

This work was granted financial support from the China Postdoctoral Science Foundation (2019M650173), the Certificate of postdoctoral research grant in Henan province, and the National Natural Science Foundation of China (Grant No. 21975225 and 51902293).

## References

- Q. F. He, Z. Y. Ding, Y. F. Ye and Y. Yang, *Jom*, 2017, **69**, 2092–2098.
- J. C. Williams and E. A. Starke, *Acta Mater.*, 2003, **51**, 5775–5799.
- E. O. Ezugwu and Z. M. Wang, *J. Mater. Process. Technol.*, 1997, **68**, 262–274.
- M.-H. Tsai, *Entropy*, 2013, **15**, 5338–5345.
- H. S. Oh, S. J. Kim, K. Odbadrakh, W. H. Ryu, K. N. Yoon, S. Mu, F. Kormann, Y. Ikeda, C. C. Tasan, D. Raabe, T. Egami and E. S. Park, *Nat. Commun.*, 2019, **10**, 2090.
- J. W. Yeh, S. K. Chen, S. J. Lin, J. Y. Gan, T. S. Chin, T. T. Shun, C. H. Tsau and S. Y. Chang, *Adv. Eng. Mater.*, 2004, **6**, 299–303.
- J.-W. Yeh, *Ann. Chim.-Sci. Mat.*, 2006, **31**, 633–648.
- K.-H. Cheng, C.-H. Lai, S.-J. Lin and J.-W. Yeh, *Eur. J. Control*, 2006, **31**, 723–736.
- K. Y. Tsai, M. H. Tsai and J. W. Yeh, *Acta Mater.*, 2013, **61**, 4887–4897.
- W. H. Liu, Y. Wu, J. Y. He, T. G. Nieh and Z. P. Lu, *Scr. Mater.*, 2013, **68**, 526–529.
- O. N. Senkov, G. B. Wilks, J. M. Scott and D. B. Miracle, *Intermetallics*, 2011, **19**, 698–706.
- C.-W. Tsai, Y.-L. Chen, M.-H. Tsai, J.-W. Yeh, T.-T. Shun and S.-K. Chen, *J. Alloys Compd.*, 2009, **486**, 427–435.
- J.-W. Yeh, S.-Y. Chang, Y.-D. Hong, S.-K. Chen and S.-J. Lin, *Mater. Chem. Phys.*, 2007, **103**, 41–46.
- L. J. Santodonato, Y. Zhang, M. Feygenson, C. M. Parish, M. C. Gao, R. J. Weber, J. C. Neufeind, Z. Tang and P. K. Liaw, *Nat. Commun.*, 2015, **6**, 5964.
- Y. Zou, S. Maiti, W. Steurer and R. Spolenak, *Acta Mater.*, 2014, **65**, 85–97.
- S. Ranganathan, *Curr. Sci.*, 2003, **85**, 1404–1406.
- J.-W. Yeh, *Jom*, 2013, **65**, 1759–1771.
- E. J. Pickering and N. G. Jones, *Int. Mater. Rev.*, 2016, **61**, 183–202.
- Y. Zhang, T. T. Zuo, Z. Tang, M. C. Gao, K. A. Dahmen, P. K. Liaw and Z. P. Lu, *Prog. Mater. Sci.*, 2014, **61**, 1–93.
- A. Takeuchi and A. Inoue, *Mater. T. JIM*, 2000, **41**, 1372–1378.
- Y. Zhang, Y. J. Zhou, J. P. Lin, G. L. Chen and P. K. Liaw, *Adv. Eng. Mater.*, 2008, **10**, 534–538.
- O. Senkov and D. Miracle, *Mater. Res. Bull.*, 2001, **36**, 2183–2198.
- A. Singh, N. Kumar, A. Dwivedi and A. Subramaniam, *Intermetallics*, 2014, **53**, 112–119.
- S. Fang, X. Xiao, L. Xia, W. Li and Y. Dong, *J. Non-Cryst. Solids*, 2003, **321**, 120–125.
- S. Guo, C. Ng, J. Lu and C. T. Liu, *J. Appl. Phys.*, 2011, **109**, 103505.
- X. Yang and Y. Zhang, *Mater. Chem. Phys.*, 2012, **132**, 233–238.
- Y. F. Ye, Q. Wang, J. Lu, C. T. Liu and Y. Yang, *Scr. Mater.*, 2015, **104**, 53–55.
- S. Guo, Q. Hu, C. Ng and C. T. Liu, *Intermetallics*, 2013, **41**, 96–103.
- A. Takeuchi, K. Amiya, T. Wada, K. Yubuta, W. Zhang and A. Makino, *Entropy*, 2013, **15**, 3810–3821.
- Z. Wang, Y. Huang, Y. Yang, J. Wang and C. T. Liu, *Scr. Mater.*, 2015, **94**, 28–31.
- Z. Wang, S. Guo and C. T. Liu, *Jom*, 2014, **66**, 1966–1972.
- Y. F. Ye, Q. Wang, J. Lu, C. T. Liu and Y. Yang, *Mater. Today*, 2016, **19**, 349–362.
- S. Guo and C. T. Liu, *Prog. Nat. Sci.-Mater.*, 2011, **21**, 433–446.
- Y. F. Ye, C. T. Liu and Y. Yang, *Acta Mater.*, 2015, **94**, 152–161.
- R. Feng, M. Gao, C. Lee, M. Mathes, T. Zuo, S. Chen, J. Hawk, Y. Zhang and P. Liaw, *Entropy*, 2016, **18**, 333.
- P. D. Jablonski, J. J. Licavoli, M. C. Gao and J. A. Hawk, *Jom*, 2015, **67**, 2278–2287.
- Y. Brif, M. Thomas and I. Todd, *Scr. Mater.*, 2015, **99**, 93–96.
- Y.-J. Jia, H.-N. Chen and X.-D. Liang, *Rare Met.*, 2019, **38**, 1153–1159.
- T. Fujieda, H. Shiratori, K. Kuwabara, T. Kato, K. Yamanaka, Y. Koizumi and A. Chiba, *Mater. Lett.*, 2015, **159**, 12–15.
- I. Kunce, M. Polanski and J. Bystrzycki, *Int. J. Hydrogen Energy*, 2013, **38**, 12180–12189.
- S. Varalakshmi, G. Appa Rao, M. Kamaraj and B. S. Murty, *J. Mater. Sci.*, 2010, **45**, 5158–5163.
- W. Ji, Z. Fu, W. Wang, H. Wang, J. Zhang, Y. Wang and F. Zhang, *J. Alloys Compd.*, 2014, **589**, 61–66.

- 43 S. Calderon Velasco, A. Cavaleiro and S. Carvalho, *Prog. Mater. Sci.*, 2016, **84**, 158–191.
- 44 Y. Y. Chen, T. Duval, U. D. Hung, J. W. Yeh and H. C. Shih, *Corros. Sci.*, 2005, **47**, 2257–2279.
- 45 X. Li, Y. Fautrelle and Z. Ren, *Acta Mater.*, 2007, **55**, 1377–1386.
- 46 Y. Zhang, B. Zhang, K. Li, G.-L. Zhao and S. M. Guo, *J. Alloys Compd.*, 2017, **734**, 220–228.
- 47 Y. Duan, X. Wen, B. Zhang, G. Ma and T. Wang, *J. Magn. Magn. Mater.*, 2020, **497**, 165947.
- 48 A. S. Sharma, S. Yadav, K. Biswas and B. Basu, *Mater. Sci. Eng., R*, 2018, **131**, 1–42.
- 49 D. Tejero-Martin, M. Rezvani Rad, A. McDonald and T. Hussain, *J. Therm. Spray Technol.*, 2019, **28**, 598–644.
- 50 X. Ji, C. Banks, A. Holloway, K. Jurkschat, C. Thorogood, G. Wildgoose and R. Compton, *Electroanal.*, 2006, **18**, 2481–2485.
- 51 G. Z. Chen, D. J. Fray and T. W. Farthing, *Nature*, 2000, **407**, 361–364.
- 52 C. Schwandt, D. T. L. Alexander and D. J. Fray, *Electrochim. Acta*, 2009, **54**, 3819–3829.
- 53 J. Peng, K. Jiang, W. Xiao, D. Wang, X. Jin and G. Z. Chen, *Chem. Mater.*, 2008, **20**, 7274–7280.
- 54 D. Sri Maha Vishnu, N. Sanil, L. Shakila, G. Panneerselvam, R. Sudha, K. S. Mohandas and K. Nagarajan, *Electrochim. Acta*, 2013, **100**, 51–62.
- 55 C.-Z. Yao, P. Zhang, M. Liu, G.-R. Li, J.-Q. Ye, P. Liu and Y.-X. Tong, *Electrochim. Acta*, 2008, **53**, 8359–8365.
- 56 Y. Chenzhong, M. Huixuan and T. Yexiang, *Chin. J. Appl. Chem.*, 2011, **28**, 1190–1194.
- 57 J. Sure, D. S. M. Vishnu and C. Schwandt, *Appl. Mater. Today*, 2017, **9**, 111–121.
- 58 B. Wang, J. Huang, J. Fan, Y. Dou, H. Zhu and D. Wang, *J. Electrochem. Soc.*, 2017, **164**, 575–579.
- 59 H. Jiao, M. Wang, J. Tu and S. Jiao, *J. Electrochem. Soc.*, 2018, **165**, 574–579.
- 60 J. Sure, D. Sri Maha Vishnu and C. Schwandt, *J. Alloys Compd.*, 2019, **776**, 133–141.
- 61 K. D. Gilroy, A. Ruditskiy, H. C. Peng, D. Qin and Y. Xia, *Chem. Rev.*, 2016, **116**, 10414–10472.
- 62 N. Ortiz, R. G. Weiner and S. E. Skrabalak, *ACS Nano*, 2014, **8**, 12461–12467.
- 63 P.-C. Chen, X. Liu, J. L. Hedrick, Z. Xie, S. Wang, Q.-Y. Lin, M. C. Hersam, V. P. Dravid and C. A. Mirkin, *Science*, 2016, **352**, 1565–1569.
- 64 P. C. Chen, G. Liu, Y. Zhou, K. A. Brown, N. Chernyak, J. L. Hedrick, S. He, Z. Xie, Q. Y. Lin, V. P. Dravid, S. A. O'Neill-Slawecki and C. A. Mirkin, *J. Am. Chem. Soc.*, 2015, **137**, 9167–9173.
- 65 Y. Yao, Z. Huang, P. Xie, S. D. Lacey, R. J. Jacob, H. Xie, F. Chen, A. Nie, T. Pu, M. Rehwoldt, D. Yu, M. R. Zachariah, C. Wang, R. Shahbazian-Yassar, J. Li and L. Hu, *Science*, 2018, **359**, 1489–1494.
- 66 S. E. Skrabalak, *Science*, 2018, **359**, 1467.
- 67 Y. Wu, Z. Lei, X. Liu, H. Wang and Z. Lu, *Sci. Bull.*, 2018, **63**, 737–738.
- 68 P. Xie, Y. Yao, Z. Huang, Z. Liu, J. Zhang, T. Li, G. Wang, R. Shahbazian-Yassar, L. Hu and C. Wang, *Nat. Commun.*, 2019, **10**, 4011.
- 69 X. Xu, Y. Du, C. Wang, Y. Guo, J. Zou, K. Zhou, Z. Zeng, Y. Liu and L. Li, *J. Alloys Compd.*, 2020, **822**, 153642.
- 70 J.-K. Lung, J.-C. Huang, D.-C. Tien, C.-Y. Liao, K.-H. Tseng, T.-T. Tsung, W.-S. Kao, T.-H. Tsai, C.-S. Jwo, H.-M. Lin and L. Stobinski, *J. Alloys Compd.*, 2007, **434–435**, 655–658.
- 71 Q. Wu, Z. Wang, F. He, L. Wang, J. Luo, J. Li and J. Wang, *Metall. Mater. Trans. A*, 2018, **49**, 4986–4990.
- 72 A. Mao, H. Xiang, X. Ran, Y. Li, X. Jin, H. Yu and X. Gu, *J. Alloys Compd.*, 2019, **775**, 1177–1183.
- 73 A. Xia, O. Glushko, M. J. Cordill and R. Franz, *J. Vac. Sci. Technol., A*, 2019, **37**, 010601.
- 74 J.-M. Park, J.-W. Kang, W.-H. Lee, S. Y. Lee, S.-H. Min, T. K. Ha and H.-K. Park, *Mater. Lett.*, 2019, **255**, 126513.
- 75 W.-H. Lee, K. B. Park, K.-W. Yi, S. Y. Lee, K. Park, T. W. Lee, T.-W. Na and H.-K. Park, *Metals*, 2019, **9**, 1296.
- 76 R. Roy, D. Agrawal, J. Cheng and S. Gedevanishvili, *Nature*, 1999, **401**, 668–670.
- 77 K. I. Rybakov, E. A. Olevsky, E. V. Krikun and D. J. Green, *J. Am. Ceram. Soc.*, 2013, **96**, 1003–1020.
- 78 P. Veronesi, R. Rosa, E. Colombini, C. Leonelli, G. Poli and A. Casagrande, *J. Microwave Power*, 2010, **44**, 45–56.
- 79 G. Poli, R. Sola and P. Veronesi, *J. Mater. Sci. Eng. A*, 2006, **441**, 149–156.
- 80 R. Rosa, P. Veronesi and C. Leonelli, *Chem. Eng. Process.*, 2013, **71**, 2–18.
- 81 P. Veronesi, R. Rosa, E. Colombini and C. Leonelli, *Technologies*, 2015, **3**, 182–197.
- 82 P. Veronesi, E. Colombini, R. Rosa, C. Leonelli and F. Rosi, *Mater. Lett.*, 2016, **162**, 277–280.
- 83 L. Han, L. Lan, T. Pu, Y. Gu, C. Zhu and H. Zhu, *MATEC Web Conf.*, 2018, **238**, 02004.
- 84 V. G. Kessler, G. A. Seisenbaeva, M. Unell and S. Hakansson, *Angew. Chem., Int. Ed.*, 2008, **47**, 8506–8509.
- 85 G. Liu, Q. Wang, J. Li, Y. Chen and B. He, *Int. J. Refract. Met. Hard Mater.*, 2013, **41**, 622–626.
- 86 B. Niu, F. Zhang, H. Ping, N. Li, J. Zhou, L. Lei, J. Xie, J. Zhang, W. Wang and Z. Fu, *Sci. Rep.*, 2017, **7**, 3421.
- 87 R. X. Li, P. K. Liaw and Y. Zhang, *J. Mater. Sci. Eng. A*, 2017, **707**, 668–673.
- 88 N. Kashaev, V. Ventzke, N. Stepanov, D. Shaysultanov, V. Sanin and S. Zherebtsov, *Intermetallics*, 2018, **96**, 63–71.
- 89 M. V. Klimova, D. G. Shaysultanov, R. S. Chernichenko, V. N. Sanin, N. D. Stepanov, S. V. Zherebtsov and A. N. Belyakov, *J. Mater. Sci. Eng. A*, 2019, **201**, 740–741.
- 90 W. Wang, H. Xie, L. Xie, X. Yang, J. Li and Q. Peng, *Mater. Lett.*, 2018, **233**, 4–7.
- 91 G.-n. Zhang, X. Yang, Z.-c. Yang, Y. Li, G. He and J.-t. Li, *Int. J. Miner., Metall. Mater.*, 2020, **27**, 244–251.
- 92 A. S. Rogachev, S. G. Vadchenko, N. A. Kochetov, D. Y. Kovalev, I. D. Kovalev, A. S. Shchukin, A. N. Gryadunov, F. Baras and O. Politano, *J. Eur. Ceram. Soc.*, 2020, **40**, 2527–2532.
- 93 M. Y. Rekha, N. Mallik and C. Srivastava, *Sci. Rep.*, 2018, **8**, 8737.

- 94 A. Garzon-Manjon, H. Meyer, D. Grotzschla, T. Löffler, W. Schuhmann, A. Ludwig and C. Scheu, *Nanomaterials*, 2018, **8**, 903.
- 95 F. Waag, Y. Li, A. R. Ziefel, E. Bertin, M. Kamp, V. Duppel, G. Marzun, L. Kienle, S. Barcikowski and B. Gökce, *RSC Adv.*, 2019, **9**, 18547–18558.
- 96 M. P. Singh and C. Srivastava, *Mater. Lett.*, 2015, **160**, 419–422.
- 97 M. Bondesgaard, N. L. N. Broge, A. Mamakhe, M. Bremholm and B. B. Iversen, *Adv. Funct. Mater.*, 2019, **29**, 1905933.
- 98 S. Gao, S. Hao, Z. Huang, Y. Yuan, S. Han, L. Lei, X. Zhang, R. Shahbazian-Yassar and J. Lu, *Nat. Commun.*, 2020, **11**, 2016.
- 99 Y. Yang, B. Song, X. Ke, F. Xu, K. N. Bozhilov, L. Hu, R. Shahbazian-Yassar and M. R. Zachariah, *Langmuir*, 2020, **36**, 1985–1992.
- 100 J. H. Ramirez, F. J. Maldonado-Hódar, A. F. Pérez-Cadenas, C. Moreno-Castilla, C. A. Costa and L. M. Madeira, *Appl. Catal., B*, 2007, **75**, 312–323.
- 101 K. Sarlar, A. Tekgül and I. Kucuk, *Curr. Appl. Phys.*, 2020, **20**, 18–22.
- 102 Z. T. Walter and H. An, *Chemosphere*, 1995, **31**, 4157–4170.
- 103 Y. Su, Z. Wu, Y. Wu, J. Yu, L. Sun and C. Lin, *J. Mater. Chem. A*, 2015, **3**, 8537–8544.
- 104 J.-Q. Wang, Y.-H. Liu, M.-W. Chen, G.-Q. Xie, D. V. Louzguine-Luzgin, A. Inoue and J. H. Perepezko, *Adv. Funct. Mater.*, 2012, **22**, 2567–2570.
- 105 Z. Y. Lv, X. J. Liu, B. Jia, H. Wang, Y. Wu and Z. P. Lu, *Sci. Rep.*, 2016, **6**, 34213.
- 106 S. Wu, Y. Pan, N. Wang, W. Dai, J. Lu and T. Lu, *RSC Adv.*, 2018, **8**, 41347–41354.
- 107 S. Wu, Y. Pan, J. Lu, N. Wang, W. Dai and T. Lu, *J. Mater. Sci. Technol.*, 2019, **35**, 1629–1635.
- 108 S.-k. Wu, Y. Pan, N. Wang, T. Lu and W.-j. Dai, *Int. J. Miner. Metall. Mater.*, 2019, **26**, 124–132.
- 109 S. Wu, J. Lu, T. Lu and Y. Pan, *Mater. Res. Express*, 2019, **6**, 1165d4.
- 110 S. Wu, W. Gao, T. Lu and Y. Pan, *Acta Metall. Sin.*, 2020, **33**, 1103–1110.
- 111 U. Ulmer, K. Asano, T. Bergfeldt, V. S. K. Chakravadhanula, R. Dittmeyer, H. Enoki, C. Kübel, Y. Nakamura, A. Pohl and M. Fichtner, *Int. J. Hydrogen Energy*, 2014, **39**, 20000–20008.
- 112 Y.-F. Kao, S.-K. Chen, J.-H. Sheu, J.-T. Lin, W.-E. Lin, J.-W. Yeh, S.-J. Lin, T.-H. Liou and C.-W. Wang, *Int. J. Hydrogen Energy*, 2010, **35**, 9046–9059.
- 113 I. Kunce, M. Polanski and J. Bystrzycki, *Int. J. Hydrogen Energy*, 2014, **39**, 9904–9910.
- 114 M. Sahlberg, D. Karlsson, C. Zlotea and U. Jansson, *Sci. Rep.*, 2016, **6**, 36770.
- 115 D. Karlsson, G. Ek, J. Cedervall, C. Zlotea, K. T. Moller, T. C. Hansen, J. Bednarcik, M. Paskevicius, M. H. Sorby, T. R. Jensen, U. Jansson and M. Sahlberg, *Inorg. Chem.*, 2018, **57**, 2103–2110.
- 116 C. Zlotea, M. A. Sow, G. Ek, J. P. Couzinié, L. Perrière, I. Guillot, J. Bourgon, K. T. Møller, T. R. Jensen, E. Akiba and M. Sahlberg, *J. Alloys Compd.*, 2019, **775**, 667–674.
- 117 C. Zhang, Y. Wu, L. You, X. Cao, Z. Lu and X. Song, *J. Alloys Compd.*, 2019, **781**, 613–620.
- 118 C. Zhang, A. Song, Y. Yuan, Y. Wu, P. Zhang, Z. Lu and X. Song, *Int. J. Hydrogen Energy*, 2020, **45**, 5367–5374.
- 119 I. Kunce, M. Polanski and T. Czujko, *Int. J. Hydrogen Energy*, 2017, **42**, 27154–27164.
- 120 G. Zepon, D. R. Leiva, R. B. Strozi, A. Bedoch, S. J. A. Figueroa, T. T. Ishikawa and W. J. Botta, *Int. J. Hydrogen Energy*, 2018, **43**, 1702–1708.
- 121 J. Hu, H. Shen, M. Jiang, H. Gong, H. Xiao, Z. Liu, G. Sun and X. Zu, *Nanomaterials*, 2019, **9**, 461.
- 122 M. M. Nygård, G. Ek, D. Karlsson, M. Sahlberg, M. H. Sørby and B. C. Hauback, *Int. J. Hydrogen Energy*, 2019, **44**, 29140–29149.
- 123 M. O. de Marco, Y. Li, H.-W. Li, K. Edalati and R. Floriano, *Adv. Eng. Mater.*, 2019, **22**, 1901079.
- 124 P. Edalati, R. Floriano, A. Mohammadi, Y. Li, G. Zepon, H.-W. Li and K. Edalati, *Scr. Mater.*, 2020, **178**, 387–390.
- 125 Y.-H. Zhang, G. Huang, Z.-M. Yuan, S.-H. Guo, Y. Qi and D.-L. Zhao, *Rare Met.*, 2018, **39**, 181–192.
- 126 B. Sharma, A. Sharma and J.-S. Kim, *Sens. Actuators, B*, 2018, **262**, 758–770.
- 127 B. Sharma and S. Harini, *Mater. Res. Express*, 2019, **6**, 1165d7.
- 128 Q. Liao, N. Li, S. Jin, G. Yang and C. Wang, *ACS Nano*, 2015, **9**, 5310–5317.
- 129 A. K. Singh and K. Mandal, *J. Appl. Phys.*, 2015, **117**, 105101.
- 130 J. J. Gao, H. J. Qiu, Y. R. Wen, F. K. Chiang and Y. Wang, *J. Colloid Interface Sci.*, 2016, **474**, 18–24.
- 131 K. Kong, J. Hyun, Y. Kim, W. Kim and D. Kim, *J. Power Sources*, 2019, **437**, 226927.
- 132 Y. Liu, Z. Zeng, R. K. Sharma, S. Gbewonyo, K. Allado, L. Zhang and J. Wei, *J. Power Sources*, 2019, **409**, 1–5.
- 133 Y. Liu, Z. Zeng, B. Bloom, D. H. Waldeck and J. Wei, *Small*, 2018, **14**, 1703237.
- 134 X. Dai, Y. Du, J. Yang, D. Wang, J. Gu, Y. Li, S. Wang, B. B. Xu and J. Kong, *Compos. Sci. Technol.*, 2019, **174**, 27–32.
- 135 L. Huang, Y. Duan, X. Dai, Y. Zeng, G. Ma, Y. Liu, S. Gao and W. Zhang, *Small*, 2019, **15**, 1902730.
- 136 K. Lance Kelly, E. Coronado, L. L. Zhao and G. C. Schatz, *J. Phys. Chem. B*, 2003, **107**, 668–677.
- 137 J. L. Snoek, *Physica C*, 1948, **14**, 207–217.
- 138 C. Wang, X. Han, P. Xu, J. Wang, Y. Du, X. Wang, W. Qin and T. Zhang, *J. Phys. Chem. C*, 2010, **114**, 3196–3203.
- 139 S. J. Yan, L. Zhen, C. Y. Xu, J. T. Jiang and W. Z. Shao, *J. Phys. D: Appl. Phys.*, 2010, **43**, 245003.
- 140 P. Yang, Y. Liu, X. Zhao, J. Cheng and H. Li, *Adv. Powder Technol.*, 2016, **27**, 1128–1133.
- 141 P. Yang, Y. Liu, X. Zhao, J. Cheng and H. Li, *J. Mater. Res.*, 2016, **31**, 2398–2406.
- 142 Y. Zhang, B. Zhang, K. Li, G.-L. Zhao and S. M. Guo, *J. Alloys Compd.*, 2018, **734**, 220–228.
- 143 B. Zhang, Y. Duan, Y. Cui, G. Ma, T. Wang and X. Dong, *Mater. Des.*, 2018, **149**, 173–183.

- 144 B. Zhang, Y. Duan, X. Wen, G. Ma, T. Wang, X. Dong, H. Zhang, N. Jia and Y. Zeng, *J. Alloys Compd.*, 2019, **790**, 179–188.
- 145 Y. Duan, Y. Cui, B. Zhang, G. Ma and W. Tongmin, *J. Alloys Compd.*, 2019, **773**, 194–201.
- 146 Z. Yingzhe, C. Yudao, Q. Qingdong and L. Wei, *J. Magn. Magn. Mater.*, 2020, **498**, 166151.
- 147 Y. Li, S. Shang and W. Zhang, *AIP Adv.*, 2019, **9**, 125045.
- 148 D. Lan, Z. Zhao, Z. Gao, K. Kou, G. Wu and H. Wu, *J. Magn. Magn. Mater.*, 2020, **512**, 167065.
- 149 H. Wu, D. Lan, B. Li, L. Zhang, Y. Fu, Y. Zhang and H. Xing, *Composites, Part B*, 2019, **179**, 107524.
- 150 K. Biswas, J. He, I. D. Blum, C. I. Wu, T. P. Hogan, D. N. Seidman, V. P. Dravid and M. G. Kanatzidis, *Nature*, 2012, **489**, 414–418.
- 151 D. T. Crane and J. W. LaGrandeur, *J. Electron. Mater.*, 2009, **39**, 2142–2148.
- 152 A. I. Hochbaum, R. Chen, R. D. Delgado, W. Liang, E. C. Garnett, M. Najarian, A. Majumdar and P. Yang, in *Materials for Sustainable Energy*, Co-Published with Macmillan Publishers Ltd, UK, 2010, 111.
- 153 S. Chen and Z. Ren, *Mater. Today*, 2013, **16**, 387–395.
- 154 S. Shafeie, S. Guo, Q. Hu, H. Fahlquist, P. Erhart and A. Palmqvist, *J. Appl. Phys.*, 2015, **118**, 184905.
- 155 L. Kush, S. Srivastava, Y. Jaiswal and Y. Srivastava, *Mater. Res. Express*, 2020, **7**, 035704.
- 156 W. Dong, Z. Zhou, L. Zhang, M. Zhang, P. Liaw, G. Li and R. Liu, *Metals*, 2018, **8**, 781.
- 157 Z. Fan, H. Wang, Y. Wu, X. Liu and Z. Lu, *Mater. Res. Lett.*, 2016, **5**, 187–194.
- 158 Z. Fan, H. Wang, Y. Wu, X. J. Liu and Z. P. Lu, *RSC Adv.*, 2016, **6**, 52164–52170.
- 159 A. Karati, M. Nagini, S. Ghosh, R. Shabadi, K. G. Pradeep, R. C. Mallik, B. S. Murty and U. V. Varadaraju, *Sci. Rep.*, 2019, **9**, 5331.
- 160 A. Karati, V. S. Hariharan, S. Ghosh, A. Prasad, M. Nagini, K. Guruvaidyathri, R. C. Mallik, R. Shabadi, L. Bichler, B. S. Murty and U. V. Varadaraju, *Scr. Mater.*, 2020, **186**, 375–380.
- 161 A. Raphael, P. Vivekanandhan and S. Kumaran, *Mater. Lett.*, 2020, **269**, 127672.
- 162 K. L. Murty and I. Charit, *J. Nucl. Mater.*, 2008, **383**, 189–195.
- 163 P. Yvon and F. Carré, *J. Nucl. Mater.*, 2009, **385**, 217–222.
- 164 A. F. Rowcliffe, L. K. Mansur, D. T. Hoelzer and R. K. Nanstad, *J. Nucl. Mater.*, 2009, **392**, 341–352.
- 165 P. Lü, H. P. Wang, P. F. Zou, K. Zhou, L. Hu and B. Wei, *J. Appl. Phys.*, 2018, **124**, 025103.
- 166 S. J. Zinkle, K. A. Terrani and L. L. Snead, *Curr. Opin. Solid State Mater. Sci.*, 2016, **20**, 401–410.
- 167 T. Egami, W. Guo, P. D. Rack and T. Nagase, *Metall. Mater. Trans. A*, 2013, **45**, 180–183.
- 168 S. Q. Xia, X. Yang, T. F. Yang, S. Liu and Y. Zhang, *Jom*, 2015, **67**, 2340–2344.
- 169 T. Yang, S. Xia, W. Guo, R. Hu, J. D. Poplawsky, G. Sha, Y. Fang, Z. Yan, C. Wang, C. Li, Y. Zhang, S. J. Zinkle and Y. Wang, *Scr. Mater.*, 2018, **144**, 31–35.
- 170 G. Pu, L. Lin, R. Ang, K. Zhang, B. Liu, B. Liu, T. Peng, S. Liu and Q. Li, *Appl. Surf. Sci.*, 2020, **516**, 146129.
- 171 L. Yang, H. Ge, J. Zhang, T. Xiong, Q. Jin, Y. Zhou, X. Shao, B. Zhang, Z. Zhu, S. Zheng and X. Ma, *J. Mater. Sci. Technol.*, 2019, **35**, 300–305.
- 172 Y. Lu, H. Huang, X. Gao, C. Ren, J. Gao, H. Zhang, S. Zheng, Q. Jin, Y. Zhao, C. Lu, T. Wang and T. Li, *J. Mater. Sci. Technol.*, 2019, **35**, 369–373.
- 173 O. El-Atwani, N. Li, M. Li, A. Devaraj, J. K. S. Baldwin, M. M. Schneider, D. Sobieraj, J. S. Wróbel, D. Nguyen-Manh, S. A. Maloy and E. Martinez, *Sci. Adv.*, 2019, **5**, 2002.
- 174 Y. Zhang, M. A. Tunes, M. L. Crespiello, F. Zhang, W. L. Boldman, P. D. Rack, L. Jiang, C. Xu, G. Greaves, S. E. Donnelly, L. Wang and W. J. Weber, *Nanotechnology*, 2019, **30**, 294004.
- 175 W. Zhang, M. Wang, L. Wang, C. H. Liu, H. Chang, J. J. Yang, J. L. Liao, Y. Y. Yang and N. Liu, *Appl. Surf. Sci.*, 2019, **485**, 108–118.
- 176 M. Moschetti, A. Xu, B. Schuh, A. Hohenwarter, J.-P. Couzinié, J. J. Krizic, D. Bhattacharyya and B. Gludovatz, *Jom*, 2019, **72**, 130–138.
- 177 D. Patel, M. D. Richardson, B. Jim, S. Akhmadaliev, R. Goodall and A. S. Gandy, *J. Nucl. Mater.*, 2020, **531**, 152005.
- 178 E. Brück, O. Tegus, L. Zhang, X. W. Li, F. R. de Boer and K. H. J. Buschow, *J. Alloys Compd.*, 2004, **383**, 32–36.
- 179 A. V. Kimel, A. Kirilyuk, A. Tsvetkov, R. V. Pisarev and T. Rasing, *Nature*, 2004, **429**, 850–853.
- 180 O. Tegus, E. Brück, K. H. J. Buschow and F. R. de Boer, *Nature*, 2002, **415**, 150–152.
- 181 T. Krenke, E. Duman, M. Acet, E. F. Wassermann, X. Moya, L. Manosa and A. Planes, *Nat. Mater.*, 2005, **4**, 450–454.
- 182 J. J. Ipus, J. S. Blázquez, V. Franco, A. Conde and L. F. Kiss, *J. Appl. Phys.*, 2009, **105**, 123922.
- 183 V. Franco, J. S. Blázquez, C. F. Conde and A. Conde, *Appl. Phys. Lett.*, 2006, **88**, 042505.
- 184 J. Huo, L. Huo, H. Men, X. Wang, A. Inoue, J. Wang, C. Chang and R.-W. Li, *Intermetallics*, 2015, **58**, 31–35.
- 185 M. Kurniawan, A. Perrin, P. Xu, V. Keylin and M. McHenry, *IEEE Magn. Lett.*, 2016, **7**, 1–5.
- 186 Y. Yuan, Y. Wu, X. Tong, H. Zhang, H. Wang, X. J. Liu, L. Ma, H. L. Suo and Z. P. Lu, *Acta Mater.*, 2017, **125**, 481–489.
- 187 W. Sheng, J.-Q. Wang, G. Wang, J. Huo, X. Wang and R.-W. Li, *Intermetallics*, 2018, **96**, 79–83.
- 188 J. Li, L. Xue, W. Yang, C. Yuan, J. Huo and B. Shen, *Intermetallics*, 2018, **96**, 90–93.
- 189 J. Huo, J.-Q. Wang and W.-H. Wang, *J. Alloys Compd.*, 2019, **776**, 202–206.
- 190 L. Xue, L. Shao, Q. Luo and B. Shen, *J. Alloys Compd.*, 2019, **790**, 633–639.
- 191 A. Perrin, M. Sorescu, M.-T. Burton, D. E. Laughlin and M. McHenry, *Jom*, 2017, **69**, 2125–2129.
- 192 S.-M. Na, P. K. Lambert, H. Kim, J. Paglione and N. J. Jones, *AIP Adv.*, 2019, **9**, 035010.
- 193 K. Sarlar, A. Tekgul and I. Kucuk, *IEEE Magn. Lett.*, 2019, **10**, 1–5.

- 194 P. Koželj, S. Vrtnik, A. Jelen, S. Jazbec, Z. Jaglicic, S. Maiti, M. Feuerbacher, W. Steurer and J. Dolinsek, *Phys. Rev. Lett.*, 2014, **113**, 107001.
- 195 K. Jasiewicz, B. Wiendlocha, P. Korbeń, S. Kaprzyk and J. Tobola, *Phys. Status Solidi RRL*, 2016, **10**, 415–419.
- 196 F. von Rohr, M. J. Winiarski, J. Tao, T. Klimeczuk and R. J. Cava, *Proc. Natl. Acad. Sci.*, 2016, **113**, 7144–7150.
- 197 S. Vrtnik, P. Koželj, A. Meden, S. Maiti, W. Steurer, M. Feuerbacher and J. Dolinšek, *J. Alloys Compd.*, 2017, **695**, 3530–3540.
- 198 K. Jasiewicz, B. Wiendlocha, K. Górnicka, K. Goffryk, M. Gazda, T. Klimeczuk and J. Tobola, *Phys. Rev. B*, 2019, **100**, 184503.
- 199 F. O. von Rohr and R. J. Cava, *Phys. Rev. Mater.*, 2018, **2**, 034801.
- 200 S. Marik, M. Varghese, K. P. Sajilesh, D. Singh and R. P. Singh, *J. Alloys Compd.*, 2018, **769**, 1059–1063.
- 201 Y. Yuan, Y. Wu, H. Luo, Z. Wang, X. Liang, Z. Yang, H. Wang, X. Liu and Z. Lu, *Front. Mater.*, 2018, **5**, 72.
- 202 N. Ishizu and J. Kitagawa, *Results Phys.*, 2019, **13**, 102275.
- 203 K. Stolze, F. A. Cevallos, T. Kong and R. J. Cava, *J. Mater. Chem. C*, 2018, **6**, 10441–10449.
- 204 S. Marik, K. Motla, M. Varghese, K. P. Sajilesh, D. Singh, Y. Breard, P. Boullay and R. P. Singh, *Phys. Rev. Mater.*, 2019, **3**, 060602.
- 205 B. Liu, J. Wu, Y. Cui, Q. Zhu, G. Xiao, S. Wu, G. Cao and Z. Ren, *Scr. Mater.*, 2020, **182**, 109–113.
- 206 W. L. Nelson, A. T. Chemey, M. Hertz, E. Choi, D. E. Graf, S. Latturner, T. E. Albrecht-Schmitt, K. Wei and R. E. Baumbach, *Sci. Rep.*, 2020, **10**, 4717.
- 207 Y.-S. Lee and R. J. Cava, *Physica C*, 2019, **566**, 1353520.
- 208 J. Wu, B. Liu, Y. Cui, Q. Zhu, G. Xiao, H. Wang, S. Wu, G. Cao and Z. Ren, *Sci. China Mater.*, 2020, **63**, 823–831.
- 209 R. Sogabe, Y. Goto and Y. Mizuguchi, *Appl. Phys. Express*, 2018, **11**, 053102.
- 210 Y. Shukunami, A. Yamashita, Y. Goto and Y. Mizuguchi, *Physica C*, 2020, **572**, 1353623.
- 211 Y. Mizuguchi, *J. Phys. Soc. Jpn.*, 2019, **88**, 041001.
- 212 A. Yamashita, R. Jha, Y. Goto, T. D. Matsuda, Y. Aoki and Y. Mizuguchi, *Dalton Trans.*, 2020, **49**, 9118–9122.
- 213 H. Kou, J. Lu and Y. Li, *Adv. Mater.*, 2014, **26**, 5518–5524.
- 214 K.-Y. Wu, S.-K. Chen and J.-M. Wu, *Nat. Sci.*, 2018, **10**, 110–124.
- 215 K. Stolze, J. Tao, F. O. von Rohr, T. Kong and R. J. Cava, *Chem. Mater.*, 2018, **30**, 906–914.
- 216 B. T. Matthias, *Phys. Rev.*, 1955, **97**, 74–76.
- 217 M. M. Colver and R. H. Hammond, *Phys. Rev. Lett.*, 1973, **30**, 92–95.
- 218 L. Sun and R. J. Cava, *Phys. Rev. Mater.*, 2019, **3**, 090301.
- 219 P. A. J. Bagot, K. Kruska, D. Haley, X. Carrier, E. Marceau, M. P. Moody and G. D. W. Smith, *J. Phys. Chem. C*, 2014, **118**, 26130–26138.
- 220 H.-J. Qiu, G. Fang, Y. Wen, P. Liu, G. Xie, X. Liu and S. Sun, *J. Mater. Chem. A*, 2019, **7**, 6499–6506.
- 221 M. M. Biener, J. Biener, A. Wichmann, A. Wittstock, T. F. Baumann, M. Baumer and A. V. Hamza, *Nano Lett.*, 2011, **11**, 3085–3090.
- 222 G. Orozco and C. Gutiérrez, *Electroanal. Chem.*, 2000, **484**, 64–72.
- 223 P. Strasser, Q. Fan, D. Martin and W. H. Weinberg, *J. Phys. Chem. B*, 2003, **107**, 11013–11021.
- 224 E. Reddington, S. Anthony, B. Gurau, R. Viswanathan, S. Sarangapani, E. S. Smotkin and T. E. Mallouk, *Science*, 1998, **280**, 1735–1737.
- 225 C.-F. Tsai, P.-W. Wu, P. Lin, C.-G. Chao and K.-Y. Yeh, *Jpn. J. Appl. Phys.*, 2008, **47**, 5755–5761.
- 226 C.-F. Tsai, K.-Y. Yeh, P.-W. Wu, Y.-F. Hsieh and P. Lin, *J. Alloys Compd.*, 2009, **478**, 868–871.
- 227 A.-L. Wang, H.-C. Wan, H. Xu, Y.-X. Tong and G.-R. Li, *Electrochim. Acta*, 2014, **127**, 448–453.
- 228 X. Chen, C. Si, Y. Gao, J. Frenzel, J. Sun, G. Eggeler and Z. Zhang, *J. Power Sources*, 2015, **273**, 324–332.
- 229 K. V. Yusenko, S. Riva, P. A. Carvalho, M. V. Yusenko, S. Arnaboldi, A. S. Sukhikh, M. Hanfland and S. A. Gromilov, *Scr. Mater.*, 2017, **138**, 22–27.
- 230 S. Chu and A. Majumdar, *Nature*, 2012, **488**, 294–303.
- 231 S.-M. Kim, S.-H. Jin, Y.-J. Lee and M. H. Lee, *Electrochim. Acta*, 2017, **252**, 67–75.
- 232 G. Zhang, K. Ming, J. Kang, Q. Huang, Z. Zhang, X. Zheng and X. Bi, *Electrochim. Acta*, 2018, **279**, 19–23.
- 233 M. A. Ud Din, F. Saleem, B. Ni, Y. Yong and X. Wang, *Adv. Mater.*, 2017, **29**, 1604994.
- 234 Z. Jin, J. Lv, H. Jia, W. Liu, H. Li, Z. Chen, X. Lin, G. Xie, X. Liu, S. Sun and H. J. Qiu, *Small*, 2019, **15**, 1904180.
- 235 Z. Jia, T. Yang, L. Sun, Y. Zhao, W. Li, J. Luan, F. Lyu, L. C. Zhang, J. J. Kružić, J. J. Kai, J. C. Huang, J. Lu and C. T. Liu, *Adv. Mater.*, 2020, 2000385.
- 236 H. J. Qiu, P. Du, K. Hu, J. Gao, H. Li, P. Liu, T. Ina, K. Ohara, Y. Ito and M. Chen, *Adv. Mater.*, 2019, **31**, 1900843.
- 237 B. M. Tackett, W. Sheng, S. Kattel, S. Yao, B. Yan, K. A. Kuttiyiel, Q. Wu and J. G. Chen, *ACS Catal.*, 2018, **8**, 2615–2621.
- 238 T. Reier, Z. Pawolek, S. Cherevko, M. Bruns, T. Jones, D. Teschner, S. Selve, A. Bergmann, H. N. Nong, R. Schlogl, K. J. Mayrhofer and P. Strasser, *J. Am. Chem. Soc.*, 2015, **137**, 13031–13040.
- 239 Q. Shi, C. Zhu, D. Du and Y. Lin, *Chem. Soc. Rev.*, 2019, **48**, 3181–3192.
- 240 W. Dai, T. Lu and Y. Pan, *J. Power Sources*, 2019, **430**, 104–111.
- 241 H.-J. Qiu, G. Fang, J. Gao, Y. Wen, J. Lv, H. Li, G. Xie, X. Liu and S. Sun, *ACS Mater. Lett.*, 2019, **1**, 526–533.
- 242 K. Huang, B. Zhang, J. Wu, T. Zhang, D. Peng, X. Cao, Z. Zhang, Z. Li and Y. Huang, *J. Mater. Chem. A*, 2020, **8**, 11938–11947.
- 243 L. Bu, N. Zhang, S. Guo, X. Zhang, J. Li, J. Yao, T. Wu, G. Lu, J.-Y. Ma, D. Su and X. Huang, *Science*, 2016, **354**, 1410.
- 244 M. Shao, Q. Chang, J. P. Dodelet and R. Chenitz, *Chem. Rev.*, 2016, **116**, 3594–3657.
- 245 A. Holewinski, J.-C. Idrobo and S. Linic, *Nat. Chem.*, 2014, **6**, 828–834.
- 246 M. Luo and S. Guo, *Nat. Rev. Mater.*, 2017, **2**, 17059.

- 247 P. Strasser, S. Koh, T. Anniyev, J. Greeley, K. More, C. Yu, Z. Liu, S. Kaya, D. Nordlund, H. Ogasawara, M. F. Toney and A. Nilsson, *Nat. Chem.*, 2010, **2**, 454–460.
- 248 S. Li, X. Tang, H. Jia, H. Li, G. Xie, X. Liu, X. Lin and H.-J. Qiu, *J. Catal.*, 2020, **383**, 164–171.
- 249 C. W. Li, J. Ciston and M. W. Kanan, *Nature*, 2014, **508**, 504–507.
- 250 S. Nellaippan, N. K. Katiyar, R. Kumar, A. Parui, K. D. Malviya, K. G. Pradeep, A. K. Singh, S. Sharma, C. S. Tiwary and K. Biswas, *ACS Catal.*, 2020, **10**, 3658–3663.
- 251 J. K. Pedersen, T. A. A. Batchelor, A. Bagger and J. Rossmeisl, *ACS Catal.*, 2020, **10**, 2169–2176.
- 252 G. S. Firstov, T. A. Kosorukova, Y. N. Koval and V. V. Odnosum, *Mater. Today: Proc.*, 2015, **2**, 499–503.
- 253 W. J. Buehler, J. V. Gilfrich and R. C. Wiley, *J. Appl. Phys.*, 1963, **34**, 1475–1477.
- 254 K. Otsuka and X. Ren, *Prog. Mater. Sci.*, 2005, **50**, 511–678.
- 255 T. Duerig, A. Pelton and D. Stöckel, *Mater. Sci. Eng., A*, 1999, **273–275**, 149–160.
- 256 J. Frenzel, A. Wieczorek, I. Opahle, B. Maafß, R. Drautz and G. Eggeler, *Acta Mater.*, 2015, **90**, 213–231.
- 257 A. R. Pelton, *J. Mater. Eng. Perform.*, 2011, **20**, 613–617.
- 258 Y. Furuya and Y. C. Park, *Nondestr. Test. Eval.*, 1992, **8–9**, 541–554.
- 259 G. S. Firstov, T. A. Kosorukova, Y. N. Koval and P. A. Verhovlyuk, *Shap. Mem. Superelasticity*, 2015, **1**, 400–407.
- 260 C.-H. Chen and Y.-J. Chen, *Scr. Mater.*, 2019, **162**, 185–189.
- 261 H.-C. Lee, Y.-J. Chen and C.-H. Chen, *Entropy*, 2019, **21**, 1027.
- 262 D. Canadinc, W. Treherne, J. Ma, I. Karaman, F. Sun and Z. Chaudhry, *Scr. Mater.*, 2019, **158**, 83–87.
- 263 L. Wang, C. Fu, Y. Wu, R. Li, X. Hui and Y. Wang, *Scr. Mater.*, 2019, **162**, 112–117.
- 264 J. I. Lee, K. Tsuchiya, W. Tasaki, H. S. Oh, T. Sawaguchi, H. Murakami, T. Hiroto, Y. Matsushita and E. S. Park, *Sci. Rep.*, 2019, **9**, 13140.
- 265 D. Piorunek, J. Frenzel, N. Jöns, C. Somsen and G. Eggeler, *Intermetallics*, 2020, **122**, 106792.
- 266 L. Peltier, P. Lohmuller, F. Meraghni, S. Berveiller, E. Patoor and P. Laheurte, *Shap. Mem. Superelasticity*, 2020, **6**, 273.
- 267 Y. Li, J. Lu, M. Li, K. Chang, X. Zha, Y. Zhang, K. Chen, P. O. Å. Persson, L. Hultman, P. Eklund, S. Du, J. S. Francisco, Z. Chai, Z. Huang and Q. Huang, *Proc. Natl. Acad. Sci.*, 2020, **117**, 820.
- 268 C. Zhao, F. Ding, Y. Lu, L. Chen and Y. S. Hu, *Angew. Chem., Int. Ed.*, 2020, **59**, 264–269.
- 269 D. Feng, Y. Dong, L. Zhang, X. Ge, W. Zhang, S. Dai and Z. A. Qiao, *Angew. Chem., Int. Ed.*, 2020, **59**, 2–9.
- 270 D. Wang, X. Wang, Y. Lu, C. S. Song, J. Pan, C. L. Li, M. L. Sui, W. Zhao and F. Q. Huang, *J. Mater. Chem. A*, 2017, **5**, 22618–22624.
- 271 C. Huang, X. Wang, D. Wang, W. Zhao, K. J. Bu, J. J. Xu, X. Y. Huang, Q. Y. Bi, J. Huang and F. Q. Huang, *Chem. Mater.*, 2019, **31**, 4726–4731.
- 272 M. Todai, T. Nagase, T. Hori, A. Matsugaki, A. Sekita and T. Nakano, *Scr. Mater.*, 2017, **129**, 65–68.
- 273 G. Popescu, B. Ghiban, C. A. Popescu, L. Rosu, R. Trusca, I. Carcea, V. Soare, D. Dumitrescu, I. Constantin, M. T. Olaru and B. A. Carlan, *IOP Conf. Ser.: Mater. Sci. Eng.*, 2018, **400**, 022049.
- 274 M. Gueye, S. Ammar-Merah, S. Nowak, P. Decorse, A. Chevillot-Biraud, L. Perrière, J. P. Couzinie, I. Guillot and G. Dirras, *Surf. Coat. Technol.*, 2020, **385**, 1253742.
- 275 Y. Liu, H.-J. Wang, S.-J. Pang and T. Zhang, *Rare Met.*, 2018, **39**, 688–694.
- 276 B.-Q. Li, C.-L. Li, Z.-X. Wang and X. Lu, *Rare Met.*, 2019, **38**, 571–576.
- 277 Q. Ding, Y. Zhang, X. Chen, X. Fu, D. Chen, S. Chen, L. Gu, F. Wei, H. Bei, Y. Gao, M. Wen, J. Li, Z. Zhang, T. Zhu, R. O. Ritchie and Q. Yu, *Nature*, 2019, **574**, 223–227.